U.S.NRC
United States Nuclear Regulatory Commission
Protecting People and the Environment

NUREG/CR-7215

Spent Fuel Pool Project Phase I:
Pre-Ignition and Ignition Testing of a Single Commercial 17x17 Pressurized Water Reactor Spent Fuel Assembly under Complete Loss of Coolant Accident Conditions

Office of Nuclear Regulatory Research

AVAILABILITY OF REFERENCE MATERIALS IN NRC PUBLICATIONS

NRC Reference Material

As of November 1999, you may electronically access NUREG-series publications and other NRC records at NRC's Library at www.nrc.gov/reading-rm.html. Publicly released records include, to name a few, NUREG-series publications; *Federal Register* notices; applicant, licensee, and vendor documents and correspondence; NRC correspondence and internal memoranda; bulletins and information notices; inspection and investigative reports; licensee event reports; and Commission papers and their attachments.

NRC publications in the NUREG series, NRC regulations, and Title 10, "Energy," in the *Code of Federal Regulations* may also be purchased from one of these two sources.

1. **The Superintendent of Documents**
   U.S. Government Publishing Office
   Mail Stop IDCC
   Washington, DC 20402-0001
   Internet: bookstore.gpo.gov
   Telephone: (202) 512-1800
   Fax: (202) 512-2104

2. **The National Technical Information Service**
   5301 Shawnee Rd., Alexandria, VA 22312-0002
   www.ntis.gov
   1-800-553-6847 or, locally, (703) 605-6000

A single copy of each NRC draft report for comment is available free, to the extent of supply, upon written request as follows:

Address: **U.S. Nuclear Regulatory Commission**
Office of Administration
Publications Branch
Washington, DC 20555-0001
E-mail: distribution.resource@nrc.gov
Facsimile: (301) 415-2289

Some publications in the NUREG series that are posted at NRC's Web site address www.nrc.gov/reading-rm/doc-collections/nuregs are updated periodically and may differ from the last printed version. Although references to material found on a Web site bear the date the material was accessed, the material available on the date cited may subsequently be removed from the site.

Non-NRC Reference Material

Documents available from public and special technical libraries include all open literature items, such as books, journal articles, transactions, *Federal Register* notices, Federal and State legislation, and congressional reports. Such documents as theses, dissertations, foreign reports and translations, and non-NRC conference proceedings may be purchased from their sponsoring organization.

Copies of industry codes and standards used in a substantive manner in the NRC regulatory process are maintained at—

The NRC Technical Library
Two White Flint North
11545 Rockville Pike
Rockville, MD 20852-2738

These standards are available in the library for reference use by the public. Codes and standards are usually copyrighted and may be purchased from the originating organization or, if they are American National Standards, from—

American National Standards Institute
11 West 42nd Street
New York, NY 10036-8002
www.ansi.org
(212) 642-4900

Legally binding regulatory requirements are stated only in laws; NRC regulations; licenses, including technical specifications; or orders, not in NUREG-series publications. The views expressed in contractorprepared publications in this series are not necessarily those of the NRC.

The NUREG series comprises (1) technical and administrative reports and books prepared by the staff (NUREG–XXXX) or agency contractors (NUREG/CR–XXXX), (2) proceedings of conferences (NUREG/CP–XXXX), (3) reports resulting from international agreements (NUREG/IA–XXXX), (4) brochures (NUREG/BR–XXXX), and (5) compilations of legal decisions and orders of the Commission and Atomic and Safety Licensing Boards and of Directors' decisions under Section 2.206 of NRC's regulations (NUREG–0750).

U.S.NRC
United States Nuclear Regulatory Commission
Protecting People and the Environment

NUREG/CR-7215

Spent Fuel Pool Project Phase I:
Pre-Ignition and Ignition Testing of a Single Commercial 17x17 Pressurized Water Reactor Spent Fuel Assembly under Complete Loss of Coolant Accident Conditions

Manuscript Completed: July 2013
Date Published: April 2016

Prepared by:
S.G. Durbin, E.R. Lindgren and A.S. Goldmann
Sandia National Laboratories
Albuquerque, NM 87185

M. Zavisca, Z. Yuan, R. Karimi, A. Krall, and M. Khatib-Rahbar
Energy Research, Inc.
Rockville, MD 20847-2034

G. A. Zigh, NRC Technical Monitor
A. Velazquez-Lozada, NRC Project Manager
S. Gonzalez, NRC Project Manager

NRC Job Code N6777

Office of Nuclear Regulatory Research

ABSTRACT

The US Nuclear Regulatory Commission (NRC), in collaboration with the Organization for Economic Corporation and Development (OECD), and 12 international partners, conducted an experimental program to obtain experimental data for the characterization of hydraulic and ignition phenomena of prototypic light water reactor fuel assemblies in a spent fuel pool under complete loss of coolant accidents for validation of the MELCOR severe accident computer code. MELCOR is a fully integrated, engineering-level computer code whose primary purpose is to model the progression of postulated accidents in light water reactors as well as non-reactor systems (e.g., spent fuel pool and dry cask). The experimental program, were conducted in two phases at Sandia National Laboratories. The first phase, described in this NUREG, focused on axial heating and zirconium fire propagation in a single 17x17 PWR fuel assembly. The results from the first phase of the experiments demonstrate that the MELCOR computer code can accurately simulate ignition timing and burn propagation in a single 17x17 PWR assembly under complete loss of coolant conditions.

CONTENTS

LIST OF FIGURES

LIST OF TABLES

EXECUTIVE SUMMARY

In 2001, an evaluation of the potential accident risk in a spent fuel pool (SFP) at a US nuclear plant was performed. NUREG-1738, "Technical Study of Spent Fuel Pool Accident Risk at Decommissioning Nuclear Power Plants," describes a modeling approach for a typical decommissioning plant with design assumptions and industry commitments, the thermal hydraulic analyses performed to evaluate spent fuel stored in the SFP, the risk assessment of SFP accidents, the consequence calculations, and the implications for decommissioning regulatory requirements. Some of the assumptions in the accident progression were known to be necessarily conservative, especially the estimation of the fuel damage. The SFP accident research continued by applying best-estimate computer codes to predict the severe accident progression following various postulated initiators. These studies identified various modeling and phenomenological uncertainties that prompted a need for experimental confirmation.

Previous analyses have shown that fuel assemblies can ignite and propagate in a SFP during a complete loss of coolant scenario. Hence, qualified data obtained in representative fuel configurations were needed to confirm these results. In 2003, the NRC undertook an experimental program to address thermal-hydraulic conditions and zirconium fire propagation during a complete loss of coolant event in a boiling water reactor spent fuel pool. These experiments are summarized in NUREG/CR-7143. The experiments showed that the measured form and friction loss coefficients of a prototypic BWR assembly were significantly different from generally accepted values and that the use of the measured coefficients was vital for accuracy when calculating (with MELCOR) the naturally induced air flow rate. The incorporation of "breakaway" Zircaloy oxidation kinetics into MELCOR was also necessary to accurately capture the Zircaloy heat-up to ignition and oxygen consumption.

In May 2009, the NRC, in collaboration with the Organization for Economic Cooperation and Development/Nuclear Energy Agency (OECD/NEA) and 12 international partners signed an agreement called the "OECD/NEA Sandia Fuel Project - An Experimental Programme and Related Analyses for the Characterization of Hydraulic and Ignition Phenomena of Prototypic Water Reactor Fuel Assemblies." This program defined an experimental test matrix, experimental conditions and parameters to be examined with the overall objective being to perform a highly detailed thermal-hydraulic characterization of a full-length commercial fuel assembly mockup to provide data for the direct validation of severe accident computer codes (i.e., MELCOR). This experimental work was valuable to the OECD/CSNI community to facilitate severe accident code validation (ATHLET-CD, ASTEC, Ansys Fluent, DRACCAR, and MELCOR) and reduce modeling uncertainties within the codes. Further, it provided a collaborative exchange of information on severe accident modeling which resulted in increased knowledge to participating members that can be used in their regulatory programs and future research.

The study was conducted in two phases; Phase I (documented in this NUREG), focused on axial heating and burn propagation in a single assembly and Phase II (documented in NUREG/CR-7216) focused on axial and radial heating, burn propagation and the effects of fuel rod ballooning. Phase II consisted of a single heated assembly surrounded by four unheated assemblies representing a 1x4 loading pattern.

A single test assembly of a full-length commercial 17x17 PWR fuel bundle was constructed using prototypic, commercial components with heater rods made from zirconium alloy tubing supplied by an industrial vendor. The fuel assembly contains the core skeleton including eleven spacers permanently attached to twenty-five guide tubes and 264 fuel rods which pass through the spacers and are held captive in the assembly by the top and bottom nozzles. The assembly was placed into two different size pool racks during the testing. The test assembly was completely insulated to model boundary conditions representing a “hot neighbor” loading pattern. The test assembly was fully instrumented including hot wire anemometers (flow rate), oxygen sensors, gas chromatograph (Ar and N_2 quantification), quartz light pipes (visual observation), laser Doppler anemometer (velocity), pressure transducers and thermocouples.

Separate effects tests were performed to investigate the assembly hydraulic response. For these tests, the assembly was unheated, and flow was forced into the assembly covering the expected range of flow rates. Tests were performed and these values were computed for both pool rack cell sizes. The experimental data for flow rate and pressure drop was used to compute both the frictional and inertial flow resistance coefficients S_{LAM} and Σk (along with their associated uncertainties).

Pre-ignition tests were conducted using a uniform axial power profile with electrically heated rods to simulate decay powers from 0.5 to 3.5 kW (in steps of 0.5 kW). These tests were also performed with both pool rack cell sizes. The key parameters for these non-destructive tests are temperatures throughout the fuel assembly and inlet mass flow rate.

The ignition test was conducted at a simulated decay power of 5.0 kW and using the slightly larger pool rack cell size. The power is equivalent to an offload age of approximately 17 months (assuming fuel burn up of 45 GWd/MTHM). Ignition of the Zircaloy within the assembly was first indicated at an elapsed test time of 12 hours 40 minutes. Power to the assembly was lost shortly after ignition occurred.

During the ignition test, a residual gas analyzer (RGA) was used to monitor the amount of nitrogen and argon exiting the top of the assembly. The ratio of nitrogen to argon was used to determine if nitrogen was being consumed by reaction with zirconium. While encountering some sampling difficulties, the RGA successfully measured a significant amount of nitrogen consumption at the start of ignition and during the burn front progression to the bottom of the assembly. The single point calibration with air was used for samples containing significant concentrations of oxygen. The analysis of two additional calibration gases allowed adjustment of the air calibration for samples that were devoid of oxygen. During the burn phase, all of the oxygen was removed from the air drawn into the assembly converting 14 percent of the initial

zirconium to ZrO_2. Depending on which background ratio was assumed, between 20 percent to 40 percent of the zirconium in the assembly was converted to ZrN. These results indicate that the hot oxygen starved environment remaining after the passage of the burn front is ideal for significant zirconium nitride formation.

A MELCOR model representing the test assembly was developed consisting of a stack of 10 control volumes and 17 axial core levels in a single radial ring (12 axial levels along the heated length of the rods). This MELCOR model was used to simulate both the pre-ignition and ignition tests.

For the pre-ignition tests with the smaller pool rack cell size (Cell 1), the MELCOR model with the base S_{LAM} and Σk parameters over predicted the induced air inlet mass flow rate, resulting in a slight under prediction of the assembly temperatures. To improve the results, the value of S_{LAM} used was increased from 132 to 145 (at the top end of the uncertainty range). This resulted in the mass flow rate predictions falling within the experimental data uncertainty range for all power levels and improving the temperature response so that MELCOR is within 19K (34°F) of the measured test data. For the pre-ignition tests with the larger pool rack cell size (Cell 2), the MELCOR model with the base S_{LAM} and Σk parameters shows excellent agreement for both induced air inlet mass flow rate and temperatures. MELCOR calculated temperatures are within 7K (13°F) of the experimental data for all power levels. The MELCOR computed mass flow rates were within the experimental data uncertainty range for all power levels.

For the 5.0 kW ignition test, MELCOR shows excellent agreement for the peak cladding temperature in the assembly, and accurately captures the ignition time. Just prior to the ignition, MELCOR was over predicting the temperature throughout the assembly. This was traced to MELCOR over predicting the oxidation rate. Earlier in the transient, MELCOR was accurately predicting the peak cladding temperature in the assembly, however, had a tendency to over predict the temperature in the lower portion of the assembly. The MELCOR predicted mass flow rate shows excellent agreement to the experimental test data up until the time of ignition, after which time, the MELCOR mass flow rate shows significant oscillations. Overall, MELCOR is capable of accurately predicting the induced mass flow rate, peak cladding temperature and ignition time for a single assembly in a spent fuel pool under complete loss of coolant conditions. Additional MELCOR analyses were performed to investigate axial and radial nodalization. The addition of nodes in both the axial and radial directions did not result in changes to the overall results, implying that there are a sufficient number of nodes in the base case model.

ABBREVIATIONS

ANL	Argonne National Laboratory
BSA	burst signal analyzer
BWR	Boiling Water Reactor
CFD	computational fluid dynamics
COR	MELCOR Core Package
CVH	MELCOR Control Volume Hydrodynamics Package
DAQ	data acquisition
D_H	hydraulic diameter
ID	inside diameter or dimension
LDA	laser Doppler anemometer
LOCA	Loss of Coolant Accident
MELCOR	severe accident analysis code
NEA	Nuclear Energy Agency
NRC	Nuclear Regulatory Commission
NS	Non-supporting Structure
OECD	Organization for Economic Co-operation and Development
PCT	peak cladding temperature
PID	Proportional-integral-derivative
PWR	pressurized water reactor
RGA	residual gas analyzer
SCR	silicon-controlled rectifier
SFP	spent fuel pool
SFPP	Spent Fuel Pool Project
slpm	standard liters per minute (standard defined at 0ºC and 1 atm)
SNL	Sandia National Laboratories
TC	Thermocouple

1 INTRODUCTION

The testing in Phase I of the spent fuel pool (SFP) project focused on axial heating and burn propagation. The near-prototypic test assembly was constructed to represent a commercial 17×17 PWR fuel bundle. The various components comprising a typical 17×17 PWR assembly are illustrated in Figure 1.1. The main structural component of the assembly is the core skeleton, which consists of eleven spacers permanently attached to twenty-five guide tubes. The 264 fuel rods pass through the spacers and are held captive in the assembly by the top and bottom nozzles.

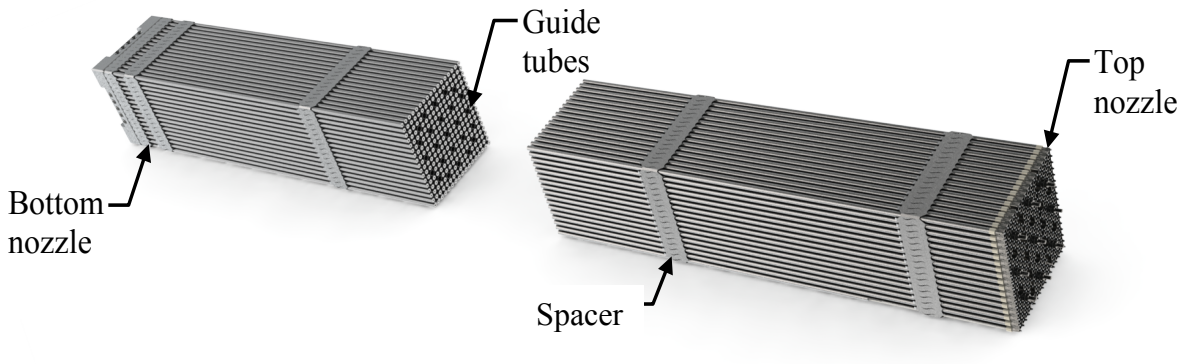

Figure 1.1 Various components in a typical 17×17 PWR fuel assembly

The single full-length, electrically heated PWR assembly was fabricated using prototypic, commercial 17×17 PWR components and 9.50 mm (0.374 in.) heater rods made from 11.18 mm (0.44 in.) Zircaloy-2 tubing supplied by an industrial vendor. The as-built heater rod diameter of 9.50 mm (0.374 in.) is slightly smaller than the typical PWR design value of 9.53 mm (0.375 in.) but is not expected to significantly affect system hydraulics. The heater rods were manufactured by a commercial vendor using the same fuel rod simulator design and Zircaloy-2 material that was highly successful in the BWR study (Ref. 1). An oxidation kinetics study was performed that showed no difference between the Zircaloy-2 used to make the heaters and Zircaloy-4 used in prototypic PWR fuel rods (Ref. 2). The spent fuel rod simulators for Phase I had a linear power profile and a maximum output of 15.8 W/m (4.8 W/ft), which was three times greater than expected to produce ignition.

Two storage cell sizes were fabricated for study in Phase I testing. Cell 1 had an inner dimension (ID) of 221.3 mm (8.7 in.) and was chosen to match the middle-sized cell in the PWR hydraulic characterization study (Ref. 3). Cell 2 had an inner dimension of 223.4 mm (8.8 in.) and was chosen to match the cell size in the pool rack to be used in Phase II testing. A series of eight pre-ignition tests were conducted for each cell to determine the thermal-hydraulic response of the mock-spent fuel assembly. In addition, MELCOR simulations were performed for each of these pre-ignition tests for both cells and the ignition test of Cell 2. MELCOR sensitivity analyses were also conducted to examine the effect of using more refined discretization.

2 EXPERIMENTAL APPARATUS AND PROCEDURES

2.1 Flow Measurements and Calibrations

2.1.1 Assembly Hydraulics

A single pressure port was installed near the bottom of the storage cell to allow isothermal pressure drop measurements to determine the hydraulic loss coefficients of the apparatus with unheated rods. The location of this pressure port is detailed in Section 2.3.2. Figure 2.1 shows the overall assembly pressure drop of the Cell 1 (221.3 mm ID) configuration as a function of average air velocity (with the guide tubes plugged). The S_{LAM} and Σk as determined from the quadratic fit of the data are 132 and 29.2, respectively. Figure 2.2 shows two simultaneous measurements of the overall assembly pressure drop for the Cell 2 (223.4 mm ID) configuration as a function of average air velocity. The S_{LAM} and Σk, as determined from the quadratic fit of the data, are 146 and 24.8, respectively. Appendix A summarizes calculations and definitions for S_{LAM} and Σk. Thermocouples were not installed during these forced flow hydraulic tests.

The dependence of the hydraulic parameters on the storage cell size differs from that determined during the PWR hydraulic characterization study (Ref. 3). The previous hydraulic characterization was conducted with a prototypically ideal PWR assembly. As the storage cell size increased, the S_{LAM} decreased significantly and Σk decreased minimally with a net result that hydraulic resistance decreased. With the Phase I PWR assembly, the S_{LAM} and Σk are comparable within the calculated uncertainties, as the cell size did not change significantly. Figures 2.1 and 2.2 show the measured pressure drop as a function of velocity based on separate measurements ($\Delta P1$ and $\Delta P2$). Comparing Figure 2.1 and Figure 2.2 at high velocity (1.6 m/s (5.25 ft/s)), the pressure drop with Cell 2 is only slightly lower than with Cell 1. At 0.8 m/s (2.62 ft/s) and lower, there is little discernible difference between the pressure drop in Cell 1 and Cell 2. The velocity range of interest for complete loss-of-coolant conditions is on the order of 0 to 0.25 m/s (0 to 0.82 ft/s).

The uncertainties in the hydraulic measurements are detailed in Appendix A, Error Propagation Analysis. Unless otherwise noted, the uncertainties quoted throughout this report refer to the expanded uncertainties, which give the 95 percent confidence level that the measurement lies within the cited bounds. The uncertainty in the average assembly velocity is ± 0.078 m/s (± 0.256 ft/s). The uncertainty in the pressure measurement is ± 0.1 N/m^2 ($\pm 1.45 \cdot 10^{-5}$ psi). The estimated uncertainty in the flow loss coefficients is ± 13 and ± 1.4 for S_{LAM} and Σk, respectively. Table 2.1 presents a summary of the hydraulics for both Cell 1 and 2. The as-built, average diameter of the simulated fuel rods was 9.5 mm (0.374 in.). The presence of the thermocouples was considered in calculating the flow area and hydraulic diameter. The average number of thermocouples at any given height in the assembly is 60, each with an outer diameter of 0.79 mm (0.031 in.). The decrease to the flow area with the inclusion of the thermocouples is approximately 0.1 percent of the non-instrumented flow area. These thermocouples were bundled into four groups that added an estimated 41 mm (1.6 in.) of wetted perimeter, or 0.4 percent of the total wetted area.

Major differences between the hydraulic assembly and the heated assembly are the presence of thermocouples and a slight randomly oriented curvature present in the heater rods in the heated assembly. Variation in the spacing between adjacent rods is evident in the velocity profile measurements discussed in Section 4.3. The heater rods to be used in the Phase II testing will be mechanically straightened in an effort to make them more ideally prototypic.

Additional hydraulic characterization will be conducted on the center heated assembly as well as the unheated peripheral assemblies to examine the issues of rod straightness and presence of thermocouples.

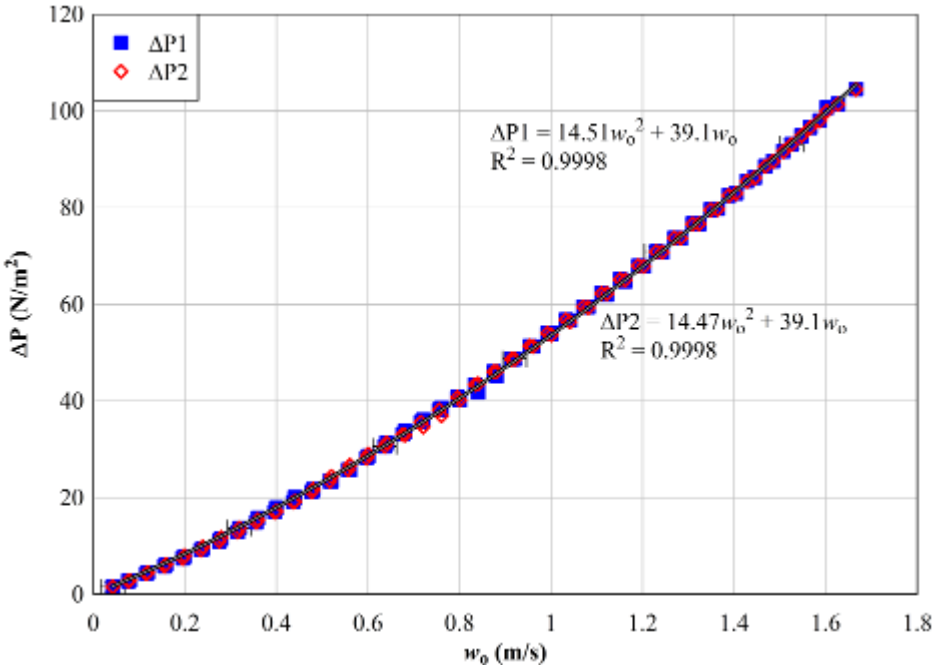

Figure 2.1 **Overall pressure drop as a function of average air velocity in the assembly for the 221.3 mm storage cell (Cell 1)**

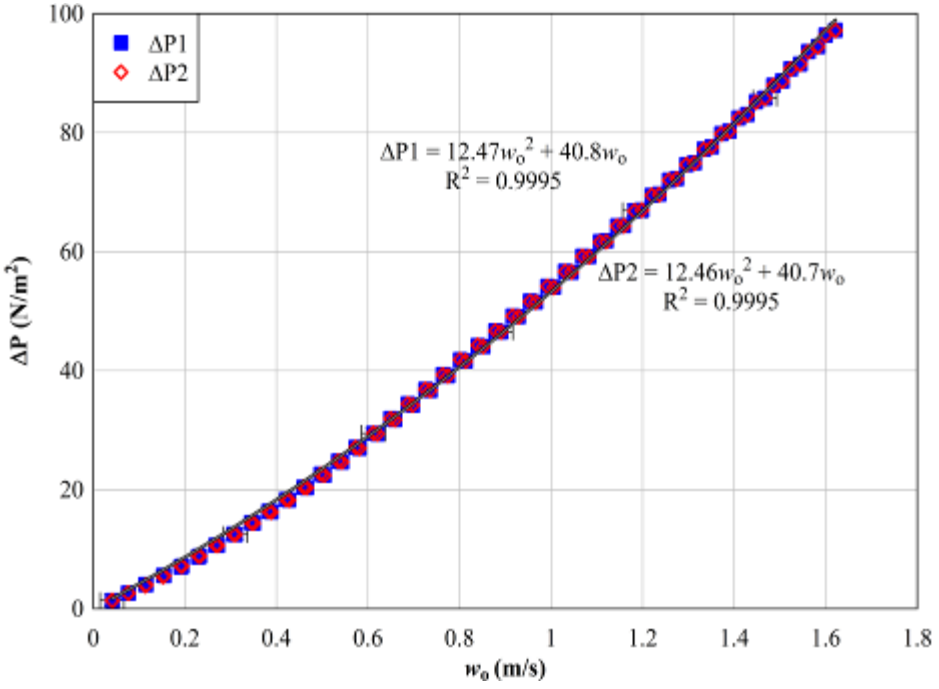

Figure 2.2 **Overall pressure drop as a function of average air velocity in the assembly for the 223.4 mm storage cell (Cell 2)**

Table 2.1 Summary of assembly hydraulics for storage Cell 1 and Cell 2

Description	Cell 1	Cell 2
Inner Dimension (mm)	221.3	223.4
Flow Area (m^2)	0.0273	0.0283
Hydraulic diameter, D_H (mm)	11.2	11.6
S_{LAM}	132	146
Σk	29.2	24.8

2.1.2 Hot Wire Anemometer at the Assembly Inlet

A hot wire anemometer was placed in the 154 mm (6.065 in.) ID pipe that defines the inlet to the test assembly. A hot wire anemometer was chosen to measure the inlet flow rate because this type of instrument is sensitive and robust while introducing almost no unrecoverable pressure loss. The placement of the hot wire is shown in Figure 2.3. A TSI Model 8455 hot wire anemometer was used for these tests. A honeycomb element was added to the inlet entrance to reduce the influence of any air flow disturbances within the experimental enclosure on the hot wire measurements.

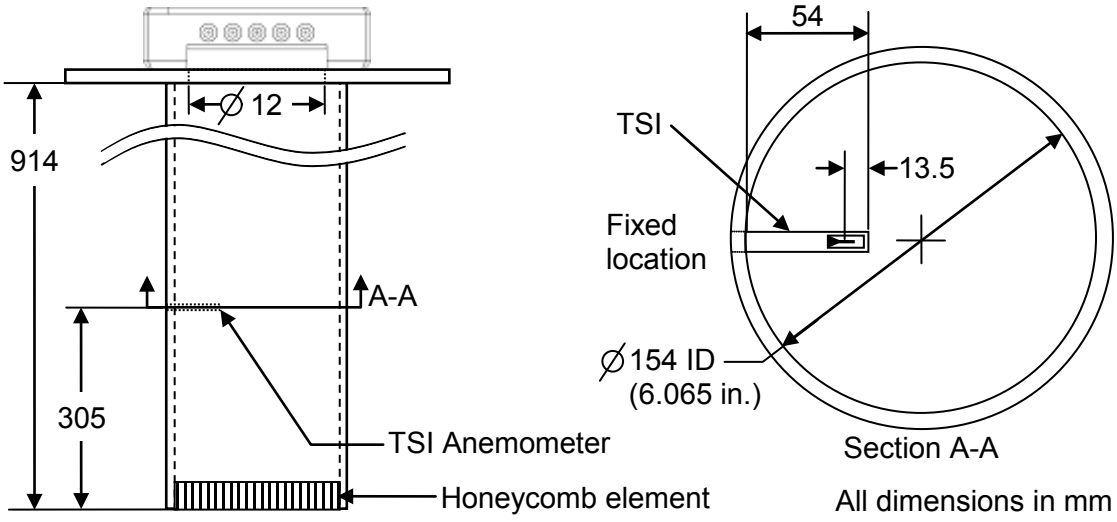

Figure 2.3 Schematic showing the layout of the inlet hot wire

A series of unheated calibration runs were performed to calibrate the output of the hot wire anemometer. Air flows were metered into the bottom of the assembly via the inlet pipe and the response of the anemometer was recorded for each flow rate. A least-squares regression was performed for each pool cell configuration as shown in Figure 2.4. These linear coefficients were used to determine the indicated flow rate from the hot wire anemometer during heated testing. Although the data for the two pool cells give different calibration coefficients, the apparent flow rates from both calibration curves are well within the uncertainty of the measurement of ±12 slpm, especially for flow rates in the observed range of testing (< 250 slpm).

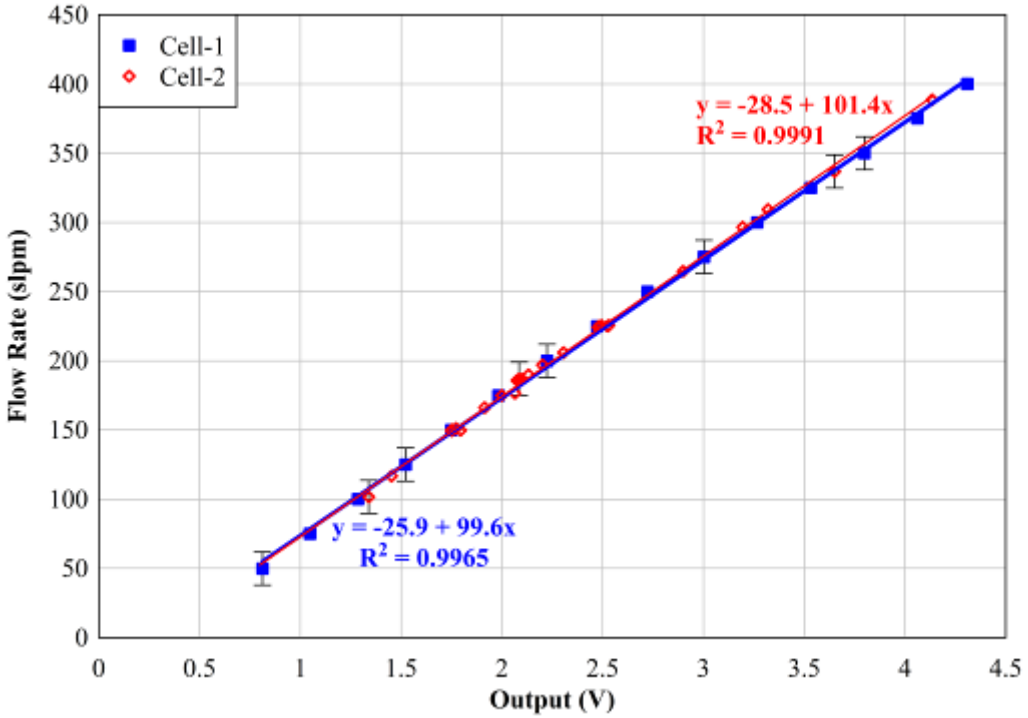

Figure 2.4 Flow rate as a function of the TSI Model 8455 hot wire anemometer voltage

2.1.3 Laser Doppler Anemometry Measurements

Laser Doppler anemometry (LDA) is a non-intrusive, optical technique used to measure the instantaneous velocity in a flow field at the intersection of two coherent laser beams. The most common method of LDA used at present is the dual-beam anemometer system. Typically, a single laser beam is split into two mutually coherent polarized light waves, which intersect to form a spheroid-shaped region called the measuring volume. Particles passing through the measuring volume with a given velocity scatter light from the light beams to produce the LDA signal. For the investigations detailed herein, a dual-beam system operating in backscatter mode as shown in Figure 2.5 was used. The photodetector was a photomultiplier (PM), and a Bragg cell was used to introduce a reference frequency, allowing the measurement of near-zero velocities. The signal was then processed in a burst analyzer and sent to a PC-based data acquisition system.

LDA measurements were initially planned for the Cell 1 configuration only. However, failure of the burst signal analyzer (BSA) during Cell 1 efforts forced these measurements to be collected during Cell 2 pre-ignition testing. The data collected are of the same nature for Cell 2 as it would have been for Cell 1 with only a slightly larger cell ID. This change to the original test plan was necessary to prevent further delay to the project and does not significantly affect the technical content.

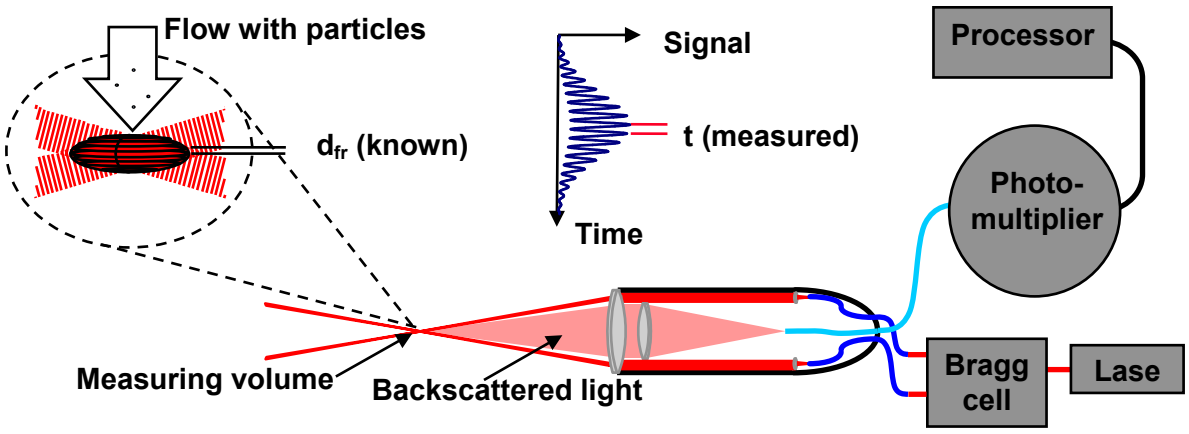

Figure 2.5 Dual-beam backscatter LDA system components and principles

The average velocity profiles were measured in these experiments by a single-component laser-Doppler anemometer (Dantec 1-D FlowExplorer). This LDA system is composed of the FlowExplorer probe head, a photomultiplier, a burst analyzer, a motorized stage and controller unit, a PC-based data acquisition (DAQ) system, and data processing software. These components are listed in Table 2.2.

Table 2.2 Detailed list of the LDA system components

Description	Manufacturer	Serial Number
FlowExplorer probe head	Dantec Dynamics	0115
BSA F60 – Burst analyzer	Dantec Dynamics	437
Photomultiplier	Dantec Dynamics	119
1-D Stage	Isel Automation	505
1-D Stage controller	Isel Automation	502
DAQ – PC	Dell	F51KYD1

Figure 2.6 shows the layout of the test components for LDA measurements. The LDA probe is mounted externally to the PWR assembly on a motorized stage. The laser beams pass through the optical window into the assembly and measures the velocity at the intersection of the beams. In this manner, the local velocity can be measured across the assembly in between rod banks. All measurements in this report were collected between the rod banks identified in Figure 2.6 at z = 0.442 m (17.4 in.). Figure 2.7 gives three photographs of the LDA setup. These photographs depict a measurement just inside the optical window. The rubber coupling shown in Figure 2.7c was connected to the flow conditioner for pressure drop measurements, hot wire calibrations, and forced flow velocity profile baselines. Further details of the flow conditioner, flow metering system, and LDA may be found in the PWR hydraulic characterization study (Ref. 3).

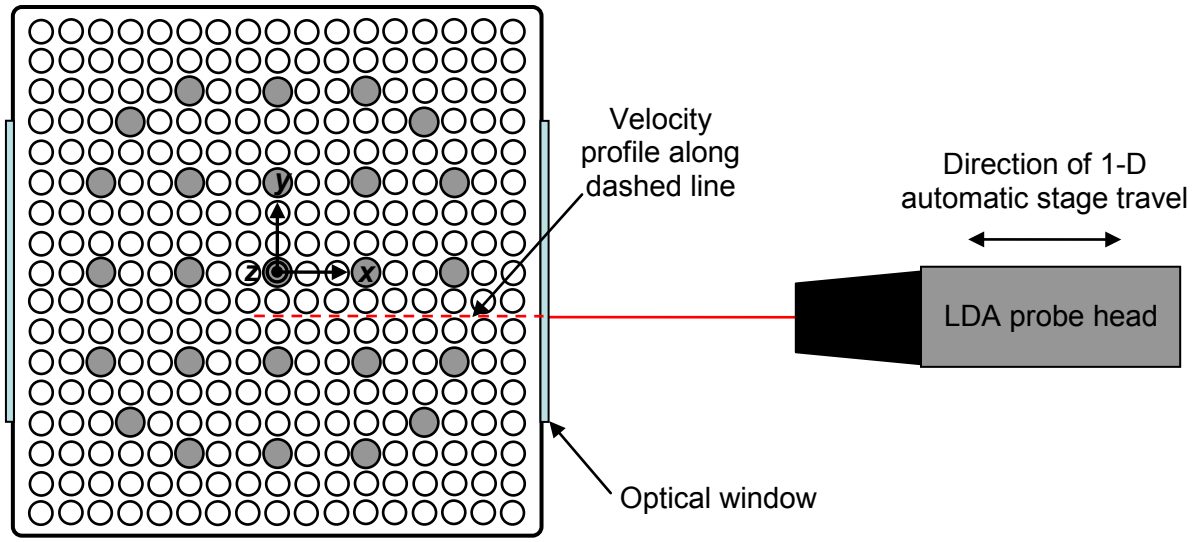

Figure 2.6 **Schematic of the LDA system for measuring velocity profiles in the PWR 17×17 assembly**

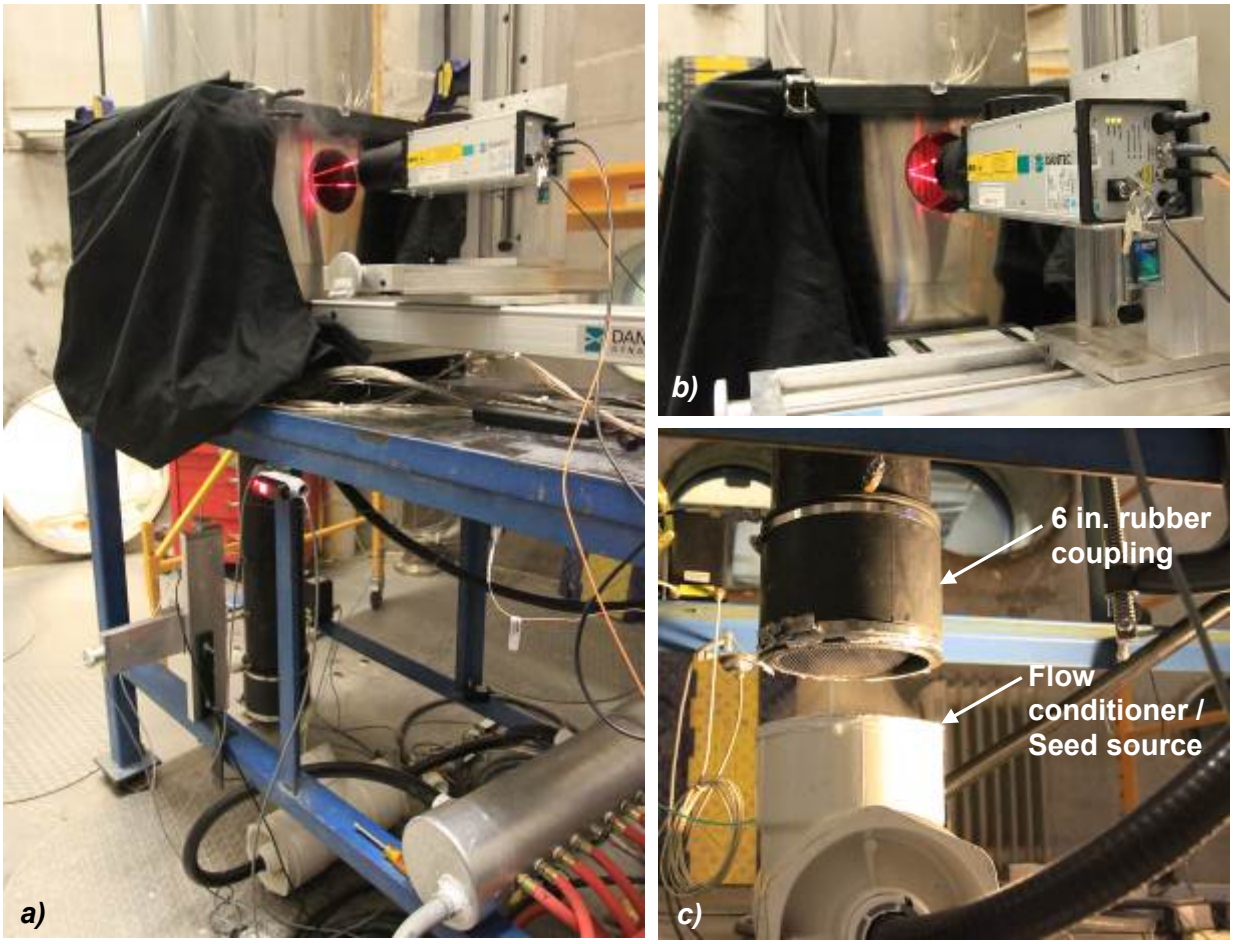

Figure 2.7 **Photographs showing the *a*) overall LDA setup, *b*) close-up of the probe head and optical window, and *c*) flow inlet and seed source**

2.2 Thermocouple Layout

Thermocouples (TCs) were installed throughout the assembly to measure thermal response during heat up. The TC layout was unchanged between the Cell 1 and the Cell 2 configurations. A total of 131 TCs were installed on the guide tubes and heater rods. The top 11 TCs, representing those at z = 3.759 and 3.934 m (148 and 154.875 in.), exited the top of the assembly. The remainders of TCs were routed through the bottom of the assembly. All of Phase I testing utilized these internal TCs. Figure 2.8 shows the layout and identification scheme of these TCs. An additional 60 TCs were placed on the storage cell (30) and the thermal radiation barrier (30). The thermocouples were placed 15.24 cm (6 in.) apart along the storage cell and thermal radiation barrier. These TCs were designated by their physical orientation, e.g. Pool_N_F_27" was a pool TC on the North face at an elevation of 0.686 m (27 in.) and Rad_SE_C_52" was a radiation barrier TC on the Southeast corner at an elevation of 1.321 m (52 in.). Other TCs were placed to measure temperatures of interest such as flow inlet and ambient temperature.

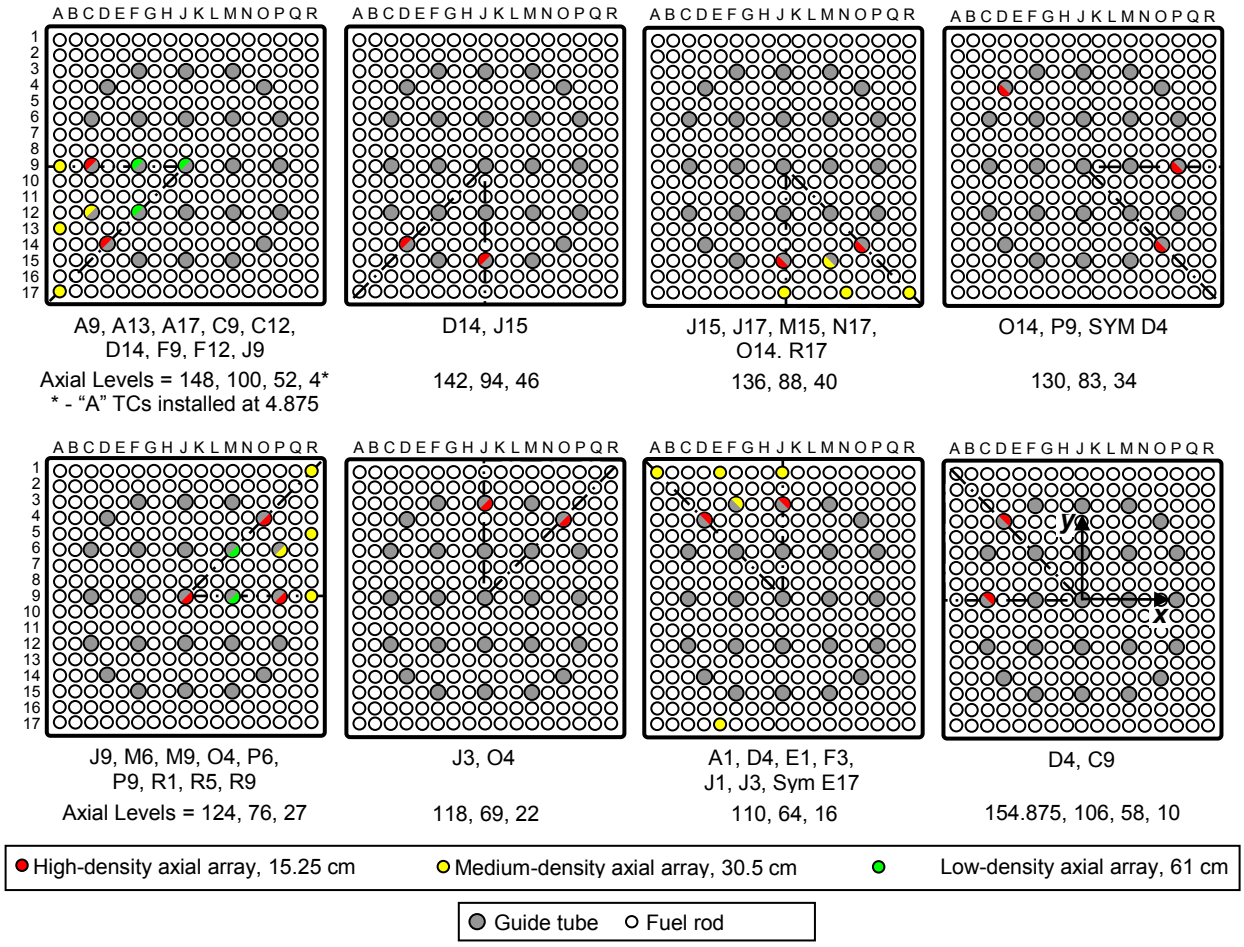

Figure 2.8 Thermocouple layout for the Phase I test assembly

Note: Thermocouples were installed using US customary units. The data file headers and TC identifiers give positioning in inches, e.g. J_9_124" is installed on the middle instrument tube at z = 124 in. (3.150 m).

TCs were attached to the assembly by spot welding Nichrome ribbon over the thermocouple sheath as shown in Figure 2.9. An additional piece of Nichrome was attached a short distance away from the tip of the TC to provide strain relief. All TCs used in this testing were ungrounded, K-type with a 0.813 mm (0.032 in.) Super Omegaclad XL sheath diameter. The majority of the TCs used were Omega Engineering part number TJ192-CAXL-032U-192-SMPW-M.

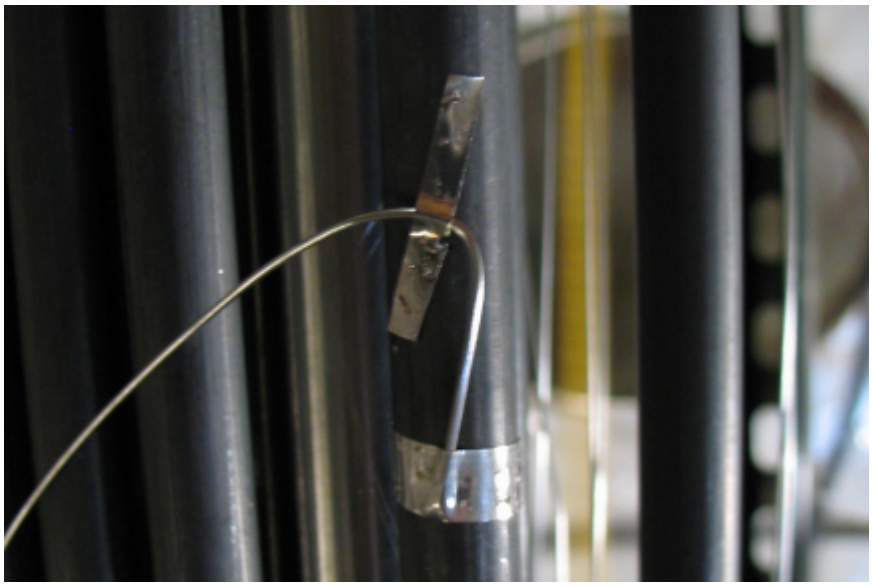

Figure 2.9 Detail view showing TC attachment to a fuel rod

2.3 General Construction

2.3.1 Power Control

Figure 2.10 shows the configuration of the power control system for the SFP Phase I test series. The data acquisition (DAQ) system generates a power set point based on user input via a LabVIEW graphical user interface. This set point signal is relayed to a proportional-integral-derivative (PID) controller. The PID controller determines an appropriate power control signal by comparing the power set point to the feedback signal from the system Watt transducer. The silicon controlled rectifier (SCR) power controller receives the control signal and allows the prescribed electrical power into the resistive load of the test assembly.

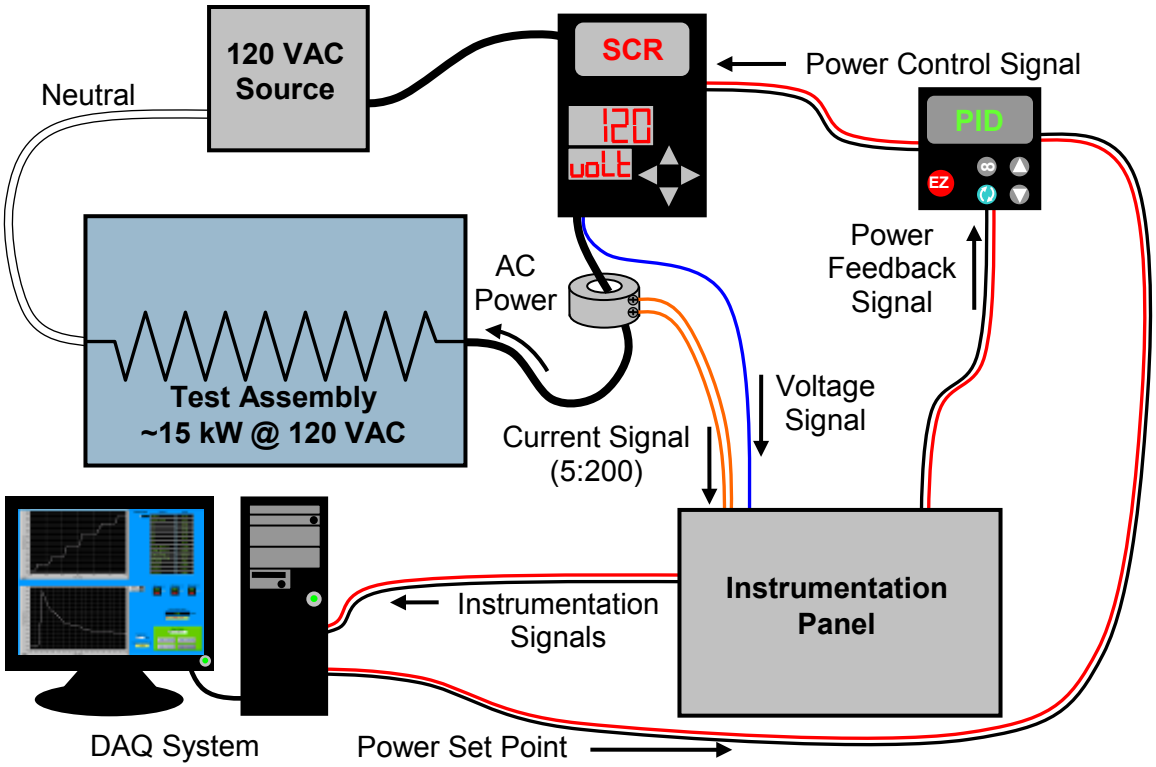

Figure 2.10 Power control system and test circuit

The internal layout of the instrumentation panel is shown in Figure 2.11. The transducers measure power, voltage, and current applied to the assembly. The signal from the Watt transducer is output to the DAQ and the PID controller as a feedback signal. The components used in this testing are listed in Table 2.3.

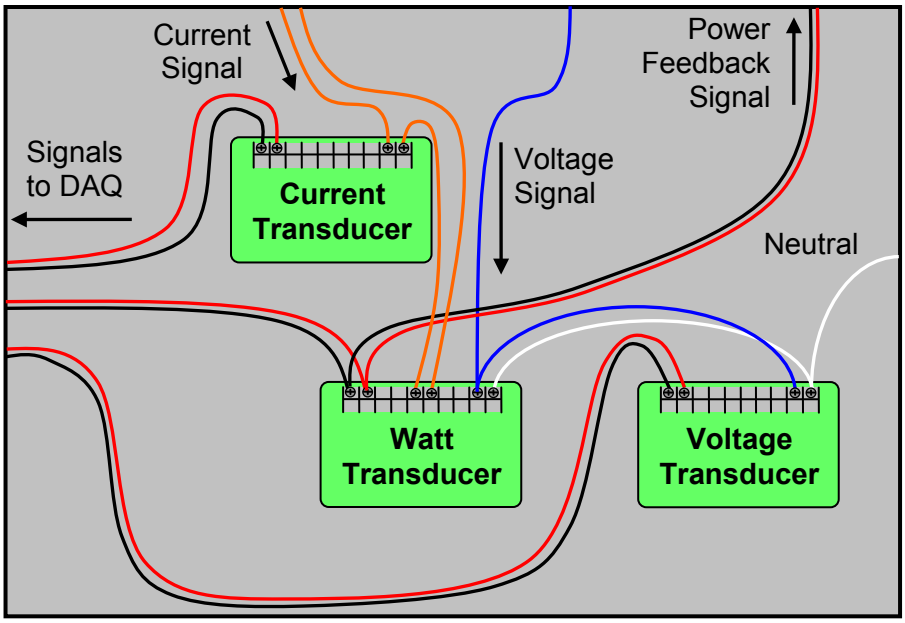

Figure 2.11 Schematic of the instrumentation panel

Table 2.3 List of equipment used for power control

Description	Manufacturer	Model
AC Watt Transducer	Ohio Semitronics	PC5-001D
AC Voltage Transducer	Ohio Semitronics	3VTR-001D
AC Current Transducer	Ohio Semitronics	3CTR-010D
PID Controller	Watlow Electric Manufacturing	PM6C1FJ1RAAAAA
SCR Power Controller	Watlow Electric Manufacturing	PC91-F25A-1000

2.3.2 Instrumentation External to the Assembly

Figure 2.12 shows the location of external instrumentation. All dimensions are referenced from the bottom of the bottom nozzle (z = 0). A single pressure port was located at z = 0.011 m (0.43 in.) to calculate the overall assembly pressure drop using atmospheric pressure as the reference pressure. These pressure drops were used to determine the S_{LAM} and Σk of the as-built assembly. The laser-Doppler anemometer (LDA) was located mid-bundle between the bottom nozzle/debris catcher and the first spacer. Also, quartz light pipes were placed approximately every 0.3048 m (1 ft) for visually observing the burn front. Three sample tubes were placed at the exit of the assembly. An exhaust air temperature was measured using a TC inserted into one of the tubes with the exit air drawn across the TC junction. The other bundle and annulus sample tubes supplied the two oxygen concentration transmitters (Advanced Micro Instruments, Model 65, Part 6ANA0056). An additional slip stream from the bundle sample tube was diverted to the residual gas analyzer (RGA) to measure relative concentrations of oxygen and nitrogen to the argon present in the assembly exhaust.

A schematic of the sampling system is provided in Figure 2.13. Two vacuum pumps were used to draw the samples from the top of the assembly. The main vacuum pump was used to pull relatively high volumetric flow rates through the sample tubes in order to reduce residence time of the samples. The secondary vacuum pump was used to pull slip stream samples for the oxygen concentration transmitters and the RGA. The RGA had a resident vacuum system internal to the instrument to provide a final sample stream.

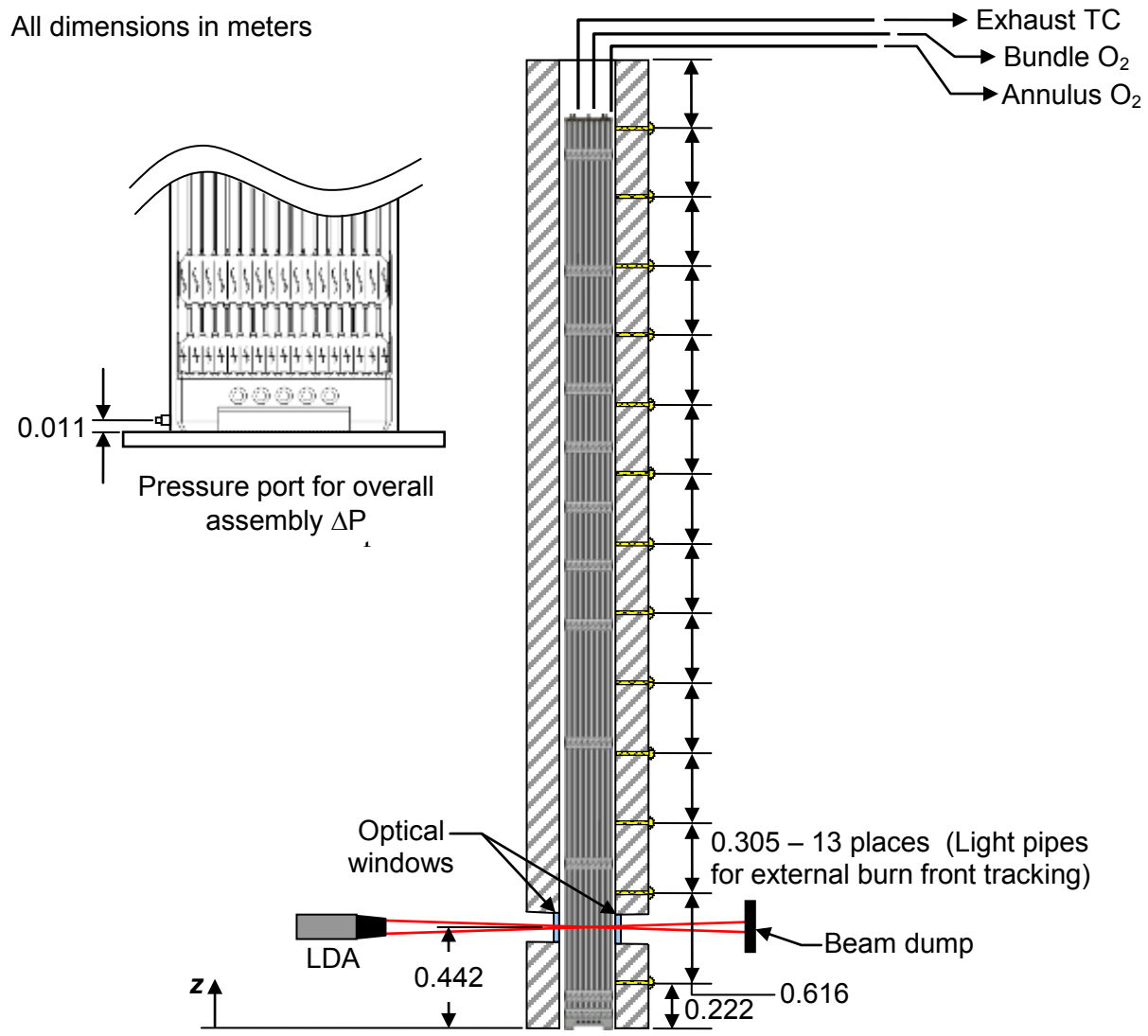

Figure 2.12 PWR test assembly and external instrumentation

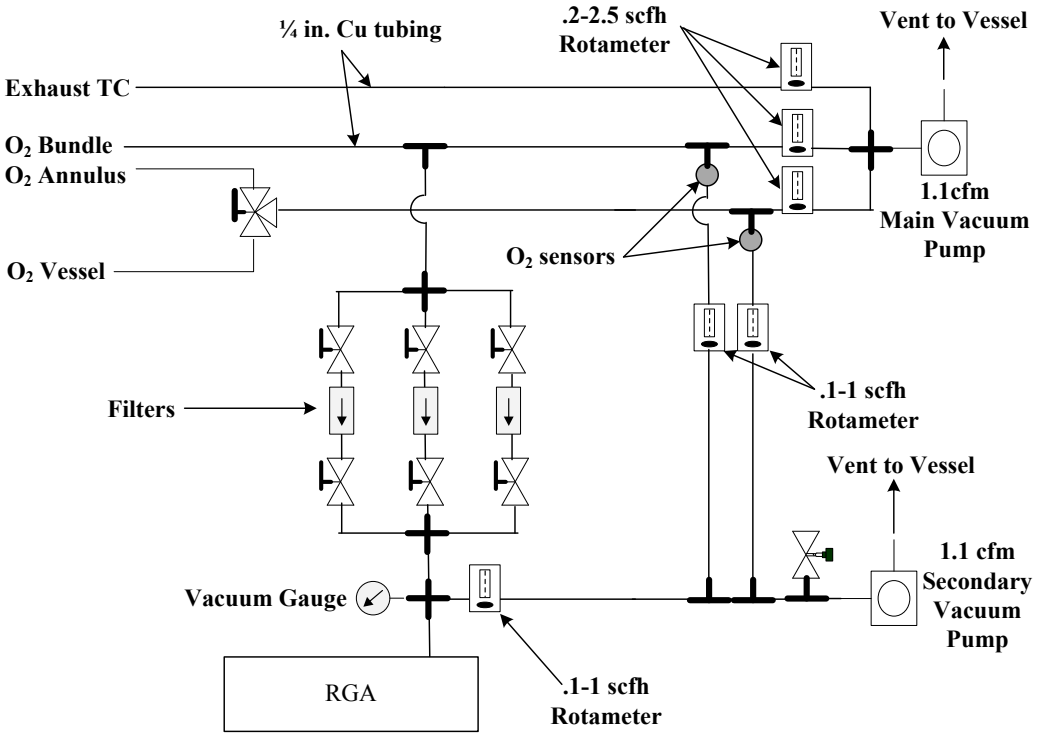

Figure 2.13 Schematic of the assembly exhaust sampling system

The amounts of nitrogen, oxygen, and argon in the exhaust stream directly above the test bundle were measured with a Pfeiffer RGA (Model GSD 300T). This instrument employed a heated quartz capillary for sampling air at ambient pressures (83 kPa (12 psi)). The standard instrument configuration contains a tungsten filament for ionizing the sample and a quadruple mass spectrometer for detection. A single ion (amu 28, 32, 40) was used to monitor for each gas. Data was recorded at 10 second intervals over the duration of the test. Before the test started, the instrument was tuned to reduce signal drift. Data were recorded in terms of detector current and then converted to a mole or volume fraction based on the analysis of ambient air, which served as a single point calibration gas. After initial evaluation of the ignition test data, two additional calibration gases were analyzed using the RGA. The first calibration gas was 1.22 percent argon in nitrogen. The other calibration gas was 4.76 percent argon in nitrogen. These additional calibration gases spanned ranges of interest as determined during post-test analyses of the RGA data.

The detector current for each of the three major gas species was normalized by the sum of the three detector currents. Since the three gas species ionized with different efficiency, correction factors are required to adjust the current ratios into volume fraction of each of the gas species. Assuming ambient air is 0.78084 N_2, 0.20946, O_2 and 0.00934 Ar. The correction factors determined on the day of the ignition test were 0.957, 1.153, and 2.401, respectively.

Samples were drawn through ceramic tubes at the top of the assembly at two independent locations, one from the center of the bundle just above the electrical bus plate and the other from the annular region between the storage cell and the outer perimeter of the bundle just below the electrical bus plate. The bus plate was located 0.173 m (6.82 in.) below the top of the storage cell. The sample for the RGA analysis was initially configured to be drawn from the center bundle location. Later, an additional sampling point was added at the annulus.

3 CELL 1 PRE-IGNITION TESTING AND ANALYSIS

The tests were performed using a uniform power profile with electrically heated rods. The pre-ignition tests were performed for seven different power levels, varying from 0.5 kW to 3.5 kW. The power was maintained constant during the tests. All tests were performed for a period of 12 hours, except the two 1 kW tests, which were conducted for a period of 20 hours. A 0.1524 m (6 in.) layer of Kaowool insulation was installed around the cell and wrapped with a 0.9 mm (0.036 in.) thick sheet of stainless steel. In the pre-ignition tests, the assembly was cooled by natural circulation. During the tests, the pressure and air inlet temperature were maintained at the ambient conditions of Albuquerque, NM.

A summary of the pre-ignition testing results for Cell 1 are presented in Table 3.1. This table gives the average temperatures and flow rates at 3, 6, 9, and 12 hours for z = 3.150 m (124 in.). The minimum and maximum temperatures of the bundle at each time are also shown.

The 1.0 kW test was run twice, as shown in the second and third columns of test entries in Table 3.1, to examine repeatability. The temperatures were within 3 K (5.4°F) at all positions and times, which is slightly greater than the experimental uncertainty of ±2.2 K (±4.0°F). The air flow rates were within 12 slpm for the two measurements, which is equal to the experimental uncertainty of ± 12 slpm.

Table 3.1 Summary of pre-ignition testing results for Cell 1 at z = 3.150 m (124 in.)

		True RMS Power (W)	500	1000	1000	1500	2000	2500	3000	3500
		Test Date	10/27/2010	10/12/2010	11/08/2010	10/22/2010	10/21/2010	10/20/2010	10/19/2010	10/18/2010
3 hrs		Flow Rate (slpm)	56	116	128	145	164	175	176	184
	Bundle	Min. Temp. (K)	320	343	344	365	392	411	438	455
		Max. Temp. (K)	327	359	359	388	422	445	479	503
		Avg. Temp. (K)	324	352	353	379	409	430	461	482
	Pool Cell	Avg. Temp. (K)	316	336	336	356	380	398	425	437
	Rad. Barrier	Avg. Temp. (K)	302	301	296	297	298	298	301	301
	Ambient	Avg. Temp. (K)	301	300	295	295	296	296	297	298
6 hrs		Flow Rate (slpm)	114	155	156	174	183	183	184	181
	Bundle	Min. Temp. (K)	343	386	388	429	474	513	559	594
		Max. Temp. (K)	354	410	410	459	510	552	600	645
		Avg. Temp. (K)	349	399	400	445	493	534	581	621
	Pool Cell	Avg. Temp. (K)	339	379	380	421	465	503	550	580
	Rad. Barrier	Avg. Temp. (K)	300	302	299	300	304	306	310	312
	Ambient	Avg. Temp. (K)	298	299	296	295	298	298	299	300
9 hrs		Flow Rate (slpm)	138	172	165	181	182	182	176	170
	Bundle	Min. Temp. (K)	363	425	426	483	545	599	661	718
		Max. Temp. (K)	377	452	450	515	579	636	698	756
		Avg. Temp. (K)	371	440	439	500	563	619	682	739
	Pool Cell	Avg. Temp. (K)	359	418	420	477	538	593	656	708
	Rad. Barrier	Avg. Temp. (K)	300	304	303	304	309	316	321	324
	Ambient	Avg. Temp. (K)	297	299	297	295	297	300	300	300
12 hrs		Flow Rate (slpm)	149	175	165	181	179	173	168	158
	Bundle	Min. Temp. (K)	381	458	457	526	598	665	738	820
		Max. Temp. (K)	396	487	484	559	634	702	775	850
		Avg. Temp. (K)	390	474	472	544	617	685	759	838
	Pool Cell	Avg. Temp. (K)	377	451	453	522	594	662	736	809
	Rad. Barrier	Avg. Temp. (K)	301	307	307	309	315	323	331	338
	Ambient	Avg. Temp. (K)	296	299	298	297	297	300	301	300

A MELCOR input model was developed containing 10 control volumes and 17 axial core levels (12 heated) in a single radial ring. Details about the MELCOR input model can be found in Appendix C. MELCOR version 1.86.yv.3084 was used for the analyses.

The experimental data of Cell 1 was compared with two MELCOR models using the values of 132 for S_{LAM} (as shown in Table 2.1) and a S_{LAM} of 145 (which includes the uncertainty of +13). A value of 30 for Σk was used in both cases. Figure 3.1 shows the comparison of temperature for the pre-ignition tests at t = 12 hrs. The model agrees with the measured temperatures within 19 K (34°F) for the S_{LAM} of 145 and within 35 K (63°F) for the S_{LAM} of 132 case for all powers.

Figure 3.2 shows the comparison of the airflow rates for the pre-ignition tests and MELCOR at t = 12 hrs. The model agrees with the measured flow rate to within 8 slpm for the S_{LAM} of 145 and 30 slpm for the S_{LAM} of 132 case for all powers. This flow rate includes the air flow through the bundle and the annulus. The increased MELCOR flow rate leads directly to the model under predicting the assembly temperature. As shown in Figures 3.1 and 3.2, temperature and mass flow predictions for a S_{LAM} value of 145 agrees favorably with experimental data as compared to the predictions using S_{LAM} of 132. As such, a S_{LAM} value of 145 is recommended for Cell 1.

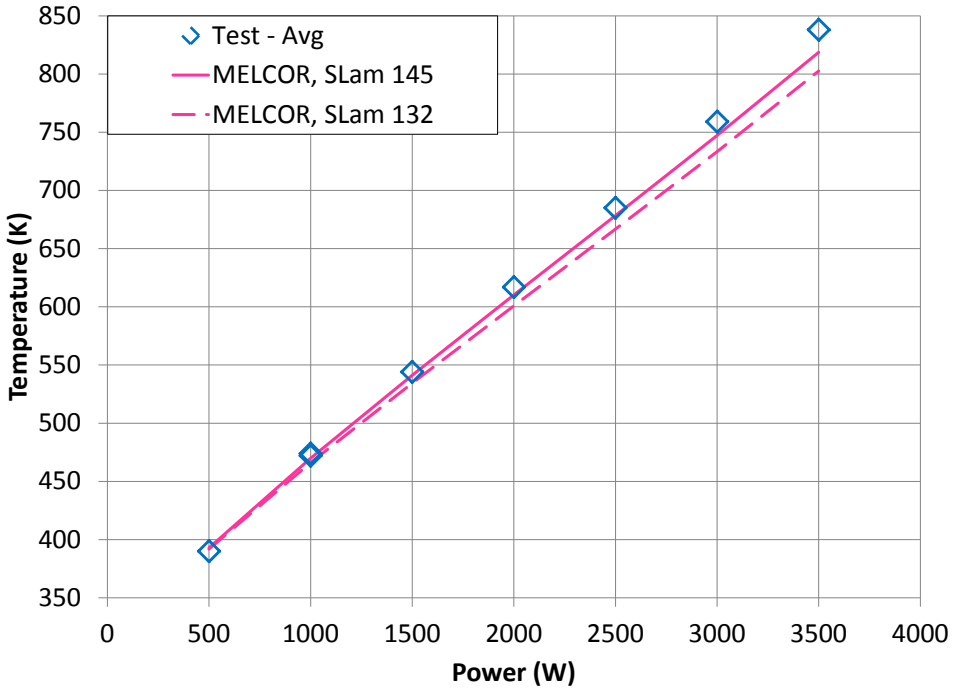

Figure 3.1 **Comparison of the average test (blue diamonds) and MELCOR (pink) temperatures during pre-ignition testing for Cell 1 at z = 3.150 m (124 in.) and t = 12 hrs**

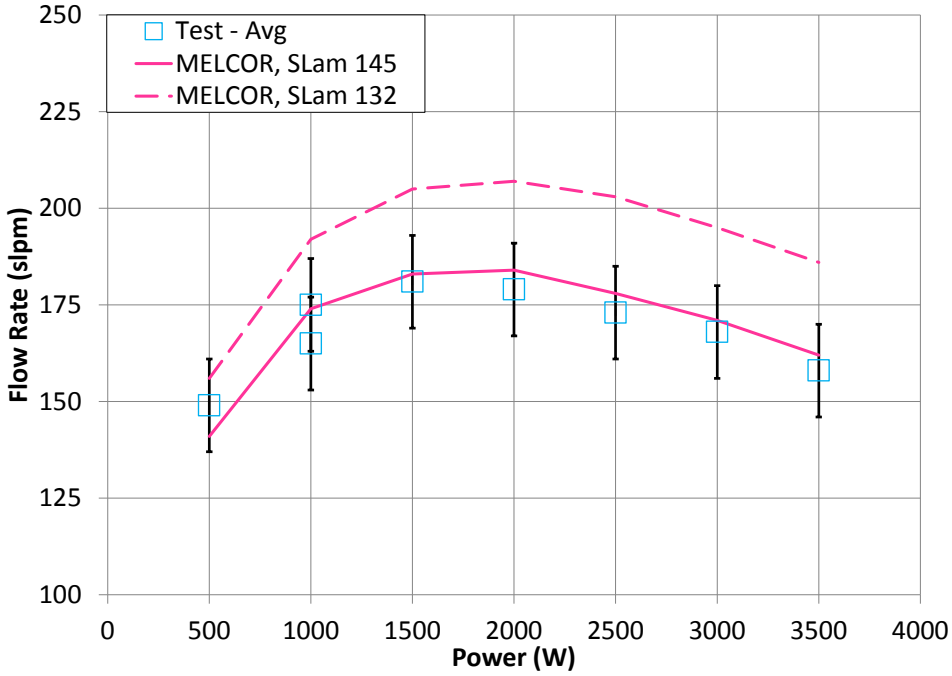

Figure 3.2 Comparison of the test (blue diamonds) and MELCOR (pink) flow rates during pre-ignition testing for Cell 1 at *t* = 12 hrs

While eight pre-ignition tests representing seven simulated decay powers were conducted for the Phase I – Cell 1 configuration, only powers of 1.0 and 3.5 kW are discussed in more detail in the following sections of the report. These tests were chosen because they bracket the experimental results. The 1.0 kW test was selected over the 0.5 kW test because the 1.0 kW test was conducted to 20 hours duration and represents the closest test result to steady state achieved in these studies.

3.1 Cell 1 – 1.0 kW Results

The peak, average test temperatures used to compare with MELCOR were calculated using the logic shown in Equation 3.1. The average data were determined primarily at the radial arrays with nine TCs, *z* = 4, 27, 52, 76, 100, 124, and 148 in. levels. In order to gain more axial information, the average values at the *z* = 124 and 148 in. levels were used in conjunction with the limited TC data at *z* = 130, 136, 142, and 154.875 in. levels to extrapolate average temperatures at these intermediate levels.

$$T_{avg}(t) = \max\left(\text{avg}\big|_{z=\text{const.}}\left(T(z,t)\right)\right) \quad \text{for } z = 4, 27, 52, 76, 100, 124, 130, 136, 142, 148 \text{ and } 154.875 \text{ in. levels} \tag{3.1}$$

Figure 3.3 shows the Cell 1 bundle temperatures at 1.0 kW simulated decay power for the peak, average test and MELCOR temperatures. The experiment and MELCOR are within 5 K (9°F) for the S_{LAM} of 145 and within 6 K (11°F) for the S_{LAM} of 132 case at *t* = 12 hrs. MELCOR under predicts the peak cladding temperature (PCT) by 13 K (23°F) for the S_{LAM} of 145 case and by 30 K (54°F) for the S_{LAM} of 132 case at *t* = 20 hrs.

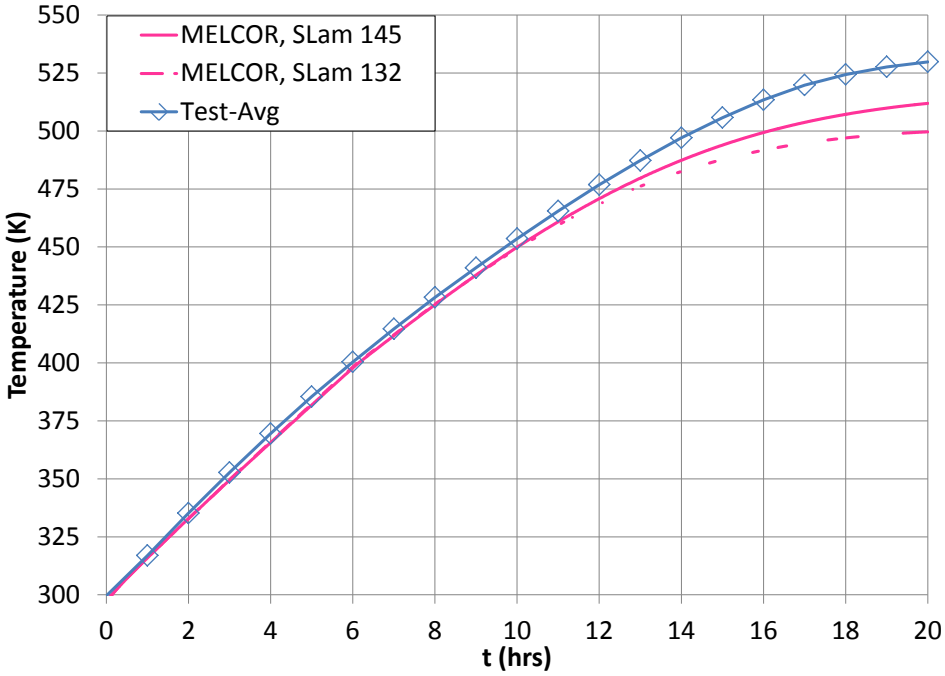

Figure 3.3 **Cell 1 bundle temperatures as a function of time at 1.0 kW simulated decay power for the average test temperature (blue diamonds) and MELCOR (pink)**

Figure 3.4 compares the transient induced flow rate of the Cell 1 configuration with an applied test power of 1.0 kW for the test and MELCOR results. The experimental enclosure was opened at approximately 13 hours elapsed test time to allow free access to both hot wire and laser Doppler anemometers. Traverses with an additional hot wire anemometer, which are not shown in this report, were conducted to measure the velocity profile inside the inlet pipe. In addition, alignment of the LDA and insertion of neutral density filters as required for operations were performed during this time period. MELCOR over predicts the observed flow data for a S_{LAM} of 132 and match favorably for a S_{LAM} of 145 case. For that reason, a S_{LAM} value of 145 is recommended for Cell 1.

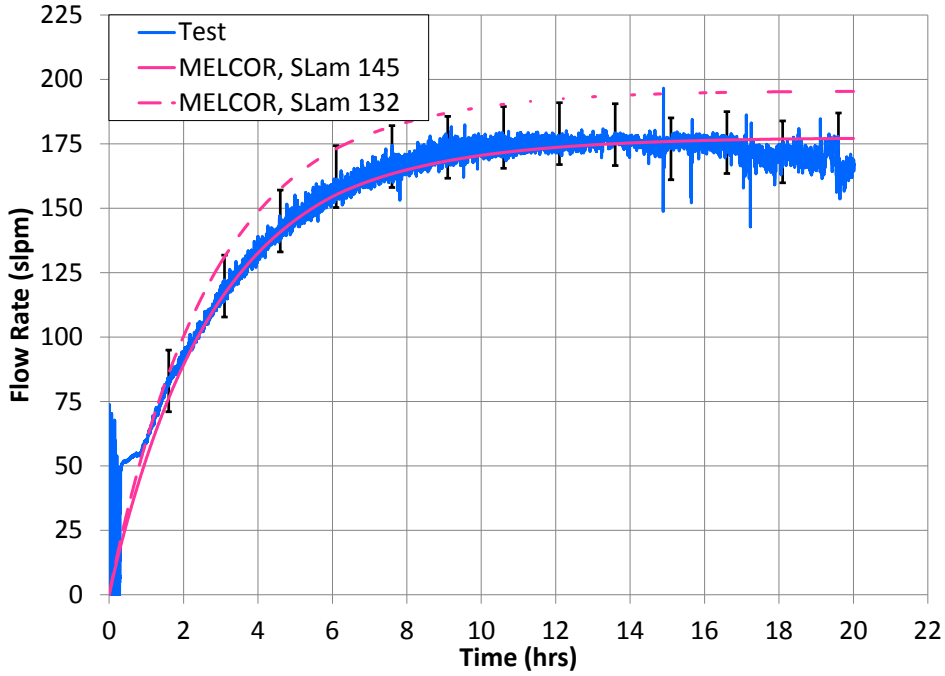

Figure 3.4 **Induced flow rate within the Cell 1 assembly at a simulated decay power of 1.0 kW for the test (blue solid) and MELCOR (pink)**

Figure 3.5 compares the Cell 1 maximum, average, and minimum test temperatures in the bundle as a function of axial height with MELCOR values at 12 hours elapsed time. MELCOR under predicts the average temperature in the top part of the assembly but over predicts the temperature in the lower part. The axial location of the MELCOR calculated PCT is accurate to within the discretization of the MELCOR model.

Similar to Figure 3.5, Figure 3.6 shows the test and MELCOR temperatures at t = 20 hours. Again, MELCOR over predicts the average temperature of the assembly in the lower part and under predicts the temperature in the upper part. The location of PCT is predicted to within less than one node in the MELCOR results for both cases. Figures 3.5 and 3.6 show that an S_{LAM} of 145 predicted the axial temperature profile more accurately than an S_{LAM} of 132. Figures 3.4 and 3.5 attest further that S_{LAM} of 145 for Cell 1 is more appropriate.

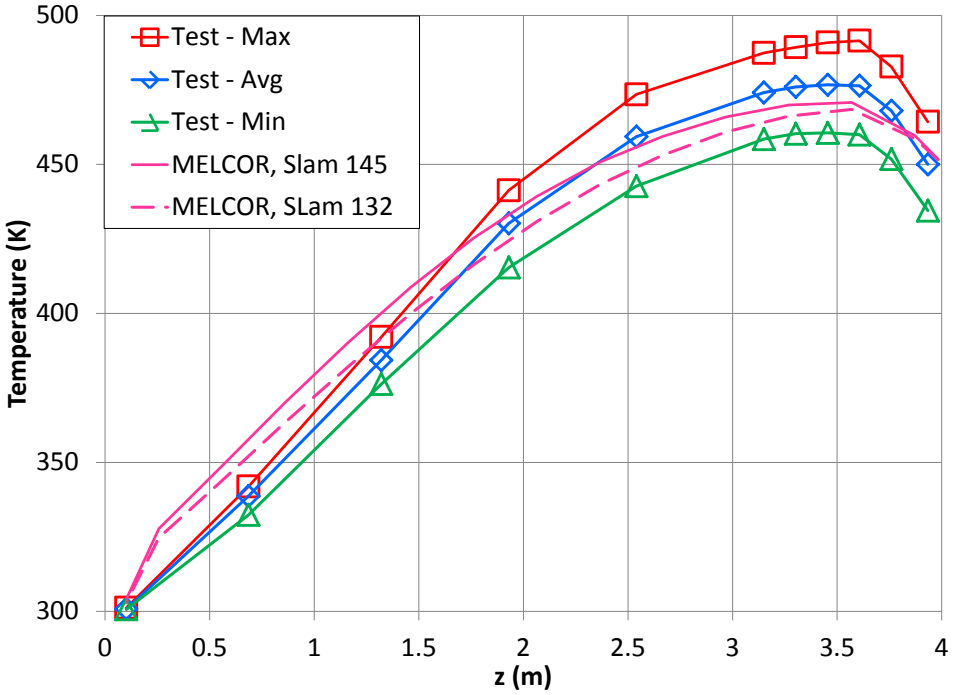

Figure 3.5 **Cell 1 bundle temperatures as a function of axial height in the assembly at 1.0 kW simulated decay power and 12 hours elapsed for the test maximum (red squares), average (blue diamonds), minimum (green triangles), and MELCOR temperatures (pink)**

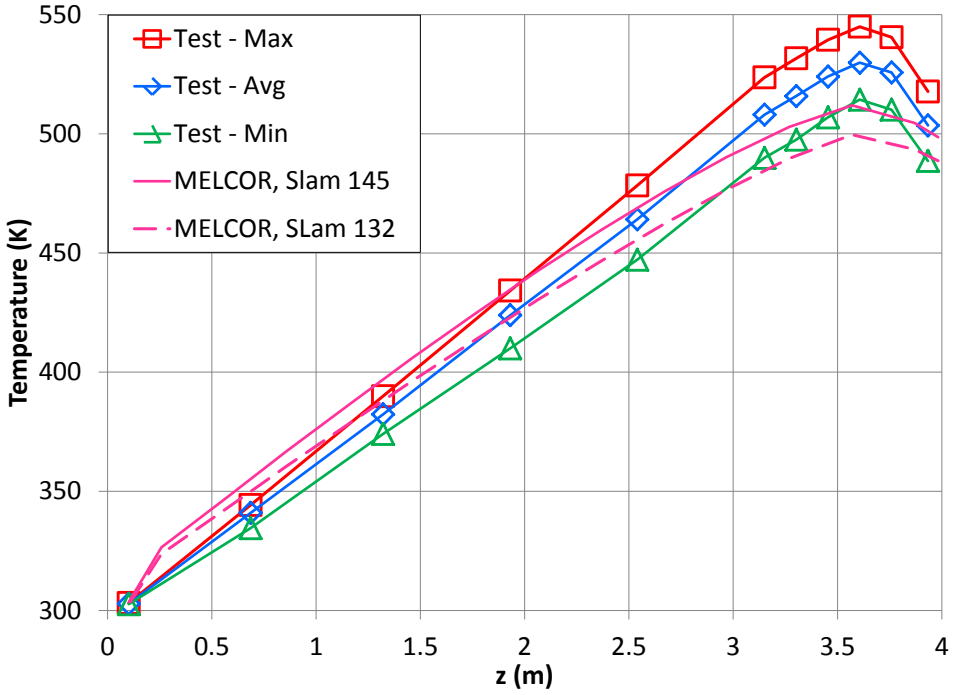

Figure 3.6 **Cell 1 bundle temperatures as a function of axial height in the assembly at 1.0 kW simulated decay power and 20 hours elapsed for the test maximum (red squares), average (blue diamonds), minimum (green triangles), and MELCOR temperatures (pink)**

3.2 Cell 1 – 3.5 kW Results

Figure 3.7 shows the Cell 1 maximum bundle temperatures at 3.5 kW heater power for the peak, average test and MELCOR temperatures. Experiment and MELCOR peak cladding temperatures agree to within 40 K (72°F) for S_{LAM} of 132 and within 30 K (54°F) for S_{LAM} of 145 case at all times.

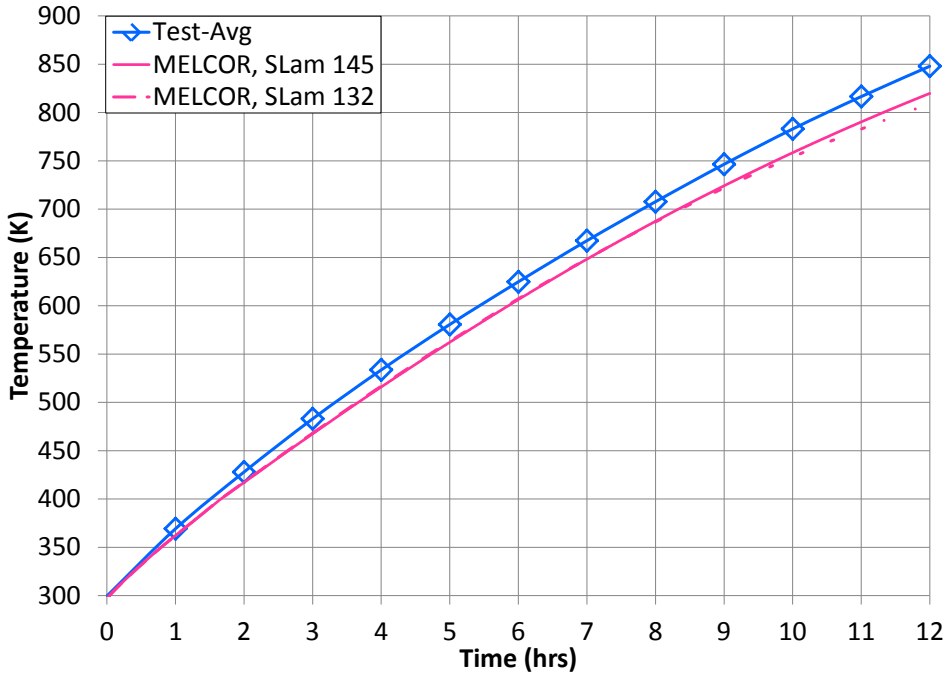

Figure 3.7 Cell 1 bundle temperatures as a function of time at 3.5 kW simulated decay power for the average test temperature (blue diamonds) and MELCOR (pink)

Figure 3.8 compares the transient, induced flow rate through the assembly in the Cell 1 configuration for the 3.5 kW test and MELCOR simulation. Disturbances to the flow rates between 2 and 3 hours were likely due to personnel entry into the vessel to diagnose lack of signal from auxiliary instrumentation. MELCOR over predicts the flow rate for a S_{LAM} value of 132 case match favorably the data for a S_{LAM} of 145 case for times greater than $t > 3$ hrs. For that reason a S_{LAM} value of 145 is also recommended for the 3.5 kW test of Cell 1.

Figure 3.9 compares the Cell 1 maximum, average and minimum test temperatures in the bundle as a function of axial height with MELCOR at 12 hours elapsed time. MELCOR under predicts the average temperature in the upper part of the assembly but over predicts the temperature in the lower part in both cases. The axial location of the MELCOR predicted PCT is accurate to within the nodalization of MELCOR.

The pre-ignition analysis for Cell 1 demonstrated that MELCOR accurately modeled the flow rate and peak cladding temperature using a Σk value of 30 and a S_{LAM} value of 145.

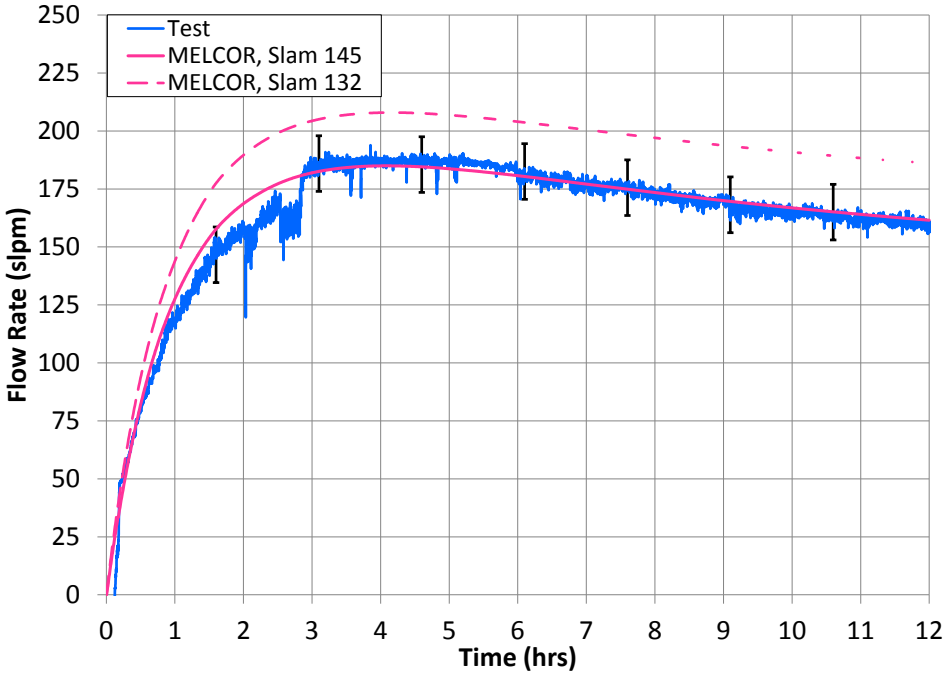

Figure 3.8 **Induced flow rate within the Cell 1 assembly at a simulated decay power of 3.5 kW for the test (blue solid) and MELCOR (pink)**

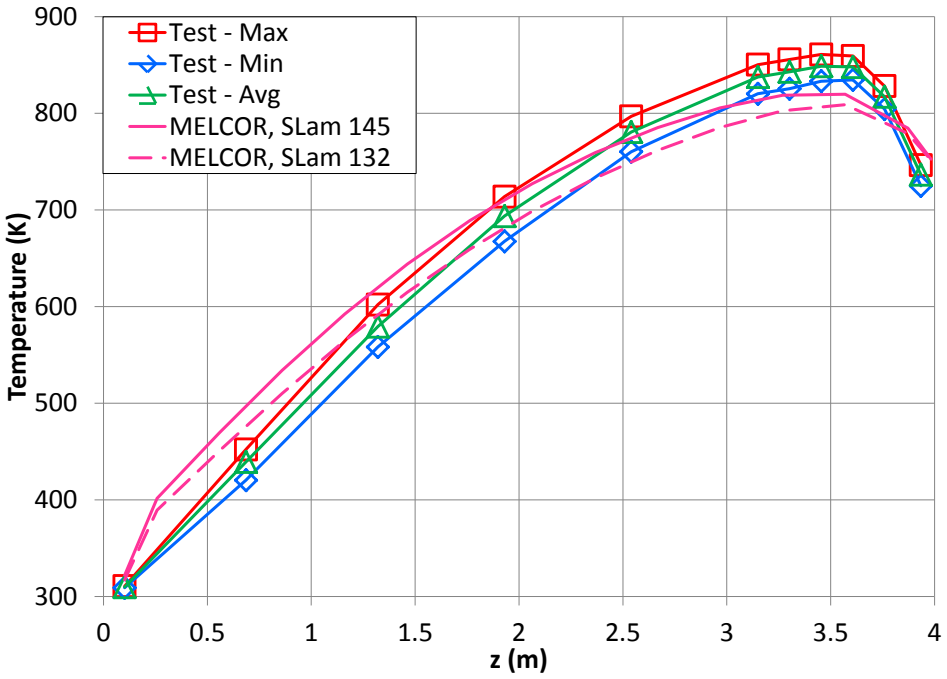

Figure 3.9 **Bundle temperatures as a function of axial height in the assembly at 3.5 kW simulated decay power and 12 hours elapsed for the maximum test temperature (red squares), average test temperature (blue diamonds), and MELCOR (pink)**

Figure 3.10 shows contours of temperature within the test apparatus at the midplane for the 3.5 kW test at t = 3, 6, 9, and 12 hours. The data represented in this plot reflect all available thermocouple data at the midplane of the apparatus with interpolation in between measurement locations. The midplane of the apparatus is defined at y = 0 m (see lower right assembly cross-section in Figure 2.8). A graphic of the fuel assembly and the surrounding insulation have been overlaid onto the plot. The insulation is denoted with diagonal hatch marks. Temperature data is not available for z > 3.934 m (154.875 in.) and z < 0.102 m (4 in.). The PCT was observed at z = 3.454 m (136 in.), which is also shown in Figure 3.7 The duration of this test was 12 hours.

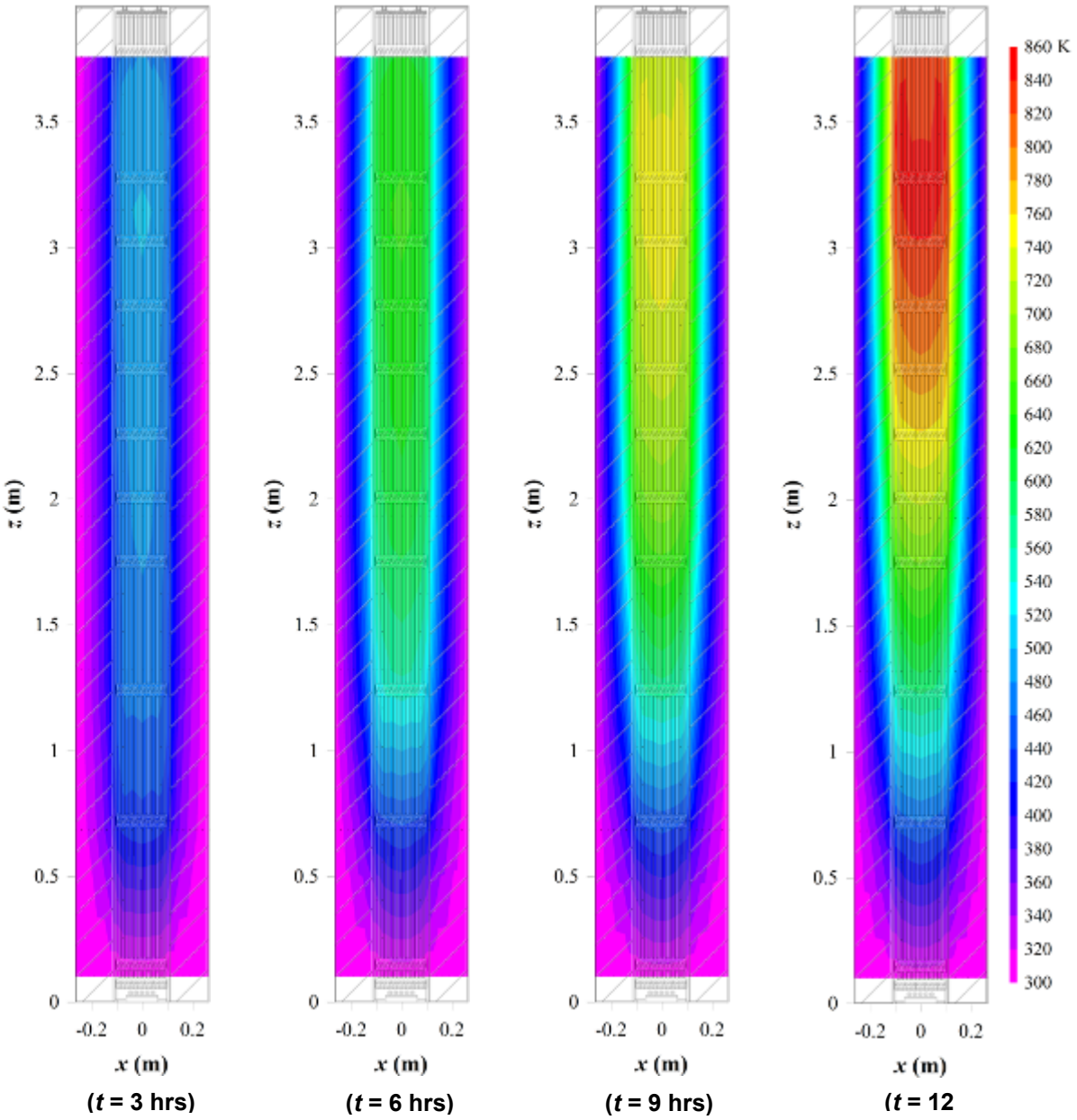

Figure 3.10 Contours of temperature within the assembly at the midplane for an input power of 3.5 kW

Figure 3.11 shows contours of temperature within the test apparatus at z = 3.150 m (124 in.) and t = 3, 6, 9, and 12 hours for the 3.5 kW test. Similar to Figure 3.10, this plot reflects all available thermocouple data at z = 3.150 m (124 in.) of the apparatus with interpolation in between measurement locations. A cross-sectional graphic of the fuel assembly and the surrounding insulation have been overlaid onto the plot. The insulation is denoted with diagonal hatch marks. The plot at t = 12 hours clearly demonstrates the transverse thermal gradient in the assembly. The temperature difference across the assembly is approximately 30 K (54°F) and is also documented in Table 3.1.

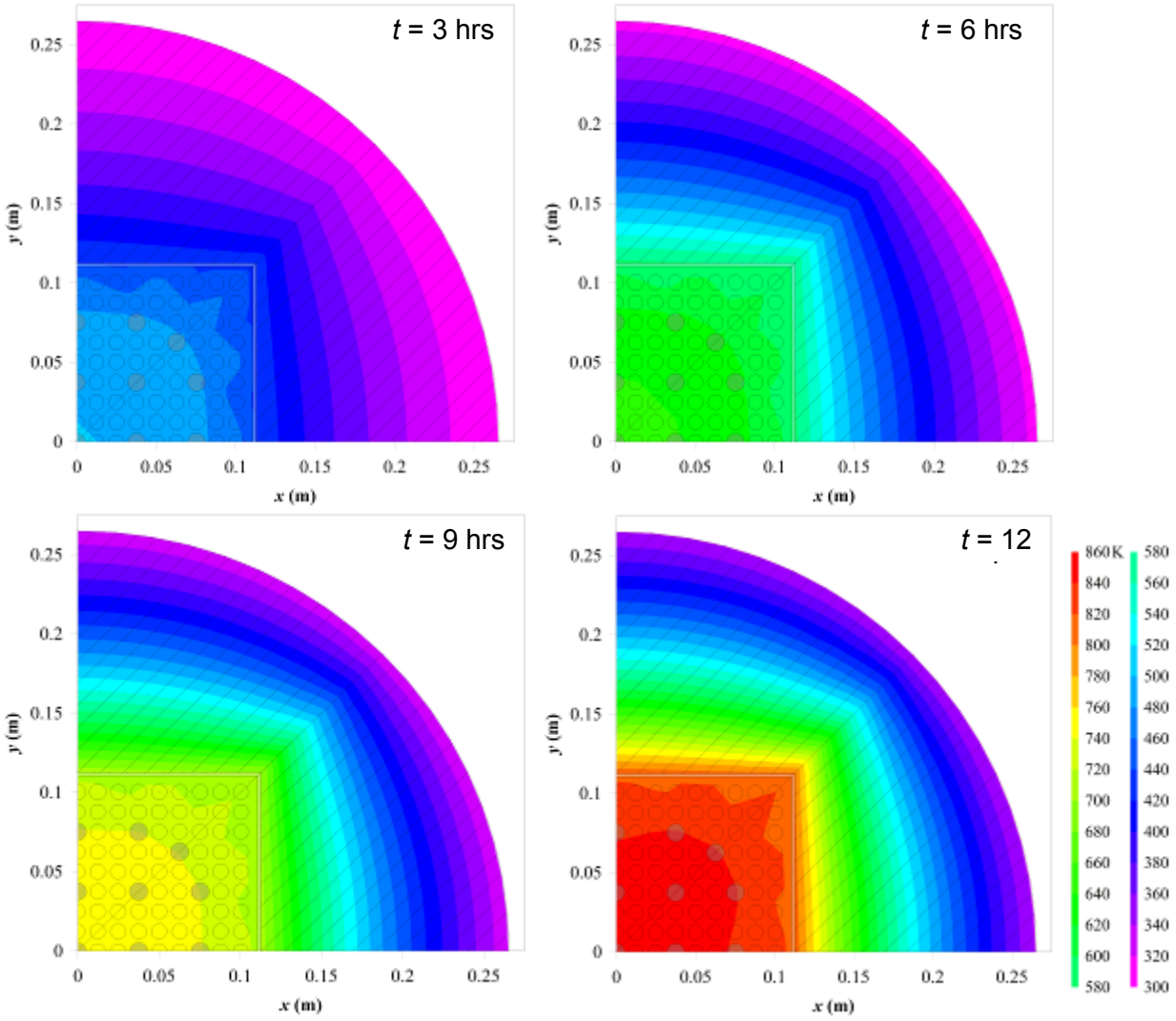

Figure 3.11 Contours of temperature within the assembly at z = 3.150 m (124 in.) level for an input power of 3.5 kW

4 CELL 2 PRE-IGNITION TESTING AND ANALYSIS

A summary of the pre-ignition testing results for Cell 2 are presented in Table 4.1. This table gives the average temperatures and flow rates at 3, 6, 9, and 12 hours for *z* = 3.150 m (124 in.). The minimum and maximum temperatures of the bundle at each time are also shown.

The 1.0 kW test was repeated to examine repeatability as shown in the second and third columns of test entries in Table 4.1. The temperatures during these repeatability tests were within 3 K (5.4°F) at all positions and times, slightly exceeding the experimental uncertainty of ±2.2 K (±4.0°F). The air flow rates were within 9 slpm for the two measurements, which is better than the experimental uncertainty of ±12 slpm.

Table 4.1 Summary of pre-ignition testing results for Cell 2 at *z* = 3.150 m (124 in.)

		True RMS Power (W)	500	1000	1000	1500	2000	2500	3000	3500
		Test Date	2/21/2011	12/07/2010	02/16/2011	01/26/2011	01/12/2011	01/11/2011	01/06/2011	01/05/2011
3 hrs		Flow Rate (slpm)	97	123	114	167	171	186	193	204
	Bundle	Min. Temp. (K)	322	345	347	371	386	415	428	457
		Max. Temp. (K)	330	361	361	393	413	449	467	504
		Avg. Temp. (K)	327	354	355	383	402	434	450	482
	Pool Cell	Avg. Temp. (K)	317	337	340	359	372	400	412	441
	Rad. Barrier	Avg. Temp. (K)	298	299	300	299	304	303	304	301
	Ambient	Avg. Temp. (K)	297	298	299	298	302	300	301	299
6 hrs		Flow Rate (slpm)	128	182	175	197	209	209	215	211
	Bundle	Min. Temp. (K)	344	387	390	432	468	514	549	594
		Max. Temp. (K)	356	411	412	463	504	555	591	640
		Avg. Temp. (K)	351	400	401	448	486	535	571	619
	Pool Cell	Avg. Temp. (K)	339	380	382	423	457	504	537	585
	Rad. Barrier	Avg. Temp. (K)	299	298	301	302	306	310	305	308
	Ambient	Avg. Temp. (K)	298	295	299	298	300	302	299	298
9 hrs		Flow Rate (slpm)	146	189	188	208	213	206	205	197
	Bundle	Min. Temp. (K)	364	424	427	484	537	598	647	706
		Max. Temp. (K)	378	450	452	517	573	637	686	748
		Avg. Temp. (K)	372	437	440	501	556	618	668	729
	Pool Cell	Avg. Temp. (K)	359	417	420	477	529	590	639	700
	Rad. Barrier	Avg. Temp. (K)	301	301	303	306	310	317	316	320
	Ambient	Avg. Temp. (K)	298	295	297	298	299	301	299	298
12 hrs		Flow Rate (slpm)	154	193	197	205	214	200	201	194
	Bundle	Min. Temp. (K)	382	451	454	519	583	652	712	781
		Max. Temp. (K)	398	482	484	557	625	695	755	823
		Avg. Temp. (K)	390	467	469	538	604	675	734	804
	Pool Cell	Avg. Temp. (K)	376	446	449	513	578	648	708	778
	Rad. Barrier	Avg. Temp. (K)	302	303	306	309	314	323	325	330
	Ambient	Avg. Temp. (K)	297	296	298	297	298	302	299	298

On Table 2.1, the value for S_{LAM} is 146 for Cell 2. However, based on fundamentals of fluid mechanics, this value should be lower than the value for Cell 1 because the flow area of Cell 2 is larger. For that reason, the experimental data of Cell 2 was compared with two MELCOR models using the values of 146 for S_{LAM} as shown in Table 2.1 and a S_{LAM} of 133 including the uncertainty of -13. On the other hand, on Table 2.1, the value of Σk is 25 for Cell 2. Based on fluid mechanics fundamentals this value should be higher because the flow experiences a larger expansion after spacer grids. After comparing MELCOR results using the values of 25 and 30 for Σk (Figures 4.1 and 4.2), no significant differences were observed and for that reason a value of 30 for Σk was used for Cell 2 MELCOR analysis. As observed in Figure 4.1, the test and MELCOR model results agree within 16 K (29°F) for a S_{LAM} of 133 and within 7 K (13°F) for

a S_{LAM} of 146 at all powers. Similarly, Figure 4.2 shows the comparison of the airflow rates for the pre-ignition tests and MELCOR at t = 12 hrs. The model agrees with the measured flow rate within 20 slpm for a S_{LAM} of 133 and within 10 slpm for a S_{LAM} of 146 for all powers.

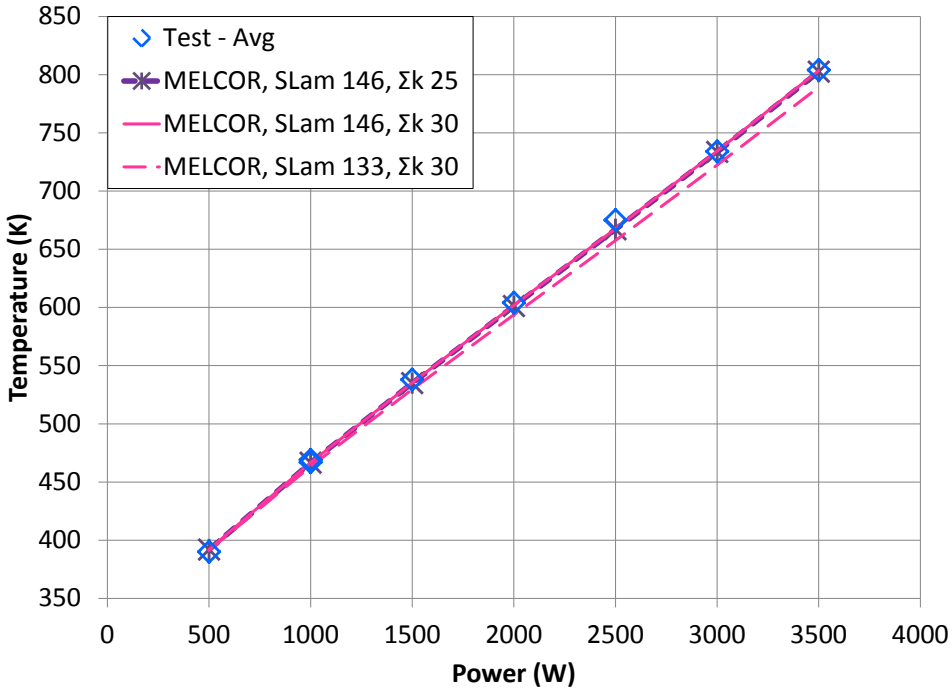

Figure 4.1 **Comparison of the average test (blue diamonds) and MELCOR (pink) temperatures during pre-ignition testing for Cell 2 at z = 3.150 m (124 in.) and t = 12 hrs**

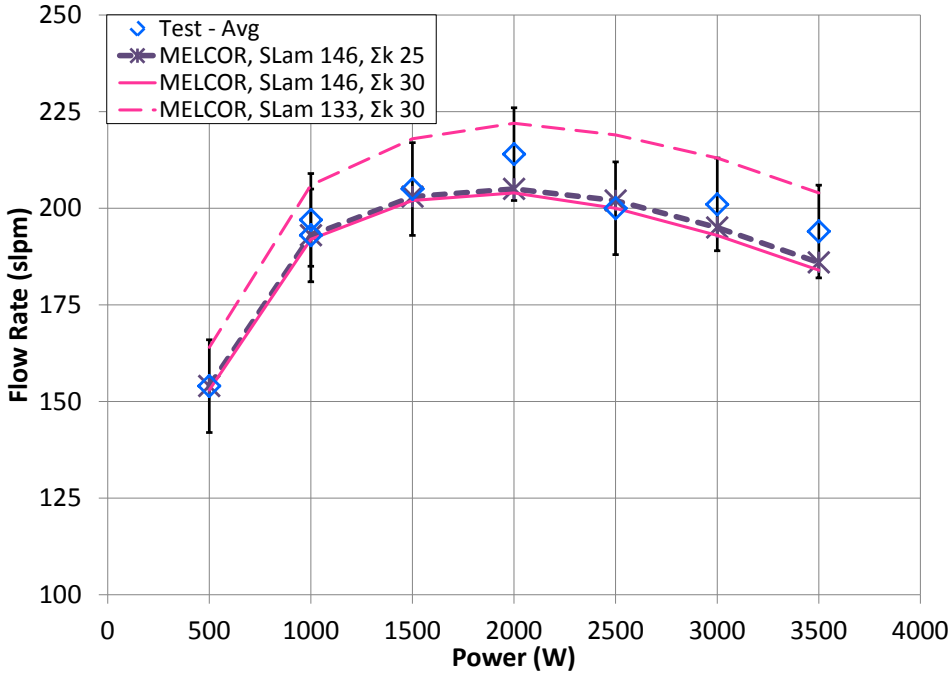

Figure 4.2 Comparison of the test (blue diamonds) and MELCOR (pink) flow rates during pre-ignition testing for Cell 2 at *t* = 12 hrs

While eight pre-ignition tests representing seven simulated decay powers were conducted for the Phase I – Cell 2 configuration, only powers of 1.0 and 3.5 kW will be discussed in more detail in the following sections of the report. These tests were chosen because they bracket the experimental results. The 1.0 kW test was selected over the 0.5 kW test because the 1.0 kW test was conducted for 20 hours and represented the closest test result similar to a steady state condition achieved in these studies.

4.1 Cell 2 – 1.0 kW Results

Figure 4.3 shows the Cell 2 maximum bundle temperatures at 1.0 kW simulated decay power for the average test and MELCOR temperatures. The average experiment and MELCOR peak cladding temperatures agree to within 20 K (36°F) for a S_{LAM} of 133 and within 10 K (18°F) for a S_{LAM} of 146.

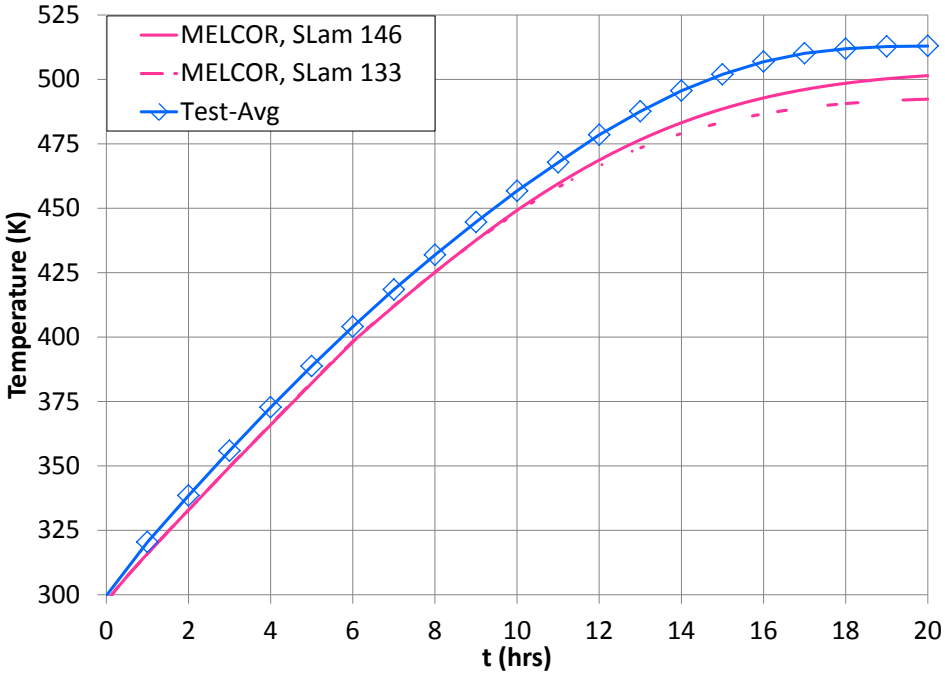

Figure 4.3 **Cell 2 bundle temperatures as a function of time at 1.0 kW simulated decay power for the average test temperature (blue diamonds) and MELCOR (pink)**

Figure 4.4 compares the Cell 2 maximum, average, and minimum 1.0 kW test temperatures in the bundle as a function of axial height with the MELCOR values at 12 hours. The test values are those defined in the maximum operator on the right hand side of Equation 3.1 for t = 12 hours. MELCOR under predicted the average temperature in the top part of the assembly but over predicted the temperature in the lower part. The axial location of the MELCOR predicted PCT is accurate to within the discretization of the MELCOR model. Similar to Figure 4.4, Figure 4.5 shows the test and MELCOR temperatures at t = 20 hours. Again, MELCOR over predicts the average temperature of the assembly in the lower part and under predicts the temperature in the upper part. The location of PCT is predicted to within less than one node in the MELCOR results for both cases. Figures 4.4 and 4.5 show that an S_{LAM} of 146 predicted the axial temperature profile more accurately than an S_{LAM} of 133.

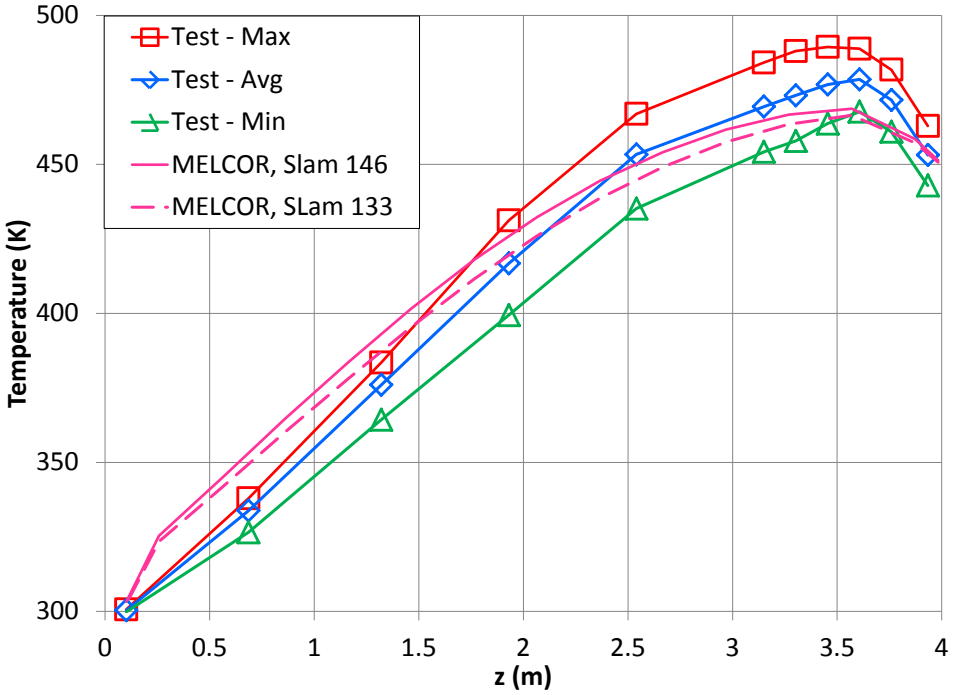

Figure 4.4 **Cell 2 bundle temperatures as a function of axial height in the assembly at 1.0 kW simulated decay power and 12 hours elapsed for the maximum test (red squares), average test (blue diamonds), minimum test (green triangles) and MELCOR (pink)**

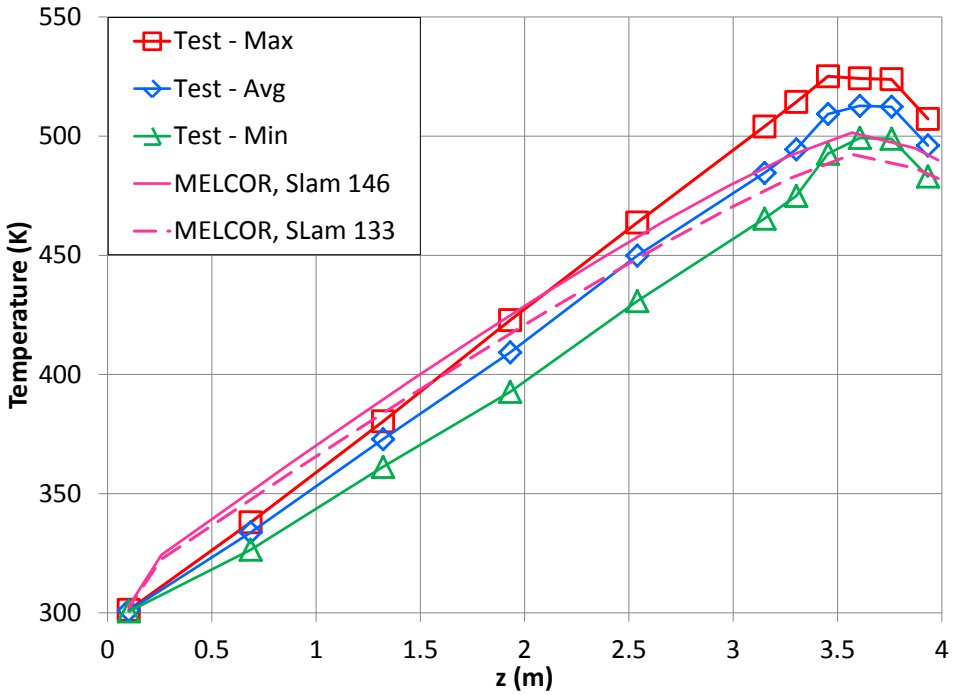

Figure 4.5 **Cell 2 bundle temperatures as a function of axial height in the assembly at 1.0 kW simulated decay power and 20 hours elapsed for the maximum test (red squares), average test (blue diamonds), minimum test (green triangles) and MELCOR (pink)**

Figure 4.6 compares the transient induced flow rate of the Cell 2 configuration with a power of 1.0 kW for the test and MELCOR results. The experimental enclosure was opened at approximately 13 hours elapsed test time to allow free access to the laser Doppler anemometer. The sharp increase and subsequent decrease at 13 hours was due to the experimental enclosure equilibrating to the building temperature. The data and simulation agree within the experimental uncertainty of 12 slpm at all times in both cases for the MELCOR simulation using S_{LAM} of 146, with the exception of the disturbance at t = 13 hours as previously described. MELCOR predictions using S_{LAM} of 133 over predicted the mass flow rare as shown in Figure 4.6.

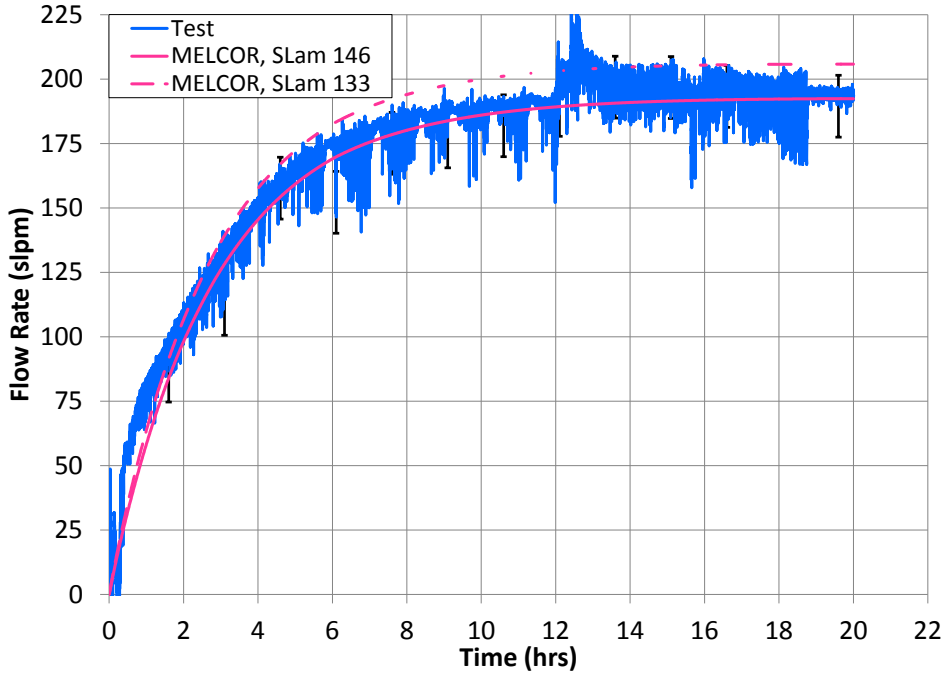

Figure 4.6 **Induced flow rate within the Cell 2 assembly at a simulated decay power of 1.0 kW for the test (blue solid) and MELCOR (pink)**

4.2 Cell 2 – 3.5 kW Results

Figure 4.7 shows the Cell 2 bundle temperatures at 3.5 kW heater power for the average test and MELCOR temperatures. Experiment and MELCOR peak cladding temperatures agree to within 28 K (50°F) for an S_{LAM} of 133 and within 18 K (32°F) for an S_{LAM} of 146 at all times.

Figure 4.8 compares the Cell 2 maximum, average, and minimum 3.5 kW test temperatures in the bundle as a function of axial height with two MELCOR simulations at 12 hours elapsed time. The test values are those defined in the maximum operator on the right hand side of Equation 3.1 for t = 12 hours. Again, MELCOR simulations over predicted the average temperature in the lower part of the bundle and under predicted the temperature in the upper part of the bundle for both cases. The axial location of the MELCOR PCT is accurate to within the nodalization of the model.

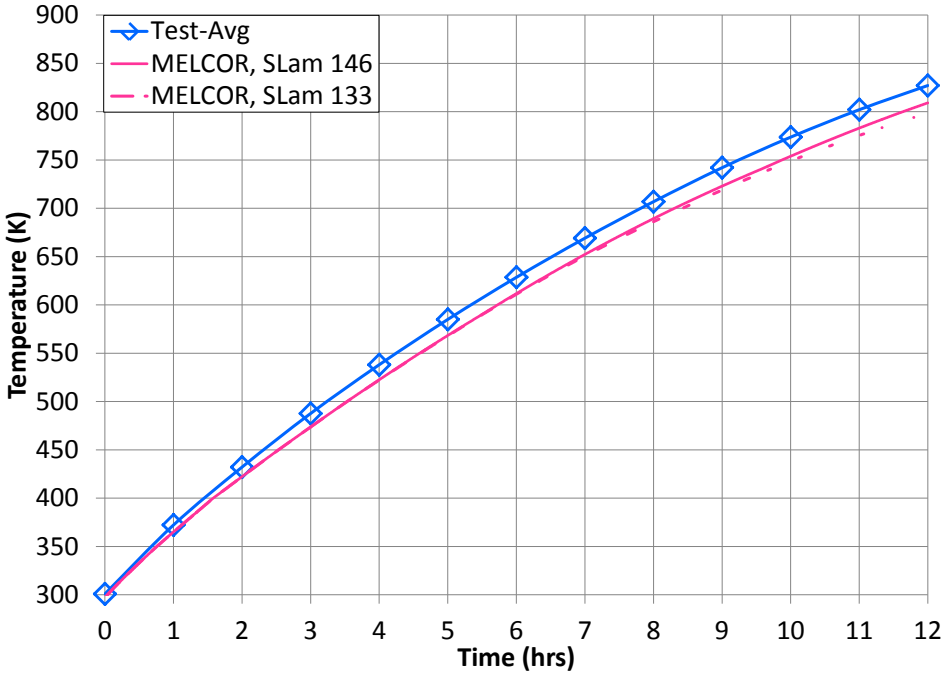

Figure 4.7 **Cell 2 bundle temperatures as a function of time at 3.5 kW simulated decay power for the average test (blue diamonds) and MELCOR (pink)**

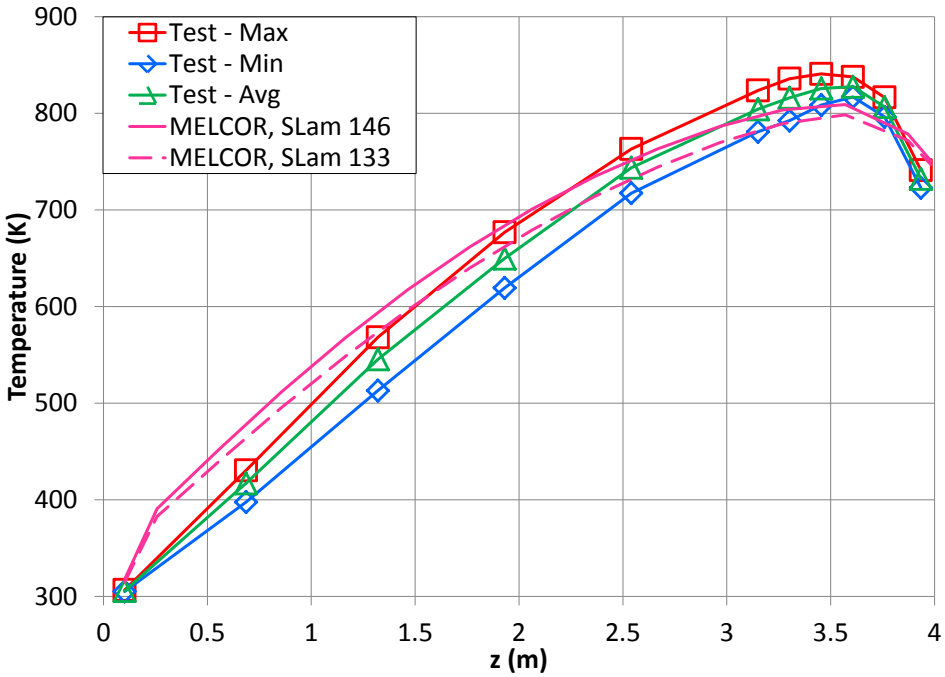

Figure 4.8 **Bundle temperatures as a function of axial height in the assembly at 3.5 kW simulated decay power and 12 hours elapsed for the maximum test (red squares), average test (blue diamonds), minimum test (green triangles), and MELCOR (pink)**

Figure 4.9 compares the transient induced flow rate through the assembly in the Cell 2 configuration for the 3.5 kW test and MELCOR simulations. MELCOR predicted the mass flow rate favorably within the experimental error of 12 slpm for S_{LAM} values between 133 and 145.

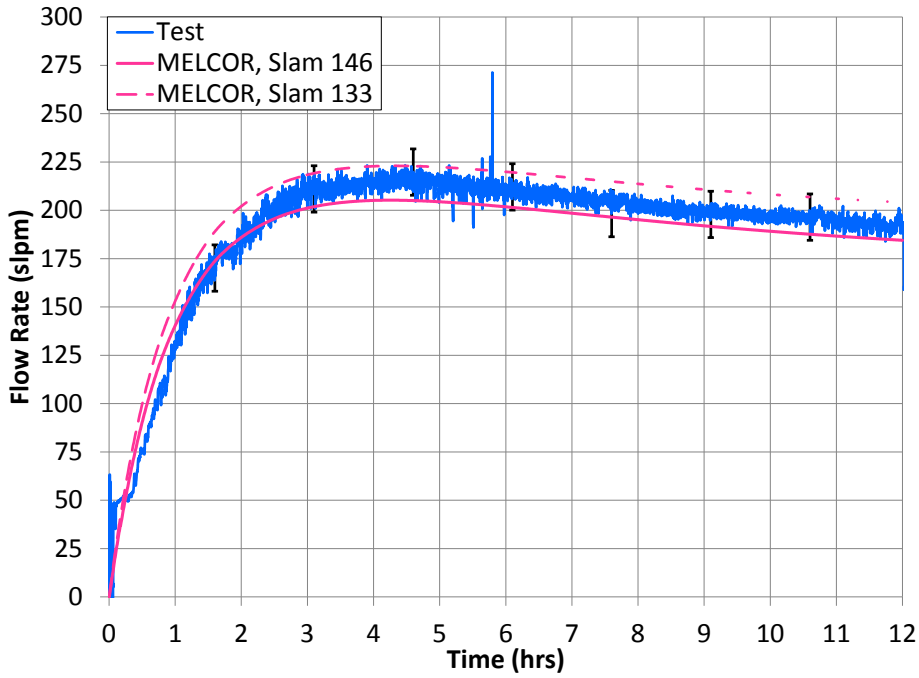

Figure 4.9 **Induced flow rate within the Cell 2 assembly at a simulated decay power of 3.5 kW for the test (blue solid) and MELCOR (pink)**

4.3 Internal Assembly Mass Flow

The behavior of the internal flow in the assembly was explored with a laser Doppler anemometer (LDA) and with computational fluid dynamics (CFD). These measurements and simulations were for both forced (unheated) and natural circulation (heated) cases. In order to account for differences in density for the heated cases, the results in this section are presented as mass flux profiles and mass flow fractions.

A series of average velocity profiles were collected with the LDA along the x-axis in the assembly at z = 0.442 m (1.45 ft) and y = -0.0189 m (-0.74 in.) (See Figure 2.6) for both forced and naturally induced flows. These profiles were measured between the inside of the optical window to slightly beyond the assembly center. The forced flow data were collected to establish a baseline with which to compare the free convection generated velocity profiles. Three forced flows of 150, 186, and 225 slpm were chosen because they bracketed the expected flow rates for the heated tests. Velocity profiles were measured for heated tests at applied powers of 0.5 and 1 kW. These naturally induced flow profiles were collected after the assembly had been under power for 12 hours. The change in the measured inlet flow rate between 12 and 20 hours was less than 3 percent of the flow rate at 12 hours for both powered tests. The local air density in the assembly was estimated from the interpolated cladding and pool cell temperatures along the x-axis at z = 0.442 m (1.45 ft) and y = -0.0189 m (-0.74 in.).

The three-dimensional CFD simulations were performed on a 1/8th wedge of the PWR fuel assembly, taking advantage of symmetry conditions in the cross-sectional geometry. ANSYS Fluent version 14.0.0 was used for all calculations. The spacers and nozzles were explicitly modeled as flow restrictions with simplified geometric representations, i.e. sheet metal construction without turning vanes. The problem solution was obtained using a steady-state, laminar solver. The inlet was defined with a uniform velocity condition for forced flow cases and with a pressure boundary condition for naturally induced flow cases. The outlet was defined with a pressure boundary condition for all cases. Thermal radiation was modeled by the discrete ordinates method. The momentum, energy, and discrete ordinates equations were solved with 2nd order up-wind discretization scheme. The continuity equation was linked to the momentum equation through the Pressure Staggering Option.

4.3.1 Forced Flow Calibrations

Figure 4.10 shows the three normalized mass flux profiles collected during the forced flow baselines. The force flow calibration used an unheated assembly. This plot also shows two profiles produced from computational fluid dynamics (CFD) simulations. The local mass flux, density multiplied by velocity, is normalized by the uniform, average bundle velocity and inlet air density. The inlet air density for both the LDA and CFD normalizations is defined as ρ_o = 0.986 kg/m^3 (0.062 lb/ft^3) at T_o = 297 K (75°F) and P_o = 84 kPa (12.2 psi). The *x*-dimension is normalized by the fuel rod pitch, *P*. Again, all profiles were collected between the rod banks identified in Figure 2.6 at *z* = 0.442 m (17.4 in.). The three normalized profiles exhibit nearly identical behavior as might be expected. Significant variations occur at locations where measurements were more difficult due to the presence of a solid surface such as a fuel pin or the optical window. Alignment of the LDA apparatus was performed to center the measurement volume between the rod banks depicted in Figure 2.6. Unlike the CFD profiles, the amplitudes of the measured maxima and minima are not equal due to random orientations of the heater rods, which had a slight curvature in their shape imparted from the manufacturing process. The rods at *x*/*P* = 2 and 6 were particularly distorted, nearly preventing penetration to the center of the assembly. However, the integrated line averages of all the LDA (dashed black lines) and CFD (dashed gray lines) profiles were within about 1percent of each other in both the bundle (0 ≤ *x*/*P* ≤ 8) and in the annulus (*x*/*P* > 8). These integrated line averages of forced flows are repeated in subsequent graphs of heated flux profiles for reference.

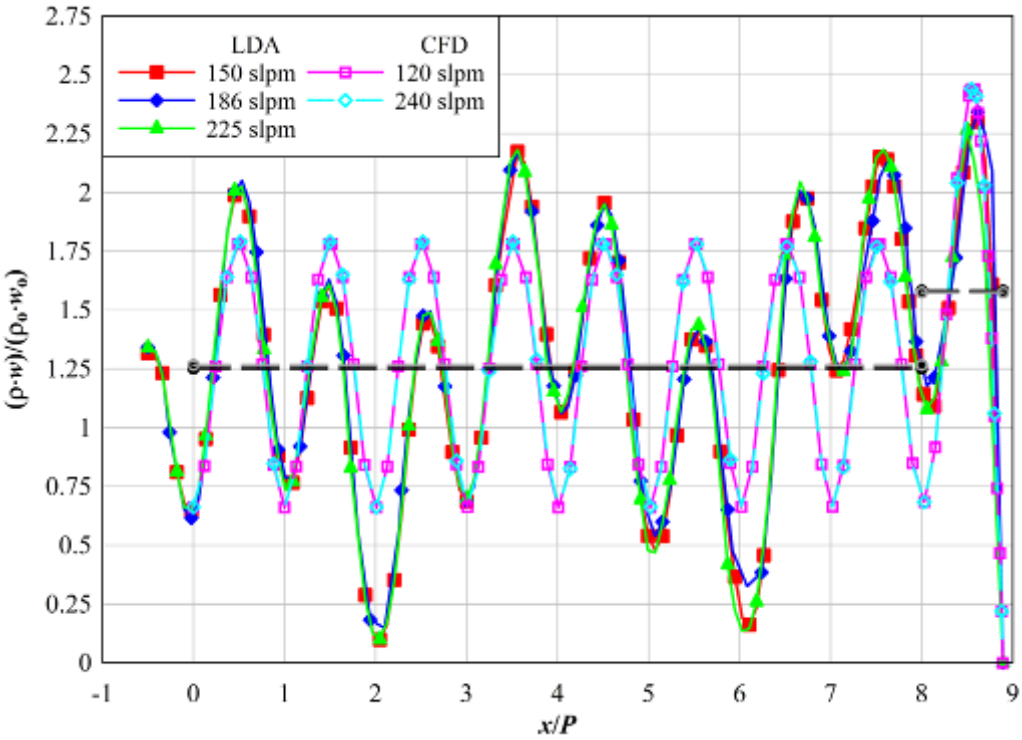

Figure 4.10 Normalized mass flux profiles within the fuel assembly for measured flows of 150 (red squares), 186 (blue diamonds), and 225 slpm (green triangles) and for simulated flows of 120 (open pink squares) and 240 slpm (open light-blue diamonds)

4.3.2 Naturally Induced Velocity Profiles

Figure 4.11 gives the measured and simulated normalized mass flux profiles of the naturally induced flow for an assembly power of 0.5 kW. Again, the long dashed lines represent the integral averages of each profile from $0 \le x/P \le 8$ for the bundle and $x/P > 8$ for the annulus. The black and gray dashed lines represent the integrated line average of the forced flow cases for the LDA and CFD, respectively. The integral averages indicate that the bundle flow increases and the annular flow decreases for the naturally induced flows compared to the forced flow values. The LDA and CFD 0.5 kW profiles show decreases in the annulus of 10 and 5 percent of the integral line averages compared to the forced cases, respectively. Conversely, the bundle mass fluxes increased by 3 and 8 percent over the forced integral average for the LDA and CFD results, respectively.

Figure 4.12 gives the normalized mass flux profiles at an assembly power of 1 kW for naturally induced flow as a function of x/P at 12 hours. The forced flow integral averages are repeated in the plot as the black dashed (LDA) and gray dashed (CFD) lines. The integrated line averages of the heated mass fluxes in the bundle are 5 and 10 percent higher than the forced cases for the LDA and CFD results, respectively. Comparison of the heated and forced annulus line averages reveals decreases of 11 and 8 percent for the LDA and CFD results, respectively.

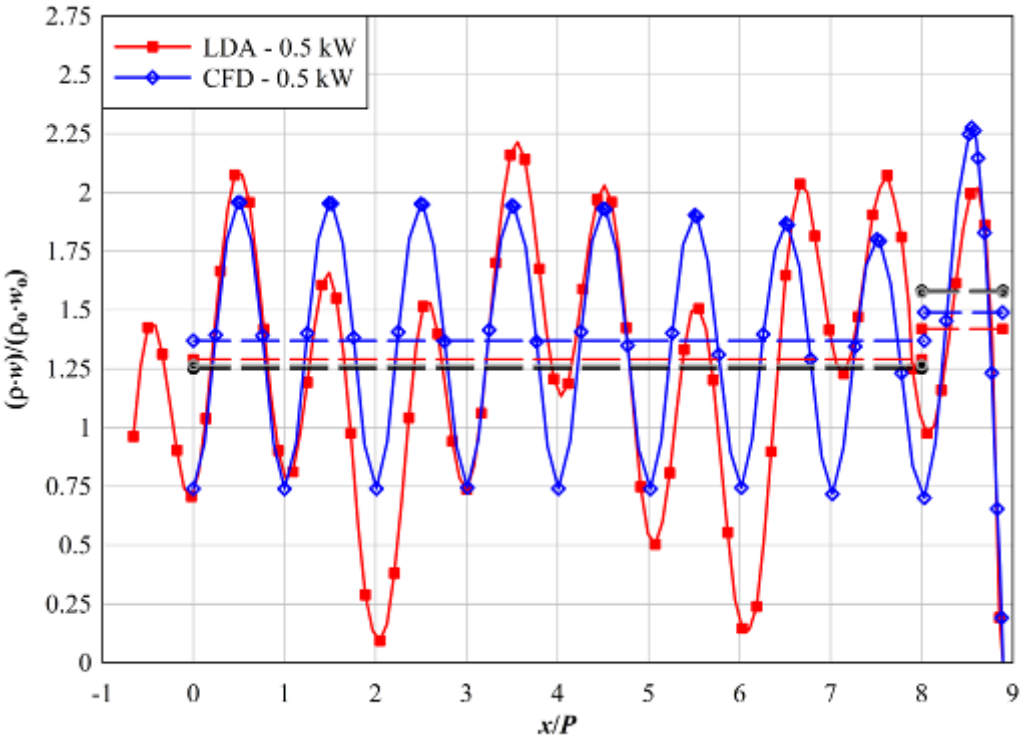

Figure 4.11 **Normalized mass flux profiles within the fuel assembly of the naturally induced flows at 0.5 kW for measured (red squares) and simulated (open blue diamonds)**

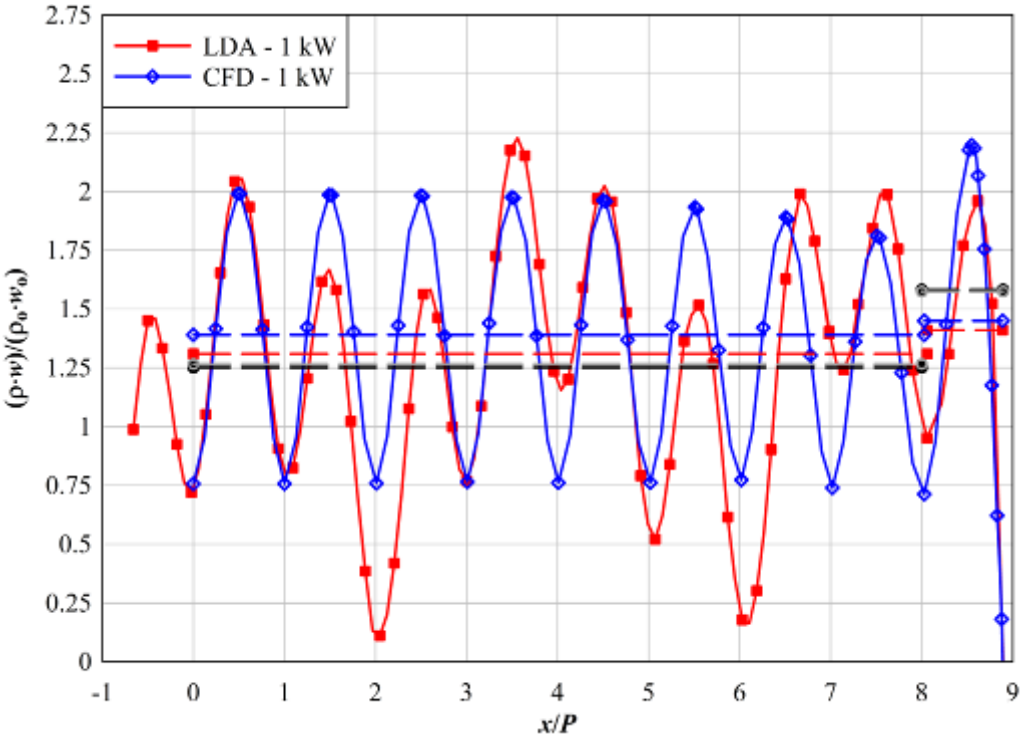

Figure 4.12 **Normalized mass flux profiles within the fuel assembly of the naturally induced flows at 1 kW for measured (red squares) and simulated (open blue diamonds)**

By multiplying the average, normalized mass fluxes in the bundle and annulus by their respective areas, the mass flow fraction may be estimated. This technique will knowingly overestimate the flows especially in the bundle because the mass fluxes are estimated along lines of maximum value, whereas the flow field is two-dimensional. However, this line-based estimation is the only method available for the LDA data. The CFD data provides both this line average value and the actual mass flows in the bundle and annulus. Figure 4.13 shows the mass flow fractions for the LDA and CFD line average technique as a function of power. The area-based, or actual, mass flow fractions from the CFD results are also provided. As expected, the line-based mass flow fractions in the bundle overestimate the area-based value by up to 0.033. However, the line average mass flow fractions for the LDA and CFD results agree to within 0.007. All the data suggest that the mass flow fraction in the bundle is increasing with assembly power at this axial location. The CFD results are explored next to determine the evolution of the mass flow fractions in the bundle and annulus as the flow passes up the assembly.

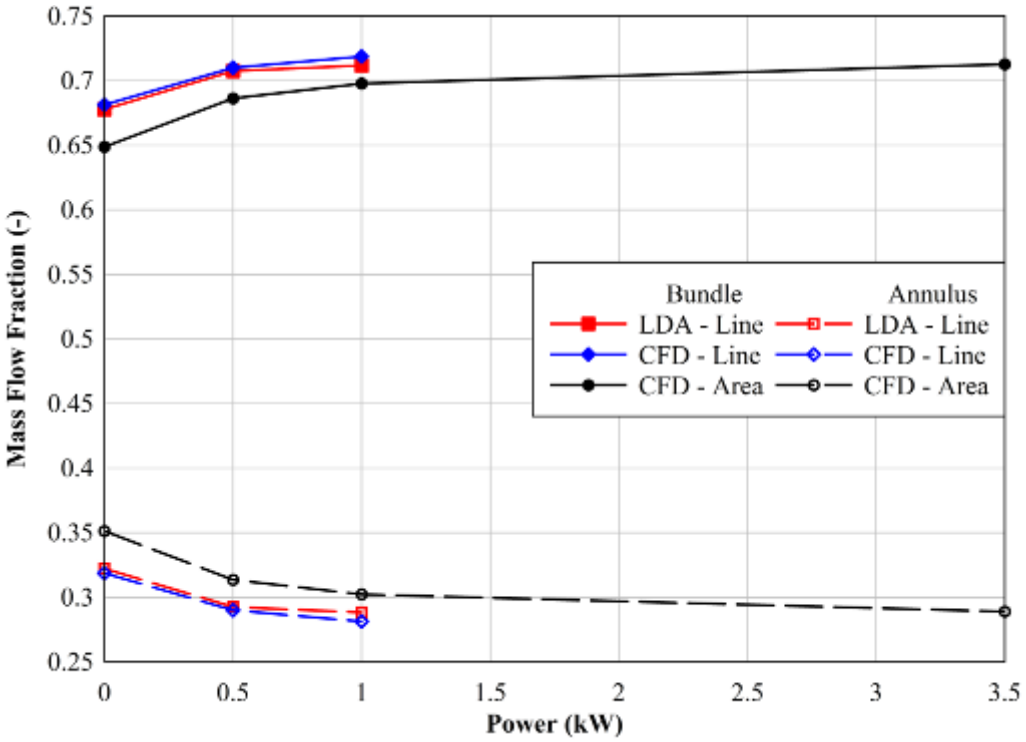

Figure 4.13 **Bundle and annulus mass flow fraction at *z* = 0.442 m (17.4 in.) within the assembly for the bundle from the LDA line average (red squares), CFD line average (blue diamonds), and CFD area average (black circles) and for the annulus from the LDA line average (open red squares), CFD line average (open blue diamonds), and CFD area average (open black circles)**

The area-average mass flow fractions in the bundle and annulus from the CFD simulations are next plotted as a function of the *z*-coordinate in Figure 4.14. The limited number of points shown in the graph are at the computational inlet and exit as well as two mid-bundle locations. The effects of the flow area contraction at spacers are not depicted in the graph but were captured in the CFD results. For reference, the bundle and annulus flow areas represent about 75 and 25 percent of the total flow area in a bundle section, respectively. As expected, the forced mass flows partition according to the flow area ratios at the inlet where a uniform velocity condition is imposed. The forced flow appears to asymptote to approximately 0.63 of the flow in

the bundle and 0.37 in the annulus. The heated cases show an inlet bundle mass flow fraction of 0.64, which then quickly increases as the flow moves up the bundle to z = 0.442 m (1.45 ft). The amount of this increase appears to be dependent on the assembly power. The bundle mass flow fraction then decreases as the flow moves further up the assembly, approaching the forced flow value. Finally, the bundle flow fraction at the exit of all the CFD simulations shows a decrease to approximately 0.6 due to the close proximity of a spacer at z = 3.89 m (12.8 ft). The annular mass flow fraction mirrors the behavior in the bundle.

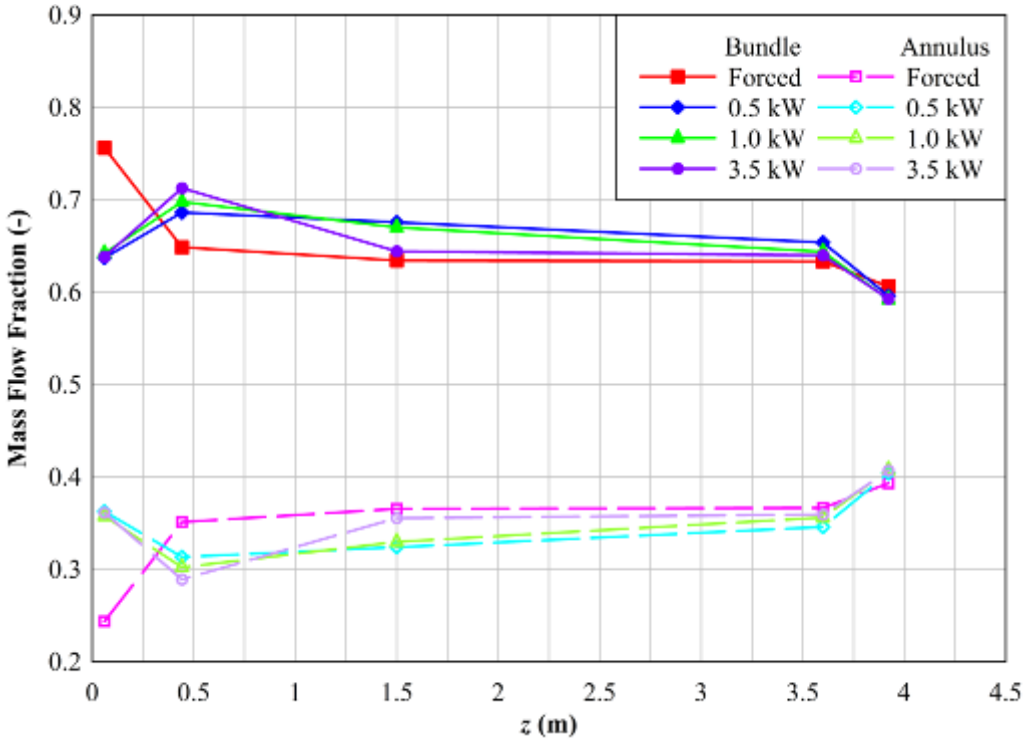

Figure 4.14 **Bundle and annulus mass flow fraction within the assembly for the bundle forced flow (red squares), 0.5 kW (blue diamonds), 1 kW (green triangles), and 3.5 kW (purple circles) and for the annulus forced flow (open pink squares), 0.5 kW (open light-blue diamonds), 1 kW (open light-green triangles), and 3.5 kW (open light-purple circles)**

5 CELL 2 IGNITION TESTING AND ANALYSIS

Phase I of the Spent Fuel Pool Project concluded with the ignition of the test assembly in the Cell 2 configuration. This test was conducted between the dates of February 28 and March 1, 2011. The test was started at 20:00:25 Mountain Standard Time. The applied power to the assembly was 5.0 kW, which represents an assembly approximately 17 months after offload. The power to the assembly was lost when ignition occurred. Ignition of the Zircaloy within the assembly was first indicated at the z = 3.302 m level (130 in.) at an elapsed test time of 12.66 hours based on a thermal criterion of 1,200 K (1,700°F).

5.1 Ignition Test and MELCOR results

The baseline MELCOR model used for Phase I predictions represents the bundle as a series of twelve axial nodes along the heated length. Similar to a grid convergence study, this baseline model was adapted to include more axial nodes and additional rings to represent the bundle. An axial nodalization refinement of twice as many nodes was applied to the bundle. The radial refinement consisted of repartitioning the single ring into two rings with roughly equal cross sectional areas and therefore equal bundle masses.

The MELCOR calculations were all performed with current best practice modeling parameters and sensitivity coefficients for the analysis of severe accidents, with the exception of radiative exchange factors. These exchange factors were adjusted based on the discretization of the model. Exchange factors should be based on standard expressions for simple geometries, where possible, or on experimental data or detailed radiation calculations for complicated geometries involving intervening surfaces, such as for radiation between “representative” structures in cells containing a number of similar structures (e.g. fuel rod bundles). In absence of this information, they should be treated parametrically to examine the effects of radiation on the course of a calculation. The values for exchange factors are user defined input and can range from zero to unity. The baseline values for the MELCOR model are 0.1 for both axial and radial exchange factors. The baseline model is therefore denoted as 12A_1R (0.1A, 0.1R) for 12 axial nodes, 1 radial ring, 0.1 axial exchange factor, and 0.1 radial exchange factor. Sensitivity analyses for the radial exchange factor was not considered, as it is ignored by MELCOR in a single ring model.

5.1.1 Thermal-Hydraulic Comparisons

Figure 5.1 shows temperature as a function of time for the test maximum, test average (at maximum temperature elevation), and peak cladding temperature of the MELCOR single ring, twelve axial node model. The MELCOR results are again denoted by the number of axial nodes and number of rings, along with the applied axial and radial radiative exchange factors (e.g. 12A_1R (0.1A, 0.1R) denotes the single ring, twelve node model with axial and radial exchange factors of 0.1). The test values are truncated beyond the time of ignition due to loss of instrumentation and noise in the remaining TCs. The MELCOR post-test prediction of ignition time was within one percent of the observed test ignition time.

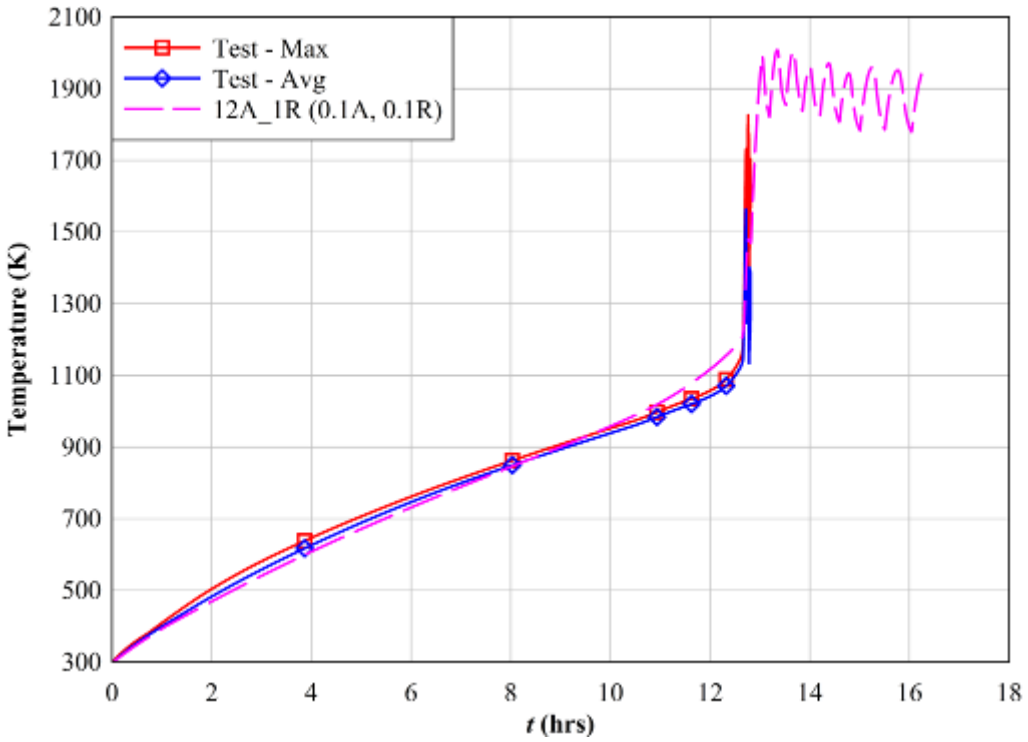

Figure 5.1 **Cell 2 bundle temperatures as a function of time at 5.0 kW simulated decay power for the maximum test temperature (red squares), average test temperature (blue diamonds), and MELCOR 12A_1R (pink dashed)**

Figure 5.2 shows the axial temperature distribution in the assembly prior to ignition at t = 12 hours for the test maximum, test average, test minimum, and the MELCOR post-test prediction with 5.0 kW input power. The model over predicts the temperature for all locations in the assembly. The MELCOR PCT is within 60 K (108°F) of the test maximum, and the prediction of the PCT location is accurate to within the nodal resolution of the model. However, the onset of oxygen consumption in the MELCOR model occurs prior to what was shown by the experiment, as seen in Figure 5.5. The MELCOR model and experiment PCT are not expected to match at 12 hours because the higher-than-measured oxidation in the MELCOR model is forcing the temperature higher. Therefore, the axial temperature profiles at 10 hours were compared when MELCOR and the experiment were in more agreement with respect to oxygen consumption.

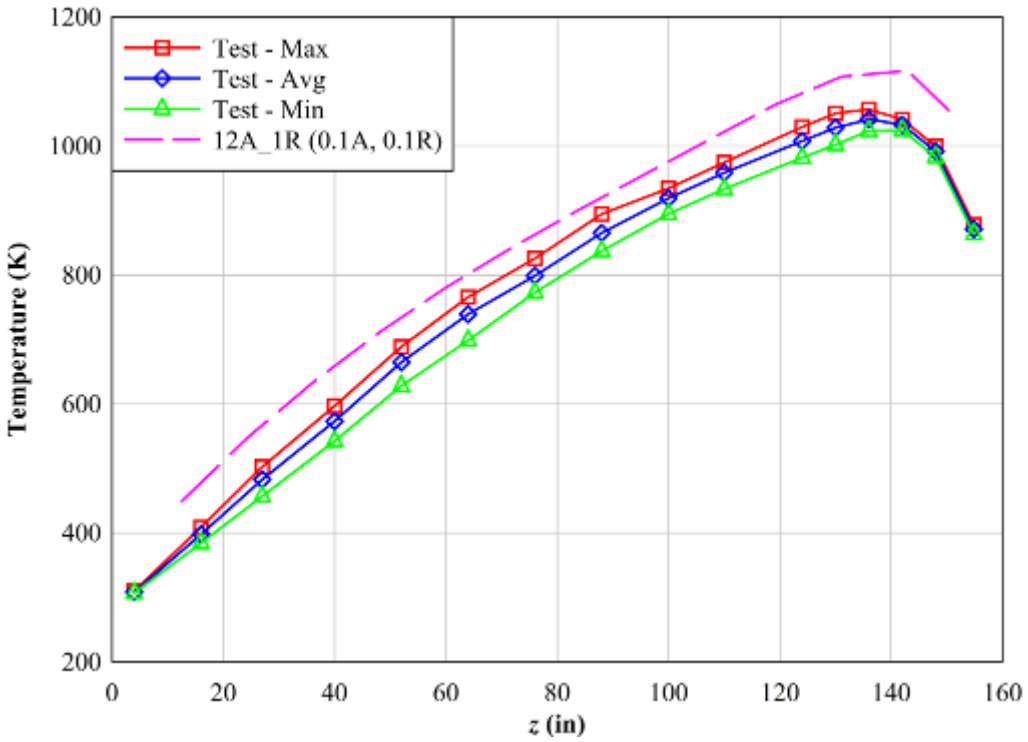

Figure 5.2 **Bundle temperatures as a function of axial height in the assembly at 5.0 kW simulated decay power and 12 hours elapsed for the test maximum (red squares), test average (blue diamonds), test minimum (green triangles), and MELCOR 12A_1R (pink dashed)**

Figure 5.3 shows the axial temperature distribution in the assembly prior to ignition at t = 10 hours for the test maximum, test average, test minimum, and MELCOR post-test prediction with 5.0 kW input power. The model over predicts the temperature for all locations in the assembly but is within 28 K (50°F) of the test maximum. The prediction of PCT location is accurate to within the nodal resolution of the model.

The measured and predicted induced flow rates for the ignition test are shown in Figure 5.4. The MELCOR results are within the experimental uncertainty until the point of ignition, as mentioned earlier.

As observed in the analysis of ignition test, the MELCOR input model of 12 axial nodes and 1 radial node, captured the ignition time accurately, within 1 percent.

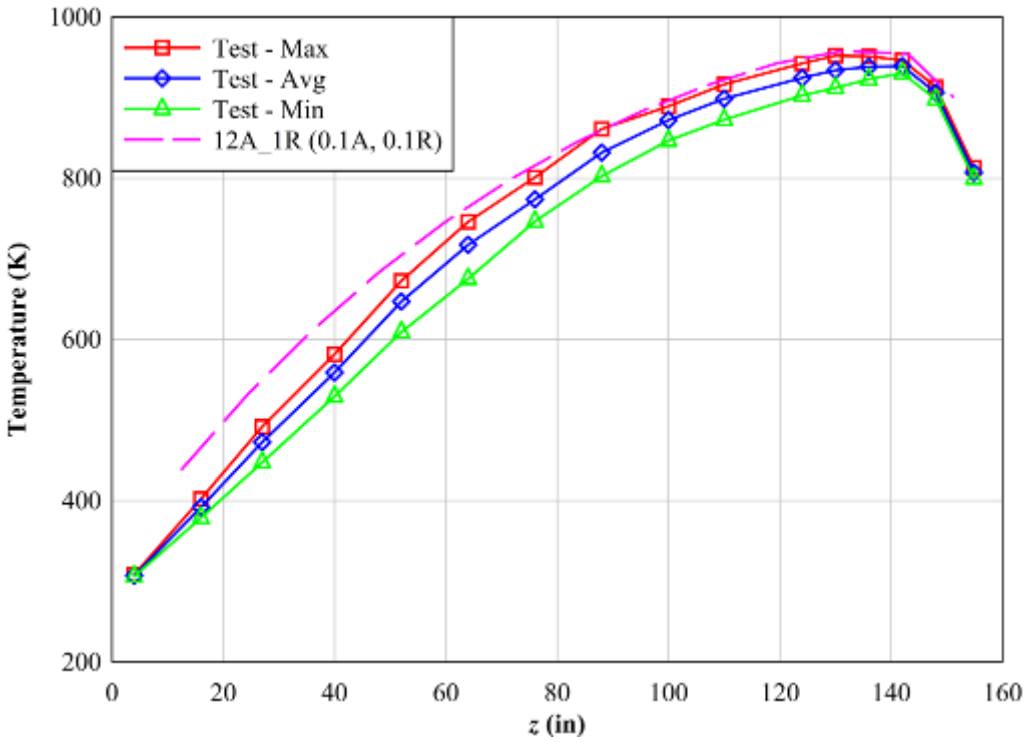

Figure 5.3 **Bundle temperatures as a function of axial height in the assembly at 5.0 kW simulated decay power and 10 hours elapsed for the test maximum (red squares), test average (blue diamonds), test minimum (green triangles), and MELCOR 12A_1R (pink dashed)**

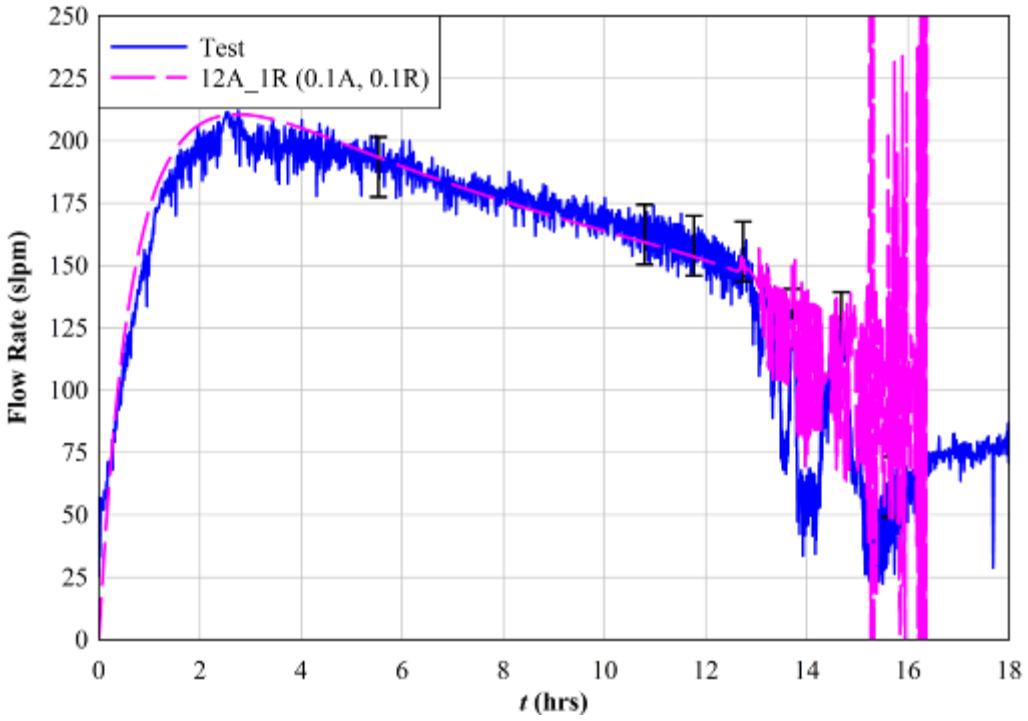

Figure 5.4 **Induced flow rate within the Cell 2 assembly at a simulated decay power of 5.0 kW for the test (blue solid) and MELCOR 12A_1R (pink dashed)**

5.1.2 Exhaust Stream Analyses

5.1.2.1 Oxygen Concentration Monitoring

Figure 5.5 gives the bundle, annulus, and MELCOR oxygen concentrations in the assembly as a function of time. The ceramic, bundle sample tube became caught in the top bus plate and was shattered at 13.2 hours as the assembly shifted and slumped. The bundle O_2 sensor and RGA slipstream sample lines were reconnected to the main annulus sample line at 13.4 hours. The annulus O_2 sensor was abandoned after 13.4 hours. Figure 5.6 shows the state of the sample lines at various times of interest throughout the test.

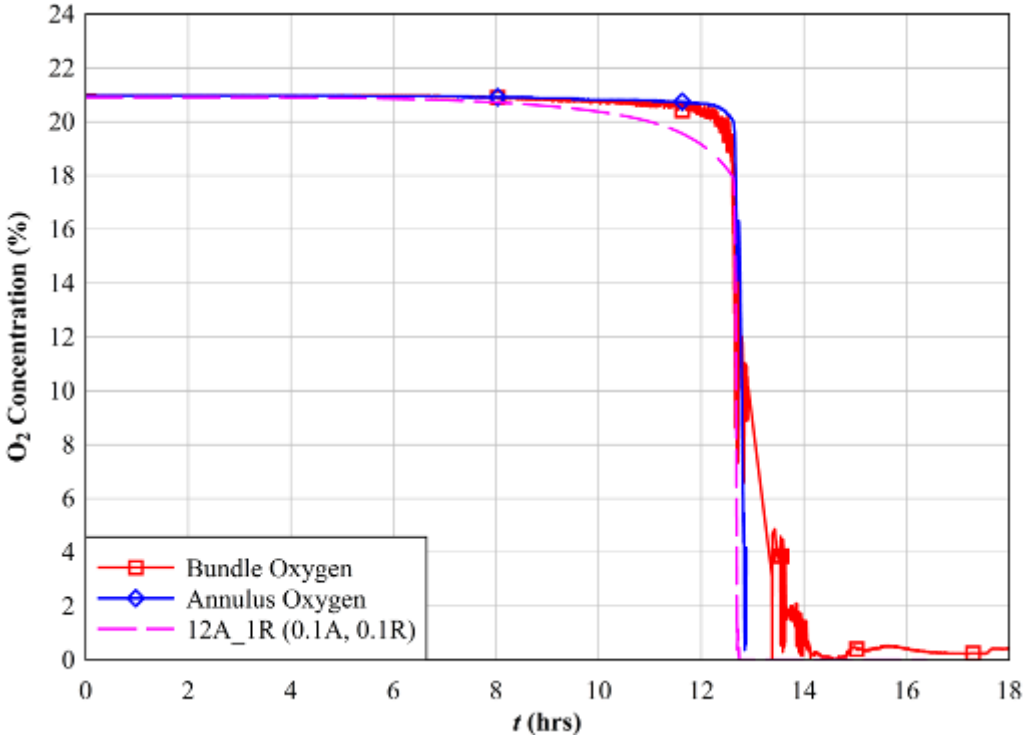

Figure 5.5 **Exit oxygen concentration as a function of time for assembly bundle (red squares), assembly annulus (blue diamonds), and MELCOR 12A_1R (pink dashed)**

Figure 5.6 **Overhead photographs of the assembly exit and exhaust sampling lines showing *a*) the initial configuration, *b*) immediately prior to the break in the bundle sample line, and *c*) immediately after the break in the bundle sample line**

5.1.2.2 Residual Gas Analyzer

Figure 5.7 shows the mole or volume fraction of nitrogen, oxygen and argon as determined by the RGA analysis. The RGA analysis was started eleven hours into the test, which was almost two hours before ignition. Near the end of the test at 17.7 hours, ambient air was sampled for calibration. After initial evaluation of the data, additional calibration of the RGA was performed to test the validity of the air calibration for the samples that were devoid of oxygen. Two calibration gases were used. The first contained 1.22 percent argon in nitrogen, which represents the argon concentration naturally in air after all the oxygen is removed. The other calibration gas contained 4.76 percent argon in nitrogen, which represents the maximum argon concentration apparently measured, based on the single air calibration. The apparent argon concentration in the 1.22 percent and 4.76 percent calibration gases was determined to be 1.66 percent and 7.85 percent respectively based on the air calibration. A linear correction correlation was used to adjust the argon and nitrogen concentrations for the samples collected during the burn phase when the oxygen concentration was essentially zero. The single point air calibration was solely used up until this point when significant oxygen was present.

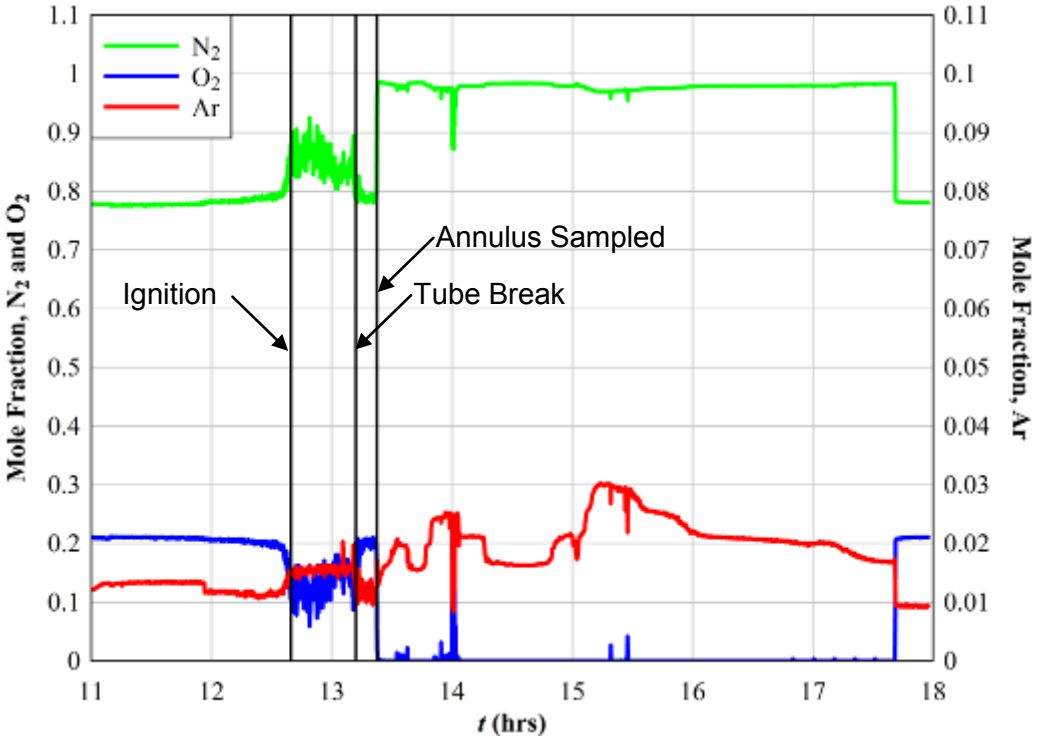

Figure 5.7 Mole fraction of nitrogen, oxygen, and argon as a function of time during the ignition test

At about 12.66 hours, the oxygen concentration began to drop sharply indicating ignition had begun. Shortly after ignition at 13.2 hours, a mishap occurred when the ceramic tube on the top bus plate snapped (See Figure 5.6). Due to the break in the sampling tube, the RGA sample location changed to just above the top of the storage cell. This resulted in the dilution of the sample with ambient air. At 13.4 hours, the bundle sample was abandoned and the RGA was configured to draw sample from the annulus sample location.

Once the sample was drawn from the annulus, the oxygen concentration dropped to zero due to the zirconium oxidation reaction. The removal of oxygen from the gas stream increased the nitrogen concentration significantly to 0.978 but not enough to be explained solely by the absence of oxygen, which would be 0.988. However, the argon concentration increased by a factor of 1.7 times greater than can be explained by the absence of oxygen. These combined observations are consistent with significant nitrogen removal by zirconium nitride formation.

When nitrogen is not being consumed, the ratio of the nitrogen to argon in atmospheric air should remain constant at 83.6, termed here the background ratio. However, due to previous testing of the argon purge system, the concentration of argon inside the cylindrical boiling facility vessel was artificially elevated above ambient to about 1.2 percent before the ignition test. The corresponding nitrogen to argon ratio was measured at 66.7. Thus, the background ratio during the ignition test was between 66.7 and 83.6. The uncertainty in the background ratio corresponds to uncertainty in the estimated nitrogen removal and ZrN formation.

Since argon is inert, any change in this ratio should be due to a change in the relative amount of nitrogen present. A ratio below the background value signifies nitrogen removal. Figure 5.8 shows the nitrogen to argon concentration ratio. After the sample point was switched to the annulus, the measured nitrogen-to-argon ratio was 48.6, indicating that between 27 percent and 42 percent (depending on the background ratio assumed) of the nitrogen drawn into the assembly was converted to ZrN during this burn phase of the experiment. Based on this nitrogen consumption and the measured inlet flow rate, the initial zirconium in the assembly converted to ZrN during this period was estimated to be between 20 and 40 percent. The amount of zirconium oxide formed was estimated with greater certainty based on the measured flow rate and assuming total oxygen consumption. During this first pass of the burn front 14 percent ± 3 percent of the initial zirconium was converted to ZrO_2. Also plotted in Figure 5.8 is the total induced flow. During the burn phase, the induced flow correlates with the nitrogen to argon ratio. When the flow is high the ratio increases, signifying that more nitrogen makes it out of the assembly. When the flow is low the ratio is low signifying that less nitrogen makes it out the top of the assembly. The correlation of the nitrogen argon ratio with the independent induced flow measurement provides some confidence in the relative accuracy of the method. The absolute accuracy is still under scrutiny. The single point calibration with air inherently assumes a linear detector response with changes in concentrations. This assumption may not be valid, especially for argon, which underwent a multi-fold increase in concentration. These results indicate that the hot oxygen starved environment left after the passage of the burn front is ideal for significant zirconium nitride formation.

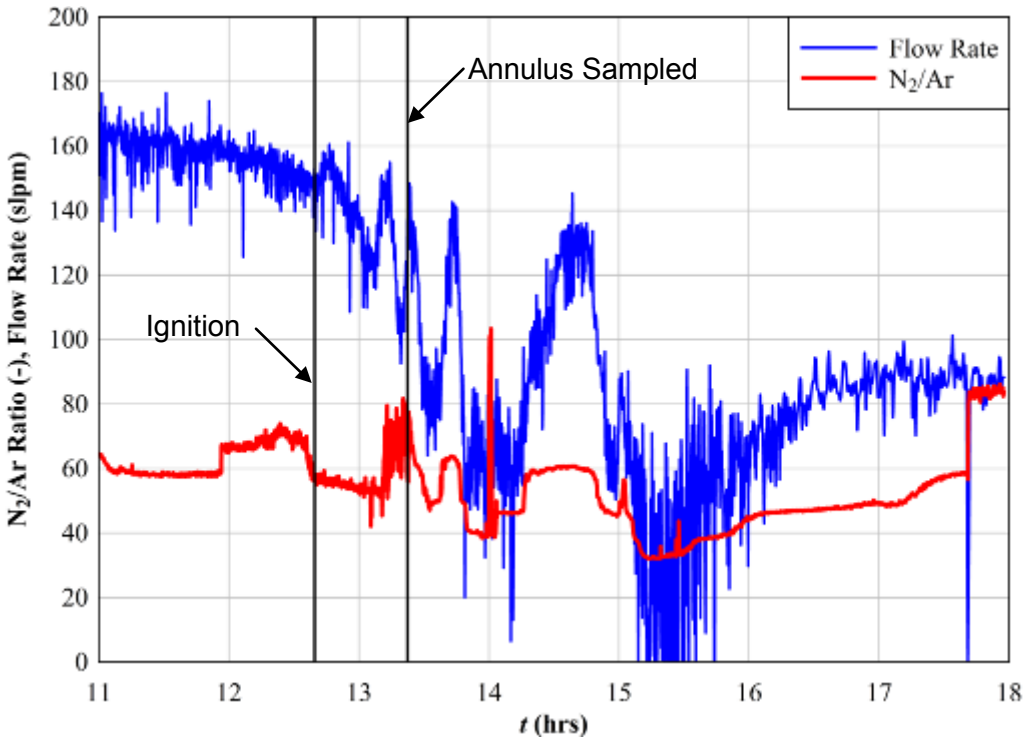

Figure 5.8 **Ratio of nitrogen to argon in the exhaust stream and assembly flow rate as a function of time**

5.1.3 Post-Test Examination and Deconstruction

The SFP Phase I test assembly continued to react for several days after the first ignition. The temperature within the assembly was low enough after about one week to allow for examination and removal of the test materials from the vessel at the Cylindrical Boiling facility. As expected, the internal geometry of the fuel bundle and storage pool cell were heavily distorted due to the severe thermal environment caused by the ignition of the zirconium. Figure 5.9 shows a sequence of photographs throughout the deconstruction process. These photographs are labeled alphabetically to denote chronology. The outer thermal radiation barrier was removed first, followed by the high-temperature insulation. The top ~0.6 m (24 in.) portion of the fuel bundle was detached and lifted from the assembly as shown in Figure 5.9 (*b*) and (*c*). Although heavily oxidized, the stainless steel pool cell remains structurally intact in this segment. This segment of the fuel bundle represents the most preserved piece and also coincides with the fuel located above the original ignition location. The fuel located below this location was largely unstable and disintegrated upon removal of the insulation. The stainless steel pool cell in this lower portion either had relocated further down the assembly or was so heavily oxidized as to be no longer structurally viable.

Figure 5.10 shows photographs from various perspectives of the Phase I fuel bundle. Figure 5.10 (*a*) is the view through the LDA port with the insulation and quartz window removed. Slag from the pool cell is evident in the lower portion of the port. Figure 5.10 (*b*) and (*c*) show the initial point of ignition, z = 3.302 m (130 in.), before and after the removal of the top section, respectively. The top ~0.6 m (24 in.) portion of the fuel bundle is shown in Figure 5.10 (*d*). Figure 5.10 (*e*) and (*f*) show the lower part of the fuel bundle from different angles.

Figure 5.9 Deconstruction photographs of the SFP Phase I test assembly

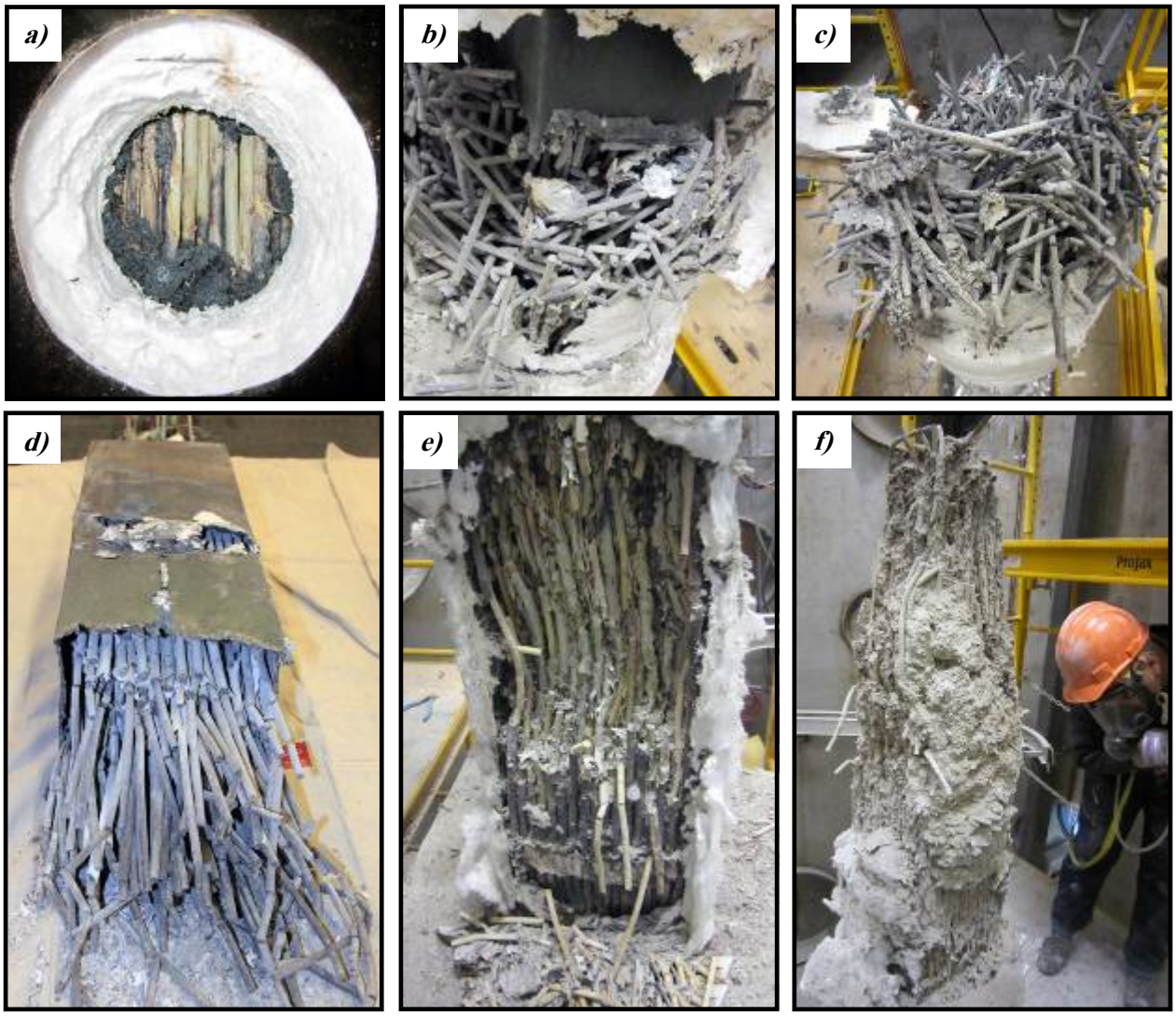

Figure 5.10 Photographs of the SFP Phase I fuel bundle after the ignition test

5.2 MELCOR Sensitivity Studies

5.2.1 Axial Nodalization Sensitivity (24A_1R)

Figure 5.11 shows temperature as a function of time for the test maximum, test average at maximum temperature elevation, and peak cladding temperature of the MELCOR single ring, twenty-four axial node model for the 5 kW ignition case. The axial radiative exchange factors of the single ring, twenty-four axial node model had to be increased compared to the twelve node model to account for the finer nodalization. The axial radiative exchange factor adjustment is made because the nodes are shorter, which effectively increases the node-to-node view factor. The MELCOR results for this model were again within one percent of the observed ignition test time.

Figure 5.12 shows the axial temperature distribution in the assembly prior to ignition at t = 10 hours for the test maximum, test average, test minimum, and the MELCOR 24A_1R model. The model over predicts the temperature for all locations in the assembly. The MELCOR PCT is within 35 K (63°F) of the test maximum, and the prediction of PCT location is accurate to within the nodal resolution of the model.

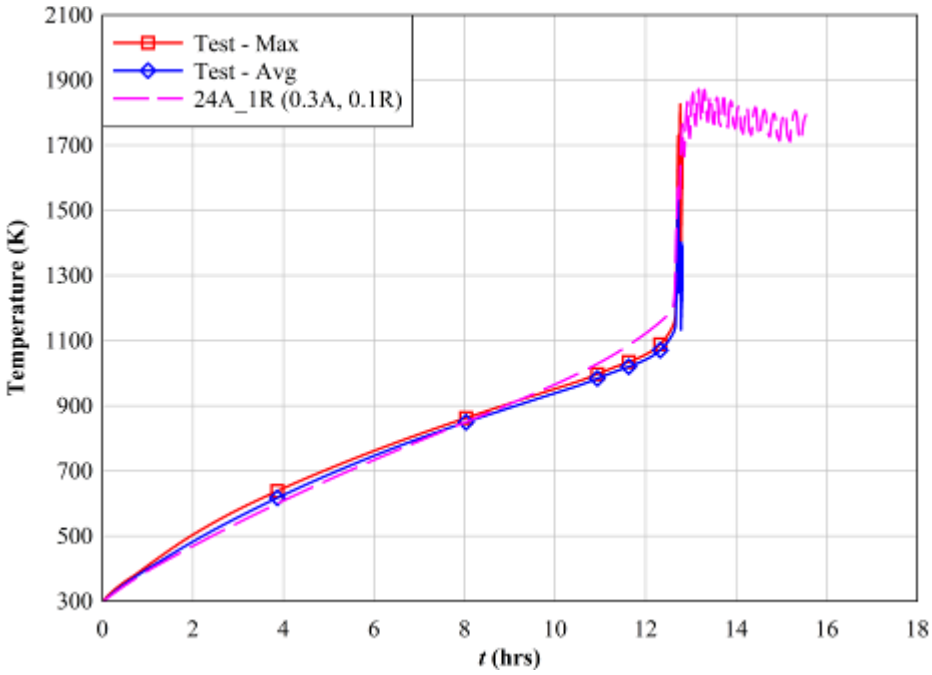

Figure 5.11 **Cell 2 bundle temperatures as a function of time at 5.0 kW simulated decay power for the maximum test temperature (red squares), average test temperature (blue diamonds), and MELCOR 24A_1R (pink dashed)**

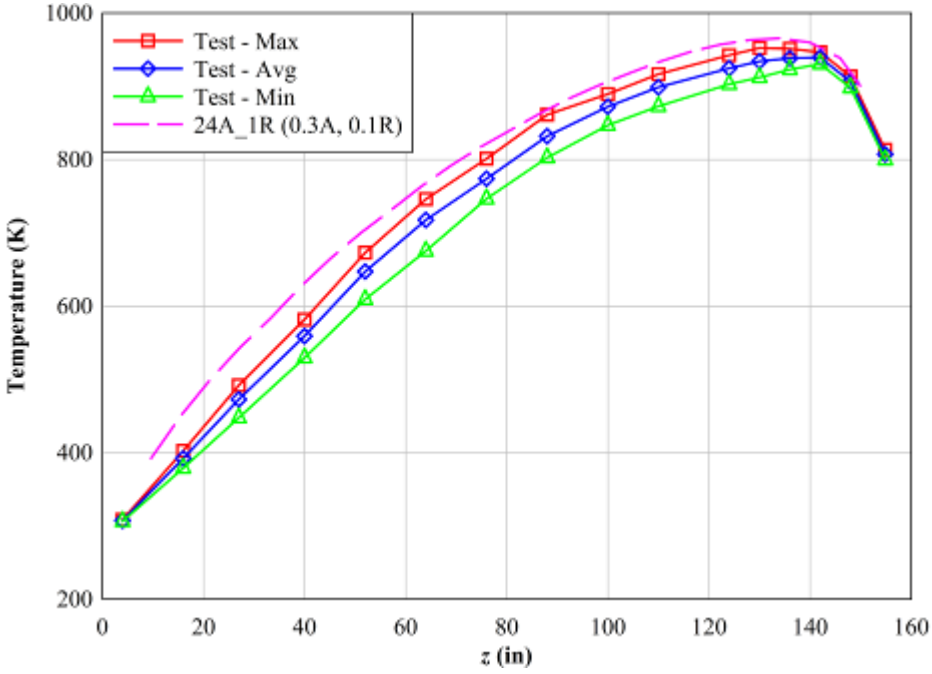

Figure 5.12 **Bundle temperatures as a function of axial height in the assembly at 5.0 kW simulated decay power and 10 hours elapsed for the test maximum (red squares), test average (blue diamonds), test minimum (green triangles), and MELCOR 24A_1R (pink dashed)**

5.2.2 Radial Nodalization Sensitivity (12A_2R)

Figure 5.13 shows temperature as a function of time for the test maximum, test average, and peak cladding temperature of the MELCOR two ring, twelve axial node model. The assembly was divided in two concentric rings in the MELCOR model. The inner ring represented 132 heated rods and the outer ring represented the remaining 132 heated rods and the rack. The temperature of the first, inner ring is denoted as 12A_2R[1] in the legend. The second, outer ring is denoted as 12A_2R[2]. This convention is repeated throughout the remainder of this report. The two ring model radial radiative exchange factors were increased to unity. The increase to unity was made because a large fraction of the rods in ring 1 are expected to radiatively interact in ring 2. If a smaller exchange factor was used, ring 1 temperatures would be unrealistically high. The MELCOR time to ignition was again within one percent of the observed ignition test time.

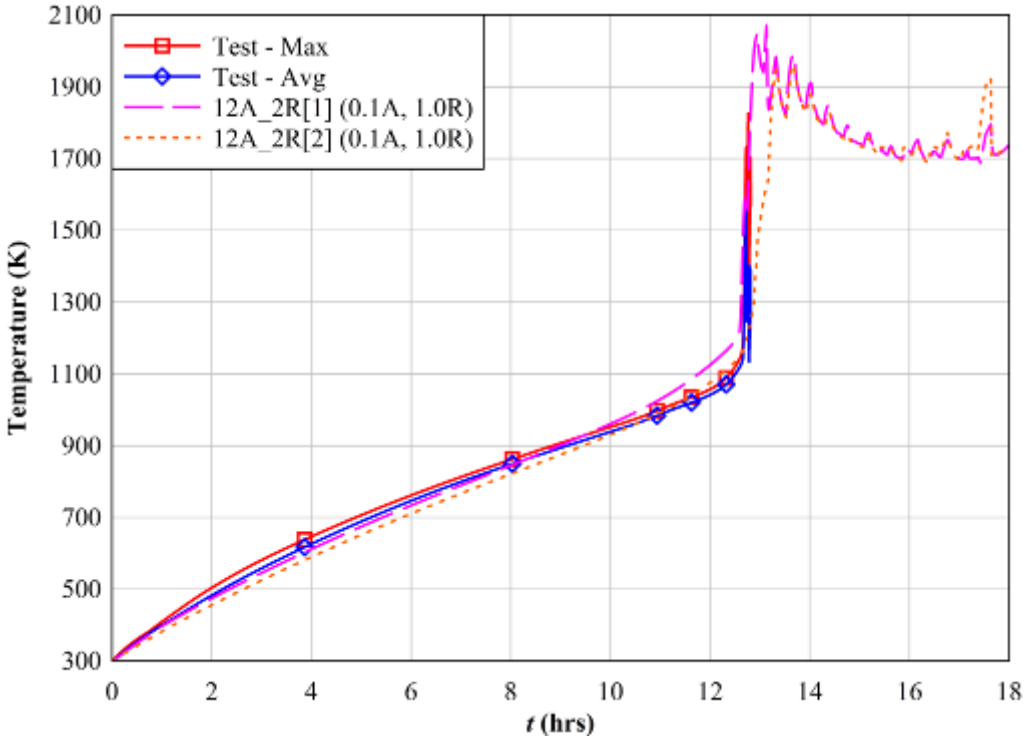

Figure 5.13 Cell 2 bundle temperatures as a function of time at 5.0 kW simulated decay power for the maximum test temperature (red squares), average test temperature (blue diamonds), MELCOR 12A_2R[1] (pink long dashed), and MELCOR 12A_2R[2] (orange short dashed)

Figure 5.14 shows the axial temperature distribution in the assembly prior to ignition at t = 10 hours for the test maximum, test average, test minimum, and both MELCOR rings. The model over predicts the temperature for all locations in the assembly for ring 1. The MELCOR PCT is within 30 K (54°F) of the test maximum, and the prediction of PCT location is accurate to within the nodal resolution of the model.

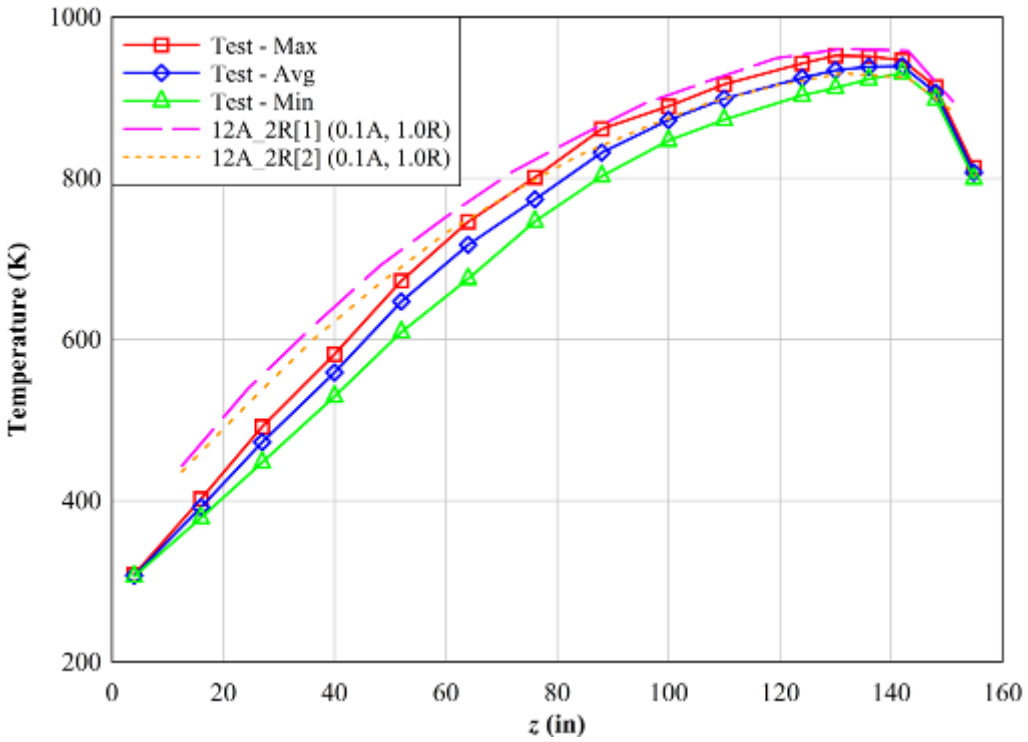

Figure 5.14 **Bundle temperatures as a function of axial height in the assembly at 5.0 kW simulated decay power and 10 hours elapsed for the test maximum (red squares), test average (blue diamonds), test minimum (green triangles), MELCOR 12A_2R[1] (pink long dashed), and MELCOR 12A_2R[2] (orange short dashed)**

5.2.3 Combined Axial and Radial Nodalization Sensitivity (24A_2R)

Figure 5.15 shows temperature as a function of time for the test maximum, test average, and peak cladding temperature of the MELCOR two ring, twenty-four axial node model. The axial exchange factor had to be increased in the two ring model, similarly to the 24A_1R model. The MELCOR result was within two percent of the observed ignition test time.

Figure 5.16 shows the axial temperature distribution in the assembly prior to ignition at t = 10 hours for the test maximum, test average, test minimum, and the MELCOR model. The model over predicts the temperature for all locations in the assembly for ring 1. The MELCOR PCT is within 40 K (72°F) of the test maximum, and the prediction of PCT location is accurate to within the nodal resolution of the model.

The results of the sensitivity study demonstrate that increasing the core nodalization beyond the baseline model does not noticeably improve accuracy for the purposes of the SFP Phase I modeling efforts. Given the treatment of the thermal system as a lumped mass within MELCOR, refined nodalizations are not expected to necessarily improve the agreement with the test data as long as the original discretization is reasonably resolved. Furthermore, user inputs such as axial and radial exchange factors require re-examination with each node refinement.

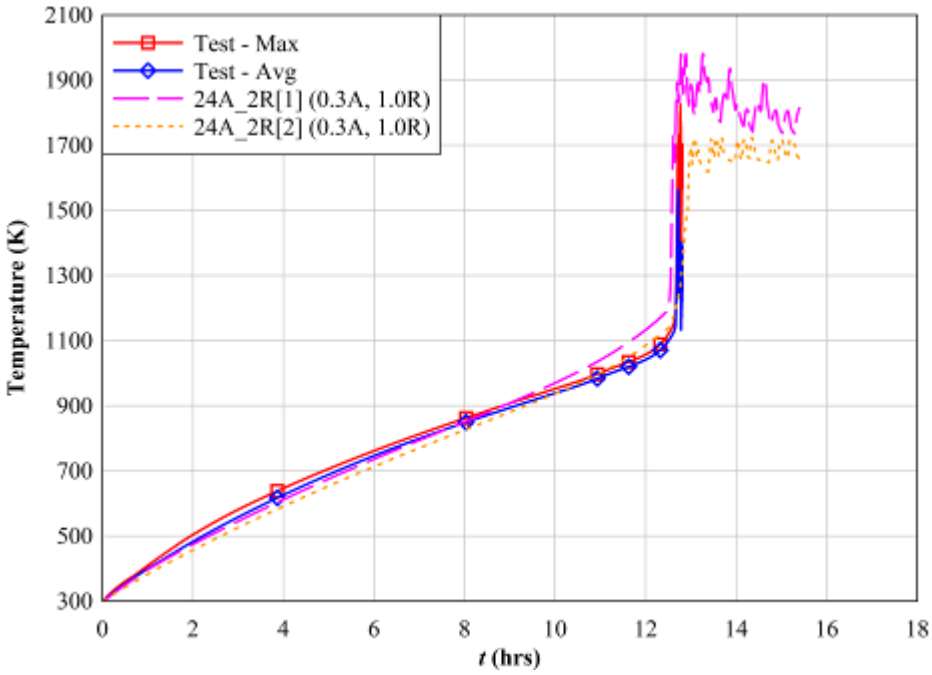

Figure 5.15 **Cell 2 bundle temperatures as a function of time at 5.0 kW simulated decay power for the maximum test temperature (red squares), average test temperature (blue diamonds), MELCOR 24A_2R[1] (pink long dashed), and MELCOR 24A_2R[2] (orange short dashed)**

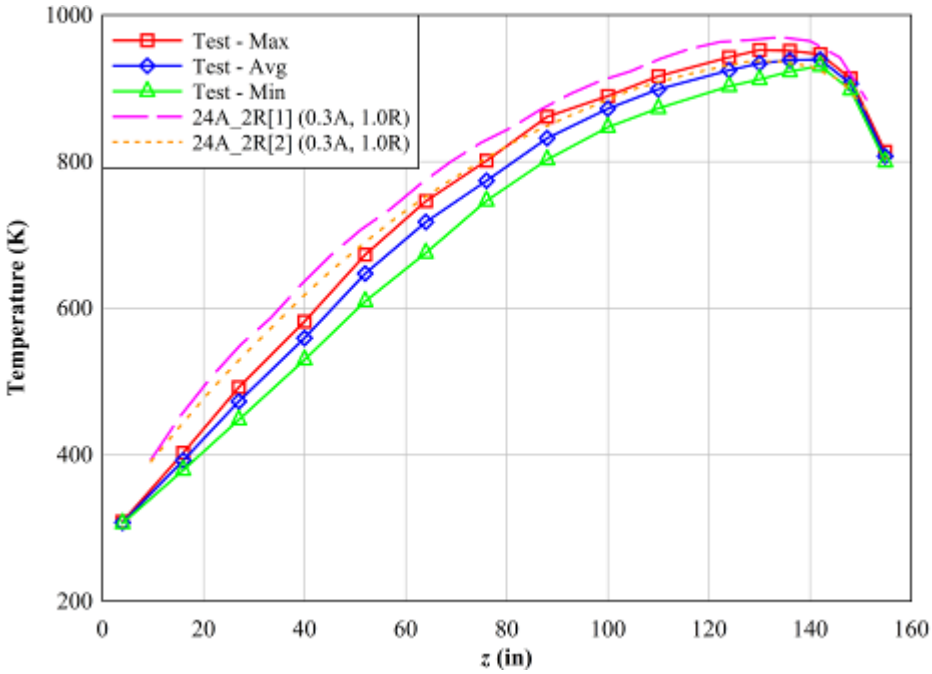

Figure 5.16 **Bundle temperatures as a function of axial height in the assembly at 5.0 kW simulated decay power and 10 hours elapsed for the test maximum (red squares), test average (blue diamonds), test minimum (green triangles), MELCOR 24A_2R[1] (pink long dashed), and MELCOR 24A_2R[2] (orange short dashed).**

6 SUMMARY

Testing of a single, full-scale 17×17 PWR mock fuel assembly for Phase I of the Spent Fuel Pool Project has been completed. The near-prototypic fuel assembly was constructed to measure the thermal-hydraulic response of spent fuel under complete loss-of-coolant accident scenarios. Testing included a pre-ignition series for Cell 1 and Cell 2 and concluded with a final, destructive ignition experiment for Cell 2. The assembly in the Cell 1 configuration, ID = 221.3 mm (8.71 in.) and in the Cell 2 configuration, ID = 223.4 mm (8.80 in.), were tested in air environments below ignition temperatures for simulated decay powers of 0.5, 1.0, 1.5, 2.0, 2.5, 3.0, and 3.5 kW. The final ignition test was conducted only for Cell 2 at a simulated decay power of 5.0 kW, or equivalent offload age of approximately 17 months.

The ignition test was conducted with an applied power of 5.0 kW. The time to ignition was captured by MELCOR to within one percent of the observed time. The MELCOR maximum temperature was within 60 K (108°F) of the maximum test temperature for times prior to ignition. Nodalization refinements to the baseline MELCOR model were performed to examine sensitivity of the model to increased discretization of the axial dimension and the effect of additional rings to capture transverse thermal gradients. Both axial and radial grid convergence efforts did not yield improvements to the predictions of temperature or time to ignition. Through sensitivity calculation for Cell 1 and Cell 2 cases, it was concluded that a Σk value of 30 matches very well the data for both Cell 1 and Cell 2. On the other hand, a S_{LAM} value of 145 matches very well the data for Cell 1 while S_{LAM} values between 146 and 133 match the data for Cell 2. In the ignition test, the MELCOR input model of 12 axial nodes and 1 radial node, captured the ignition time accurately, within 1 percent.

Laser Doppler anemometer (LDA) measurements and computational fluid dynamics (CFD) simulations were performed for both heated and unheated cases. These data indicate that flow is drawn preferentially into the bundle from the annulus for naturally induced flows as compared to forced flows at z = 0.442 m (1.45 ft). Based on the integrated line average mass fluxes of the LDA data, the bundle mass flow fraction increased by 0.030 and 0.034 over the forced flow case for 0.5 and 1 kW, respectively. Further analysis of the CFD data reveals that the bundle mass flow fraction for naturally induced flows initially increases in the lower part of the assembly and then decreases as the flow moves up the assembly. The highest simulated power case of 3.5 kW indicated that the mass flow fractions approach those in the forced flow case for z ≥ 1.5 m (4.9 ft).

During the ignition test, a residual gas analyzer (RGA) was used to monitor the amount of nitrogen and argon exiting the top of the assembly. The ratio of nitrogen to argon was used to determine if nitrogen was being consumed by reaction with zirconium. While encountering some sampling difficulties, the RGA successfully measured a significant amount of nitrogen consumption at the start of ignition and during the burn front progression to the bottom of the assembly. The single point calibration with air was used for samples containing significant concentrations of oxygen. The analysis of two additional calibration gases allowed adjustment of the air calibration for samples that were devoid of oxygen.

During the burn phase, all of the oxygen was removed from the air drawn into the assembly converting 14 percent of the initial zirconium to ZrO2. Depending on which background ratio was assumed, between 20 percent to 40 percent of the zirconium in the assembly was converted to ZrN. These results indicate that the hot oxygen starved environment remaining after the passage of the burn front is ideal for significant zirconium nitride formation.

7 REFERENCES

1. E.R. Lindgren, and S.G. Durbin, “Characterization of Thermal-Hydraulic and Ignition Phenomena in Prototypic, Full-Length Boiling Water Reactor Spent Fuel Pool Assemblies after a Complete Loss-of-Coolant Accident,” NUREG/CR 7143, April 2013.

2. M. Steinbrück, J. Jung, and M. Walter, “Separate-Effects Tests on the Investigation of High-Temperature Oxidation Behavior and Mechanical Properties of Zircaloy-2 to Be Used in the SFP PWR Tests,” Karlsruher Institute for Technology Letter Report, 2010.

3. S.G. Durbin, and E.R. Lindgren, “Laminar Hydraulic Analysis of a Commercial Pressurized Water Reactor Fuel Assembly,” NUREG/CR 7144, March 2013.

4. J. Cardoni, “MELCOR Model for an Experimental 17×17 Spent Fuel PWR Assembly,” SAND2010-8249, November 2010.

5. F. P. Incropera et al., "*Fundamentals of Heat and Mass Transfer*," 4th edition, John Wiley & Sons, Inc. (1998).

APPENDIX A – ERROR PROPAGATION ANALYSIS

The error and uncertainty inherent to an experimental result are critical to the accurate interpretation of the data. Therefore, the uncertainties in the experimental measurements are estimated in this section. Results of this analysis are given, followed by a general description of the method used and a brief explanation of the source of each reported measurement uncertainty.

The overall standard uncertainty of an indirect measurement *y*, dependent on *N* indirect measurements x_i, is defined in Equation A.1. The standard uncertainty associated with an indirect measurement is analogous to the standard deviation of a statistical population.

$$u^2 = \sum_{i=1}^{N} \left(\frac{\partial y}{\partial x_i} u_i \right)^2 \qquad \text{A.1}$$

Here, *u* is used to define the standard uncertainty of a measurement.

The expanded uncertainty *U* is reported in this appendix and defines the bounds that include 95 percent of the possible data. The expanded uncertainty is usually defined as some multiple of the standard uncertainty. For purposes of this report, all uncertainty measurements are assumed to behave according to a normal distribution. Therefore, Equation A.2 shows the definition of the expanded uncertainty as used in the following sections for a 95 percent confidence interval, where the factor of 1.96 has been rounded to a value of 2.

$$U = 2 \cdot u \qquad \text{A.2}$$

A.1 Uncertainty in Average Bundle Velocity

The uncertainty in the bundle velocity was determined using error propagation analysis (EPA) for the blocked guide tube measurements in the Cell 2 configuration (ID = 223.4 mm (8.80 in.)). The assembly velocity was determined from Equation A.3 in which Q_i is the volumetric flow rate in slpm for each flow controller, $A_{assembly}$ is the cross sectional area of the assembly, R is gas constant for air, T is the inlet air temperature, and P is the ambient air pressure. The first term in the equation represents the conversion from slpm to kg/s.

$$w_o = \left(\frac{0.001 \, \mathrm{m^3/l} \cdot \rho_{STP}}{60 \, \mathrm{s/min}} \right) \frac{\sum_{i=1}^{8} Q_i}{A_{assembly}} \left(\frac{R \cdot T}{P} \right) \qquad \text{A.3}$$

Equation A.4 gives the relation between the overall uncertainty of w_o and the contributions from the measurement uncertainties of $A_{assembly}$, Q, T, and P. The uncertainty in these fundamental measurements are defined in Sections A.1.1 through A.1.4, respectively.

$$u_{w_o}^2 = \left(\frac{0.001 \text{ m}^3/\text{l} \cdot \text{STP}}{60 \text{ s/min}} \right)^2 \left[\sum_{i=1}^{8} \left(\frac{RT}{P \cdot A_{assembly}} u_{Q_i} \right)^2 + \left(\frac{Q_{tot} R}{P \cdot A_{assembly}} u_T \right)^2 + \left(\frac{Q_{tot} RT}{P^2 \cdot A_{assembly}} u_P \right)^2 + \left(\frac{Q_{tot} RT}{P \cdot A_{assembly}^2} u_{A_{assembly}} \right)^2 \right] \quad \text{A.4}$$

Table A.1 summarizes the values used to determine the overall uncertainty of the assembly velocity. The overall uncertainty in w_o was found for the highest volumetric flow rate achieved during testing, Q_{tot} = 2,300 slpm, at a typical ambient condition of T = 298 K (77°F), P = 83.4 Pa (12.1 psi), and $A_{assembly}$ = 0.0283 m^2 (0.305 ft^2). The standard uncertainty was determined to be u_{w_o} = 0.039 m/s (0.128 ft/s). The uncertainty was dominated by the assembly cross-sectional area ($A_{assembly}$) and the air temperature (T) contributing 96 and 3 percent of the overall uncertainty, respectively. The remainder was due to the uncertainty in the flow rate and atmospheric pressure.

Table A.1 Measurement uncertainties and intermediate calculations for w_o

Measurement, x_i	Units	Value	Standard uncertainty, u_i	Influence coefficient ($u_i \cdot [(\partial w_o/\partial x_i)/w_o]$)	Contribution
Q_1	slpm	100	0.5	0.000	0.00
Q_2	slpm	200	1.0	0.000	0.00
Q_3	slpm	300	1.5	0.001	0.00
Q_4	slpm	300	1.5	0.001	0.00
Q_5	slpm	300	1.5	0.001	0.00
Q_6	slpm	300	1.5	0.001	0.00
Q_7	slpm	400	2.0	0.001	0.00
Q_8	slpm	400	2.0	0.001	0.00
T	K	298	1.1	0.004	0.03
P	N/m^2	83400	55	0.001	0.00
$A_{assembly}$	m^2	0.0283	6.0E-04	0.021	0.96
w_o	m/s	1.793	0.039	0.0216	1.00

A.1.1 Uncertainty in Assembly Cross Sectional Area

The inner dimension of the storage cell was measured to within ±1.3 mm (±0.05 in.). The outer diameter of the simulated fuel rods was measured to within ±0.04 mm (±0.0015 in.). The outer diameter of the guide tubes was measured to within ±0.03 mm (±0.001 in.). This tolerance leads to a maximum standard uncertainty of $6 \cdot 10^{-4}$ m^2 ($2 \cdot 10^{-3}$ ft) in the hydraulic area.

Table A.2 Measurement uncertainties and intermediate calculations for $A_{assembly}$

Measurement, x_i	Units	Value	Standard uncertainty, u_i	Influence coefficient ($u_i \cdot [(\partial A_{assembly}/\partial x_i)/A_{asse}$	Contribution
OD_{pin}	m	0.0095	0.00004	0.005	0.06
OD_{GT}	m	0.0122	0.00003	0.000	0.00
ID_{pool}	m	0.2234	0.00130	0.021	0.94
$A_{assembly}$	m^2	0.0283	0.00060	0.021	1.00

A.1.2 Uncertainty in Volumetric Flow Rate Q

The volumetric flow rate was controlled with eight MKS volumetric flow controllers operated in parallel (Model # 1559A-24174). The expanded uncertainty of the volumetric flow rate was determined from the stated manufacturer's upper uncertainty of 1 percent of full scale. The standard uncertainties in flow rate were 0.5 slpm for flow controller 1, 1 slpm for flow controller 2, 1.5 slpm for flow controllers 3 through 6, and 2 slpm for flow controllers 7 and 8. The value shown in Table A.1 represents these standard uncertainties associated with the volumetric flow rate.

A.1.3 Uncertainty in Ambient Air Temperature

The air temperature was measured with a standard k-type TC. The standard uncertainty for this type of TC is u_T = 1.1 K (2.0°F).

A.1.4 Uncertainty in Ambient Air Pressure

The air pressure was measured with a Setra Systems barometer (Model 276). The uncertainty of the ambient air pressure was taken from the manufacturer's calibration sheet, which indicated an expanded uncertainty in the instrument of ±0.1 percent of full scale (110 kPa (16 psi)). Therefore, the standard uncertainty in the pressure reading is u_P = 55 Pa (0.008 psi).

A.2 Uncertainty in Pressure Drop Measurements

The manufacturer of the Digiquartz pressure transducers used in these experiments lists a *static error band* of ±0.02 percent of full scale, or ±4.1 N/m^2 (6·10^{-4} psi). This error band includes repeatability, hysteresis, and conformance. Furthermore, these error bands consider the *zero-drift* of the instrument over periods of up to 14 years. Conversations with the manufacturer indicate the experimental procedure followed for these investigations, namely the zero flow measurements to correct any zero drift and the relatively short experimental data collection times (~ 2 minutes), should place the uncertainty in any pressure data closer to the resolution of the instrument, or 1 part per million of full scale. The largest observed zero drifts in the zero flow measurements were less than 0.92 N/m^2 (1.3·10^{-4} psi), which is smaller than the plotted symbols in this report.

A.3 Uncertainty in S_{LAM} and Σk Coefficients

The uncertainties in the S_{LAM} and Σk coefficients were evaluated from the hydraulic equations that describe their behavior and the curve fit coefficients determined from the pressure drop measurements. Curve fits to pressure drop data have been presented to capture the form losses (quadratic term) and the friction losses (linear term).

$$\Delta P = a_2 \cdot w_o^2 + a_1 \cdot w_o \qquad \text{A.5}$$

The equations for S_{LAM} and Σk are written as the following.

$$S_{LAM} = 2 \cdot a_1 \left(\frac{D_H^2}{L\mu} \right) \qquad \text{A.6}$$

$$\Sigma k = \frac{2 \cdot a_2}{\rho} \qquad \text{A.7}$$

The standard uncertainties for the flow loss coefficients were determined using these equations for the Cell 2 configuration. The calculation of the standard uncertainties for S_{LAM} and Σk are outlined in Table A.3 and Table A.4, respectively. The expanded uncertainties for S_{LAM} and Σk are ±13 and 1.4, respectively. Explanations of the uncertainties in the underlying measurements are given in the following sections.

Table A.3 Measurement uncertainties and intermediate calculations for S_{LAM}

Measurement, x_i	Units	Value	Standard uncertainty, u_i	Influence coefficient ($u_i \cdot [(\partial S_{LAM}/\partial x_i)/S_{LAM}]$)	Contribution
a_1	s/m	41	0.4	0.011	0.06
D_H	m	0.0116	0.0002	0.043	0.94
L	m	4.0472	0.003	0.001	0.00
S_{LAM}	--	146	6.5	0.044	1.00

Table A.4 Measurement uncertainties and intermediate calculations for Σk

Measurement, x_i	Units	Value	Standard uncertainty, u_i	Influence coefficient ($u_i \cdot [(\partial \Sigma k/\partial x_i)/\Sigma k]$)	Contribution
a_2	s^2/m^2	12.5	0.3	0.027	0.930
ρ	kg/m^3	0.976	0.0037	0.007	0.070
Σk	--	26	0.7	0.0283	1.000

A.3.1 Uncertainty in Pressure Drop Curve Fit Coefficients

The pressure drop through the assembly was measured for various bundle velocities as shown in Figure 2.2. Curve fits to these data were used to determine the quadratic and linear coefficients. Standard statistical treatment within Excel was used to determine the standard error associated with each coefficient. The standard errors were u_{a1} = 0.4 and u_{a2} = 0.3.

A.3.2 Uncertainty in Hydraulic Diameter

The hydraulic diameter is determined from the wetted perimeter and the cross sectional flow area (Section A.1.1). Table A.5 outlines the determination of the uncertainty in the hydraulic diameter.

Table A.5 Measurement uncertainties and intermediate calculations for D_H

Measurement, x_i	Units	Value	Standard uncertainty, u_i	Influence coefficient ($u_i \cdot [(\partial D_H/\partial x_i)/D_H]$)	Contribution
$A_{assembly}$	m^2	0.0283	0.0006	0.021	0.98
P_{wet}	m	9.7715	0.0321	0.003	0.02
D_H	m	0.0116	0.0002	0.021	1.00

A.3.2.1 Uncertainty in the Wetted Perimeter

The uncertainty in the wetted perimeter was estimated using the known uncertainties in the geometry of the assembly. Table A.6 shows the quantities used to determine the uncertainty in the wetted perimeter. The uncertainty is completely determined by the variation in the heater pin diameter.

Table A.6 Measurement uncertainties and intermediate calculations for P_{wet}

Measurement, x_i	Units	Value	Standard uncertainty, u_i	Influence coefficient ($u_i \cdot [(\partial P_{wet}/\partial x_i)/P_{wet}]$)	Contribution
OD_{pin}	m	0.0095	0.00004	0.003	0.97
OD_{GT}	m	0.0122	0.00003	0.000	0.00
ID_{pool}	m	0.2234	0.00130	0.001	0.03
P_{wet}	m	9.772	0.032	0.003	1.00

A.3.3 Uncertainty in Hydraulic Length

The length of the bundle was measured to within ±6.4 mm (0.25 in.). This tolerance was taken to be the expanded uncertainty. Therefore, the standard uncertainty reported in the table is half this value.

A.3.4 Uncertainty in Air Density

The density of the air flowing through the assembly was determined using the ideal gas law and measurements of the air flow temperature (Section A.1.3) and ambient pressure (Section A.1.4). The resulting uncertainty in the determination of the air density is summarized in Table A.7. The compressibility of air at test conditions is 0.9996, validating the use of the ideal gas law.

Table A.7 Measurement uncertainties and intermediate calculations for air density, ρ

Measurement, x_i	Units	Value	Standard uncertainty, u_i	Influence coefficient ($u_i \cdot [(\partial \rho/\partial x_i)/\rho]$)	Contribution
T	K	298.0	1.1	0.004	0.969
P	N/m^2	83400	55	0.001	0.031
ρ	kg/m^3	0.976	0.004	0.004	1.000

A.4 Uncertainty in Hot Wire Anemometer Measurements

Two types of hot wire anemometers were initially installed for measurement of the naturally induced flow rate through the assembly. These included the Dwyer Model 641RM and the TSI Model 8455. Only the TSI measurements were included in this report. Details of the two Dwyer hot wires are included in the Cell 2 Quick Look report. Because the data from the Dwyer hot wires is still included in the ignition data files, estimates of the uncertainty in the Dwyer hot wires is included in this error propagation analysis.

Figure A.1 shows the calibration curves for all three hot wires in the Cell 2 configuration. The uncertainties in the instrument voltages were determined from manufacturer specifications (see Sections A.4.1 and A.4.2). The uncertainties in the curve fit coefficients are estimated in Section B.4.3.

The standard uncertainties in the TSI and Dwyer hot wires were determined to be ±6 and ±9 slpm, respectively. Therefore the 95 percent confidence interval in these measurements were ±12 and ±18 slpm for the TSI and Dwyer hot wires, respectively. Although the uncertainty calculations for the Dwyer hot wire was calculated only using Dwyer 2, the uncertainty in Dwyer 1 is assumed to be equivalent to the Dwyer 2 values.

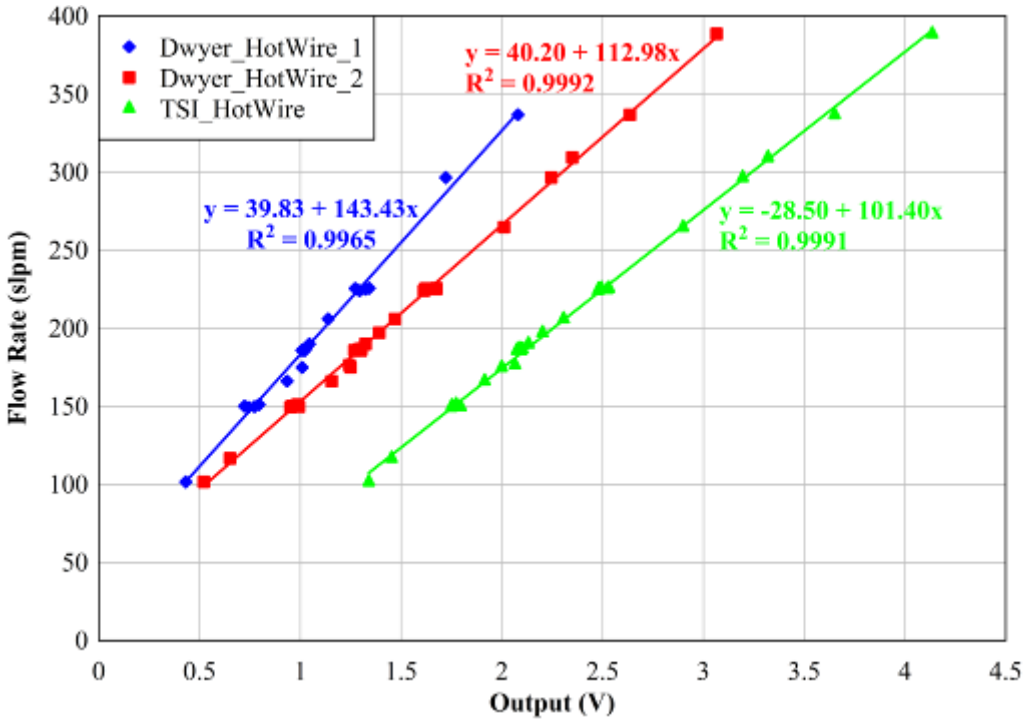

Figure A.1 **Flow rate as a function of hot wire anemometer voltage**

Table A.8 **Measurement uncertainties and intermediate calculations for assembly flow rate from the TSI hot wire**

Measurement, x_i	Units	Value	Standard uncertainty, u_i	Influence coefficient ($u_i \cdot [(\partial Q_{TSI}/\partial x_i)/Q_{TSI}]$)	Contribution
V_{TSI}	V	2	0.05	0.029	0.797
$a_{TSI,0}$	slpm	-28.5	1.9	0.011	0.117
$a_{TSI,1}$	slpm/V	101.4	0.8	0.010	0.086
Q_{TSI}	slpm	175	6	0.032	1.000

Table A.9 **Measurement uncertainties and intermediate calculations for assembly flow rate from the Dwyer 2 hot wire**

Measurement, x_i	Units	Value	Standard uncertainty, u_i	Influence coefficient ($u_i \cdot [(\partial Q_{Dwyer2}/\partial x_i)/Q_{Dwyer2}]$)	Contribution
V_{Dwyer2}	V	1.19	0.08	0.049	0.962
$a_{Dwyer2,0}$	slpm	40.2	1.3	0.008	0.023
$a_{Dwyer2,1}$	slpm/V	113.0	0.9	0.006	0.014
Q_{Dwyer2}	slpm	175	9	0.049	1.000

A.4.1 Uncertainty in TSI Hot Wire Anemometer

The standard uncertainty of the TSI Model 8455 hot wire was stated by the manufacturer as ±0.5 percent of full scale. For a full scale output of 10 V, this translates to a standard uncertainty of 0.05 V.

A.4.2 Uncertainty in Dwyer Hot Wire Anemometers

The expanded uncertainty of the Dwyer Model 641RM hot wire was stated by the manufacturer as ±3 percent of full scale. For a full scale output of 5 V, this translates to a standard uncertainty of 0.075 V.

A.4.3 Uncertainty in Hot Wire Curve Fit Coefficients

The outputs of the hot wire anemometers were measured for various bundle flow rates as shown in Figure A.1. Least-squares curve fits to these data were used to determine the slope and intercept. Standard statistical treatment within Excel was used to determine the standard error associated with each coefficient. The standard errors for the TSI curve fit coefficients were $u_{TSI,\,1}$ = 0.8 slpm/V and $u_{TSI,\,0}$ = 1.9 slpm. The standard errors for the Dwyer 2 hot wire curve fit coefficients were $u_{Dwyer2,\,1}$ = 0.9 slpm/V and $u_{Dwyer2,\,0}$ = 1.3 slpm.

APPENDIX B – OXIDATION OF ZIRCONIUM

The oxidation of zirconium alloys at high temperatures in steam, oxygen and nitrogen containing environments has been the subject of numerous studies. The temperature range of interest spans from 773 to 1,673 K (932 to 2,552°F). The pertinent reactions and the energy released at 1,500 K (2,240°F) are listed below (Ref. 1):

$$Zr + O_2 \rightarrow ZrO_2 \qquad \Delta H_{rxn} = -1{,}094.6 \text{ kJ/mol Zr} \qquad \text{B.1}$$

$$Zr + 2H_2O \rightarrow ZrO_2 + H_2 \qquad \Delta H_{rxn} = -529.1 \text{ kJ/mol Zr} \qquad \text{B.2}$$

$$Zr + \tfrac{1}{2} N_2 \rightarrow ZrN \qquad \Delta H_{rxn} = -365.4 \text{ kJ/mol Zr} \qquad \text{B.3}$$

$$ZrN + O_2 \rightarrow ZrO_2 + \tfrac{1}{2} N_2 \qquad \Delta H_{rxn} = -729.4 \text{ kJ/mol Zr} \qquad \text{B.4}$$

B.1 General Oxidation (Ref. 2)

At elevated temperatures, zirconium readily reacts with oxygen to form a zirconium dioxide product layer by reaction (Equation B.1). The reaction is highly exothermic. On a fresh zirconium surface the initial reaction rate is rapid but as soon as a product layer is formed, the reaction rate is controlled by the diffusion of oxygen through the growing product layer. Provided there is ample supply of oxygen at the surface and the oxide layer remains dense and intact, the oxygen reaction rate is solid state diffusion limited and well described by parabolic reaction kinetics. Parabolic kinetics describes diffusion controlled situations where the reaction rate decreases as the product layer thickens. With solid state diffusion the driving force is the concentration gradient in the solid phase, no porosity is required. This is in contrast to gas phase diffusion through a porous product layer. The zirconium oxidation rate is not dependent on the gaseous oxygen concentration or even the oxygen bearing species, thus pure oxygen (Equation B.1) and pure steam (Equation B.2) react at nearly the same rate and form nearly identical oxide layers. Under these conditions, at the gas/oxide interface the surface oxide is fully stoichiometric ZrO_2. At the inner oxide/metal interface, the oxide is substoichiometric ($\sim ZrO_{1.9}$) which drives the solid-state diffusion through the oxide layer. However, if the bulk gaseous oxidant concentration drops to low levels or if, at very high temperatures, the oxidation rate becomes very high, gaseous diffusion of oxidant to the surface may control the oxidation rate (Ref. 3). This situation is called oxygen/steam starvation. As a consequence, net oxygen diffusion from the oxide to the metal causes the formation of substoichiometric oxide scale and may even result in the complete dissolution of the oxide layer into the remaining metal phase.

B.2 Breakaway

As long as the growing product layer remains dense and intact, zirconium oxidation follows parabolic kinetics. However, eventually (and repeatedly) the product layer defects and "breaks away" from the inner metal interface and the reaction rate increases significantly. Several mechanisms seem to result in the breakaway phenomena. Often cited (Refs. 2, 4, 5, 6, 7) is the tetragonal to monoclinic phase transformation in the zirconia (ZrO_2) product layer at temperatures below 1,323 K (1,922°F) resulting in a 3 to 5 percent volume change (Refs. 8, 9). This phase transformation is clearly an important initiator for breakaway kinetics and the breakaway phenomena is not observed during isothermal tests at 1,373 K (2,012°F) and above. The mechanism leading to breakaway may also cause radial cracking along columnar grain boundaries to relieve accumulated compressive stresses (Ref. 7). The radial cracks provide direct access for the gas phase to reach fresh metal.

Additional mechanisms come into play when nitrogen is present in the gas phase. Above 1,073 K (1,472°F) where nitriding becomes important, breakaway occurs much sooner when nitrogen is present. Steinbrueck (Ref. 6) measured the time to breakaway for Zr alloys in oxygen-Ar, synthetic air - Ar and steam-Ar mixtures. The time to breakaway generally decreases with increasing temperature due to the faster oxidation kinetics with a "local maximum" at around 1,073 K (1,472°F) caused by the alpha-beta phase transition of the metal connected with increased plasticity. Duriez (Ref. 7) measured the time to breakaway for bare Zr-4 in air. The time to breakaway was about 450 minutes at 873 K (1,112°F), 100 minutes at 973 K (1,292°F), 30 minutes at 1,073 K (1,472°F) and 20 minutes at 1,173 K (1,652°F). At 1,073 K (1,472°F) and 1,173 K (1,652°F) the time to breakaway is an order of magnitude faster when nitrogen is present. Duriez (Ref. 7) proposes a mechanism where the oxygen is rapidly consumed in the bottom of radial cracks producing a local oxygen starved, nearly pure nitrogen atmosphere. The nitrogen reacts with zirconium to produce ZrN in a spot wise manner. As the oxidation front moves inward the ZrN islands become embedded in oxide and eventually oxidize. The oxidation of ZrN produces a 46 percent volume increase, which submits the oxide layer to local high stresses causing further cracking, and the scenario repeats itself. The oxide formed by this process is more porous and less protecting than the oxide layer formed initially.

B.3 MELCOR Kinetic Treatment

The oxidation of zirconium is modeled in MELCOR as limited by both solid-state diffusion of oxygen through the oxide layer (assumed parabolic) and gaseous diffusion of steam or oxygen to the oxide surface. Both rates are calculated and the slower is used to define the reaction rate.

The zirconium oxidation kinetics used in MELCOR is based on the recent kinetics study conducted at Argonne National Laboratory (ANL) (Ref. 10). Air oxidation of bare Zr-4 was observed at temperatures as low as 773 K (932°F). Test specimens were held at a constant temperature and the weight gain due to oxidation and nitride formation was measured as a function of time. The initial reaction rates were described by parabolic kinetics expected for solid state oxygen diffusion. However, the rate of oxidation increased after some period of time and persisted for the remainder of the test. The higher “breakaway” kinetic rate was also found to follow a parabolic rate law.

MELCOR incorporates both the pre- and post-breakaway kinetic correlations developed by Natesan and Soppet for bare Zr-4 (Ref. 10). The kinetic correlations found in Natesan and Soppet are given in units of mass of oxygen consumed while the kinetic correlation used by MELCOR are in units of mass of zirconium reacted, so an appropriate unit conversion is required.

A breakaway lifetime function is used to transition the model from pre- to post-breakaway kinetics. The model calculates an oxidation “lifetime” value for Zircaloy components in each cell using the local Zircaloy cladding temperature. Figure B.1 shows the breakaway timing data from the ANL tests. As the specimen temperature increased, the amount of time until breakaway became shorter.

For implementation into MELCOR, the ANL data was curve fit as follows.

$$LF = \int_0^t \frac{dt'}{\tau(T)} \qquad \text{B.5}$$

where, $\tau(T)$ is

$$\tau(T) = 10^{P_{LOX}} \quad \text{B.6}$$

and P_{LOX}

$$P_{LOX} = -12.528 \cdot \log 10\ T + 42.038 \quad \text{B.7}$$

A comparison of the data with Equation B.7 is shown in Figure B.1. For reference, specific values of the breakaway timing are provided in Table B.1.

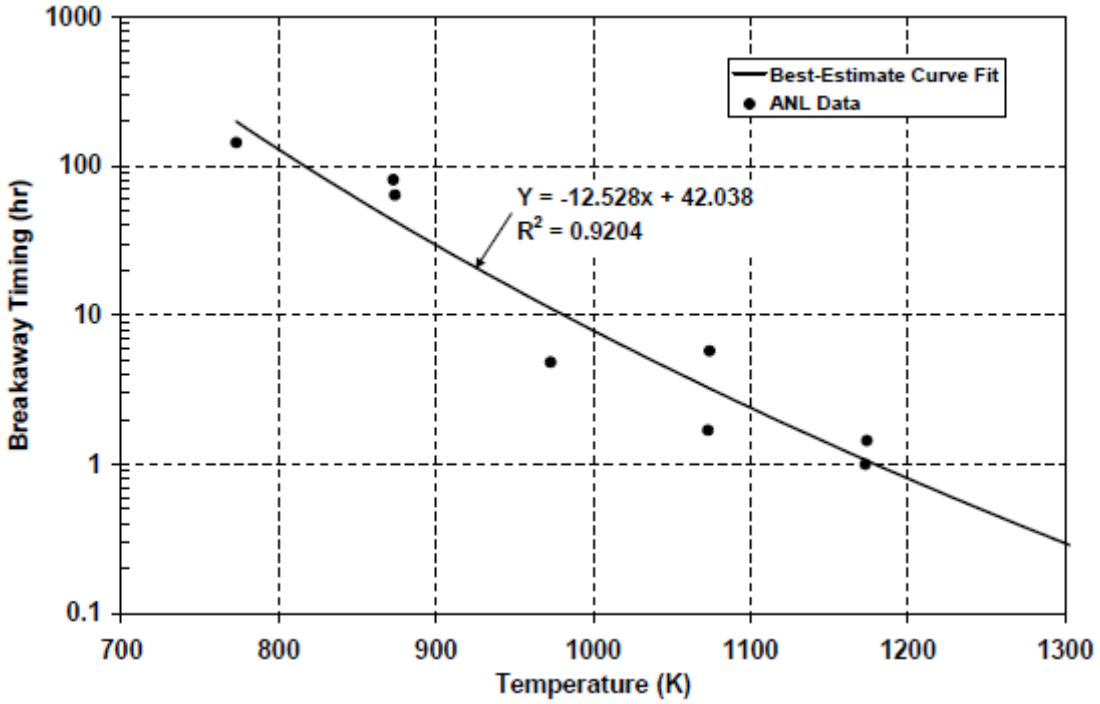

Figure B.1 Comparison of the MELCOR breakaway timing fit to Zr-4 data (Ref. 10)

The MELCOR breakaway oxidation model calculates the lifetime function at every node in the MELCOR model with Zircaloy cladding. The oxidation kinetics linearly transitions from the pre-breakaway correlation at *LF* = 1 to post-breakaway kinetics at *LF* = 1.25. Hence, only nodes that have exceeded the lifetime function will have the higher post-breakaway oxidation kinetics.

Table B.1 MELCOR Fit of the Timings for Transition from Pre-Breakaway to Post-Breakaway Oxidation Reaction Kinetics Zircaloy-4 in the ANL Experiments (Ref. 10)

Specimen Temperature	Breakaway Timing (Eqn. B.6)	ANL Data Used in Curve Fit
400°C (673 K)	1,125 hr (Extrapolated)	-
450°C (723 K)	458 hr (Extrapolated)	-
500°C (773 K)	198 hr	144 hr
550°C (823 K)	90 hr	-
600°C (873 K)	43 hr	64 and 81hr
650°C (923 K)	22 hr	-
700°C (973 K)	11 hr	4.8 hr
750°C (1,023 K)	5.9 hr	-
800°C (1,073 K)	3.3 hr	1.7 hr and 5.8 hr
850°C (1,123 K)	1.8 hr	-
900°C (1,173 K)	1.1 hr	1 hr and 1.4 hr

References

1. I. Barin, *Thermodynamic Data of Pure Substances*, VCH Verlagsgsellshaft mbG, Weinheim, and VCH Publishers, NewYork,1995.

2. M. Steinbrueck, “Prototypical experiments relating to air oxidation of Zircaloy-4 at high temperatures”, J. Nucl. Mat. 392 (2009) 531-544.

3. D.R. Olander, “Materials chemistry and transport modeling for severe accident analyses in light-water reactors. I: External cladding oxidation”, Nuclear Engineering and Design 148 (1994) 253-271.

4. J.H. Baek, and Y.H. Jeong, “Breakaway phenomenon of Zr-based alloys during a high-temperature oxidation”, J. Nucl. Mat. 372 (2008) 152-159.

5. C. Duriez, M. Steinbrueck, D. Ohai, T. Meleg, J. Birchley, T. Haste, “Separate-effect tests on zirconium cladding degradation in air ingress situations”, Nucl. Eng. Des. 239 (2009) 244-253

6. M. Steinbrueck, “Oxidation of Zirconium Alloys in Oxygen at High Temperatures up to 1600 ºC”, Oxid. Met. (2008) 70:317-329.

7. C. Duriez, T. Dupont, B. Schmet, and F. Enoch, “Zircaloy-4 and M5 high temperature oxidation and nitriding in air”, J. Nucl. Mat. 380 (2008) 30-45.

8. R.N. Patil, and E.C. Subbarao, "Monoclinic-tetragonal phase transition in zirconia: mechanism, pretransformation and coexistence”, Acta Crystallographica Section A 26, 535 (1970).

9. J. Chevalier, L. Gremillard, A.V. Virkar, and D.R. Clarke., “The tetragonal-monoclinic transformation in zirconia: Lessons learned and future trends”, J. Am. Ceram. Soc. 92 (2009), 1901-1920.

10. K. Natesan, and W.K. Soppet, “Air Oxidation Kinetics for Zr-Based Alloys”, NUREG/CR-6846, ANL-03/32, Argonne National Laboratory, June 2004.

APPENDIX C – MELCOR MODEL DESCRIPTION

Spatial representation of the assembly in both the CVH and COR packages is essentially one-dimensional, consisting of a stack of 10 control volumes and 17 axial core levels in a single radial ring (12 axial levels along the heated length of the rods), as shown in Figures C.1 through C.3.

Heater rod and other pool cell dimensions and masses were modeled based on data obtained from the facility description. As a simplification in the base case model, the mass of Nichrome resistive heating wire was excluded from consideration (i.e., the "fuel" component in the COR package was represented purely as the correct mass of MgO), and the small mass of upper plate and nozzle was also excluded.

The steel rack surrounding the pool cell was represented by mass allocated to the RK component available in recent versions of MELCOR for core models of type BWR-SFP and PWR-SFP. The layer of steel-wrapped Kaowool insulation surrounding the cell was represented as a radial boundary heat structure, which will thermally interact with the cell by means of thermal radiation heat transfer.

Spatial variation is accounted for only in the vertical direction (i.e., there is only one “ring” in the nodalization). Figures C.1 through C.3 show the nodalizations. The COR package uses 17 cells, with 12 of them lying in the heated region. Ten control volumes are defined: one for each of the free spaces above and below the assembly (CV020 and CV010), one for the region to the sides of the assembly (CV030), and eight for the assembly (CV101 – CV108). The rack wall is accounted for by MELCOR heat structures. Other masses are represented by COR package components.

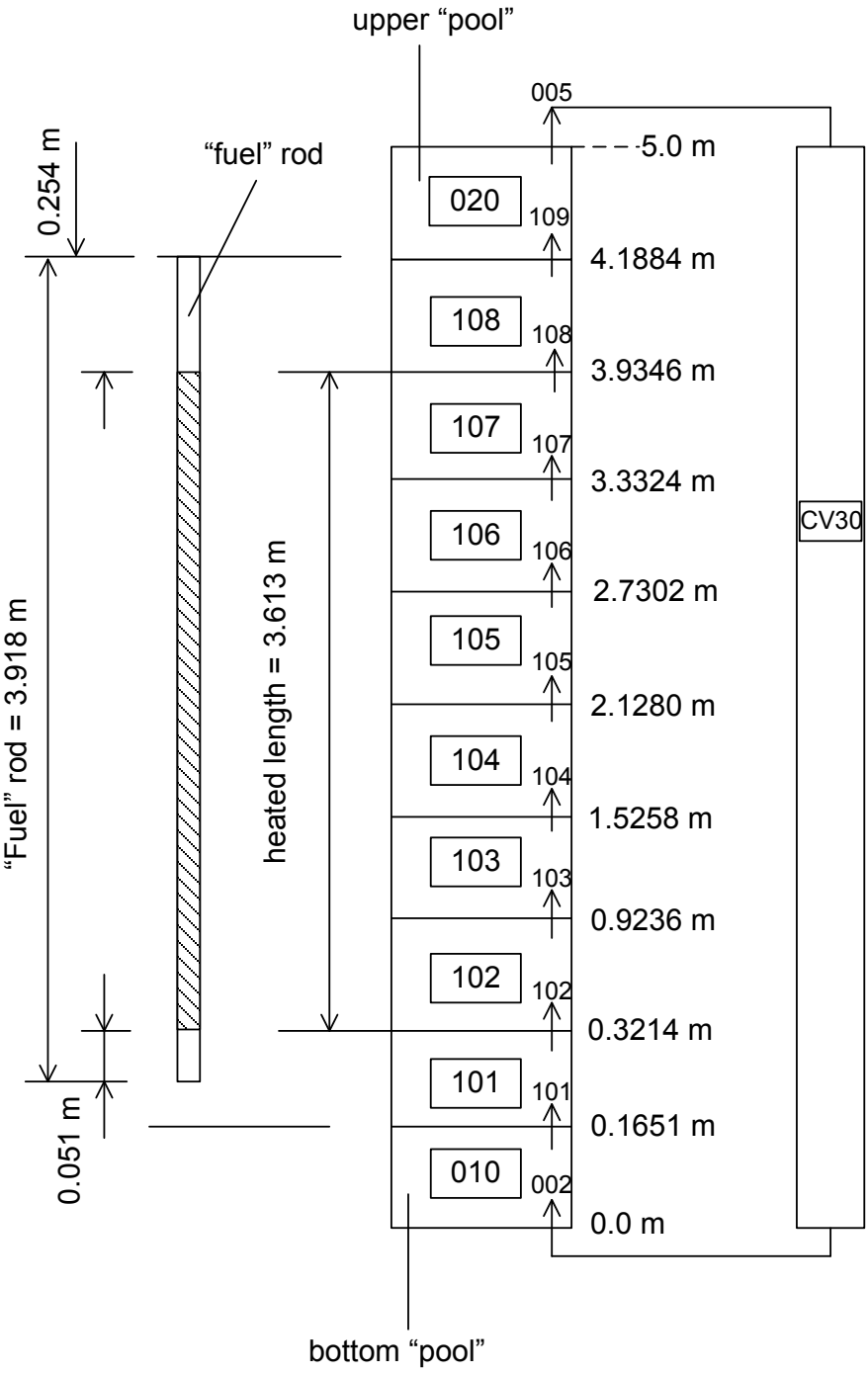

Figure C.1 Nodalization of PWR spent fuel assembly (Cell 2 in Phase I)

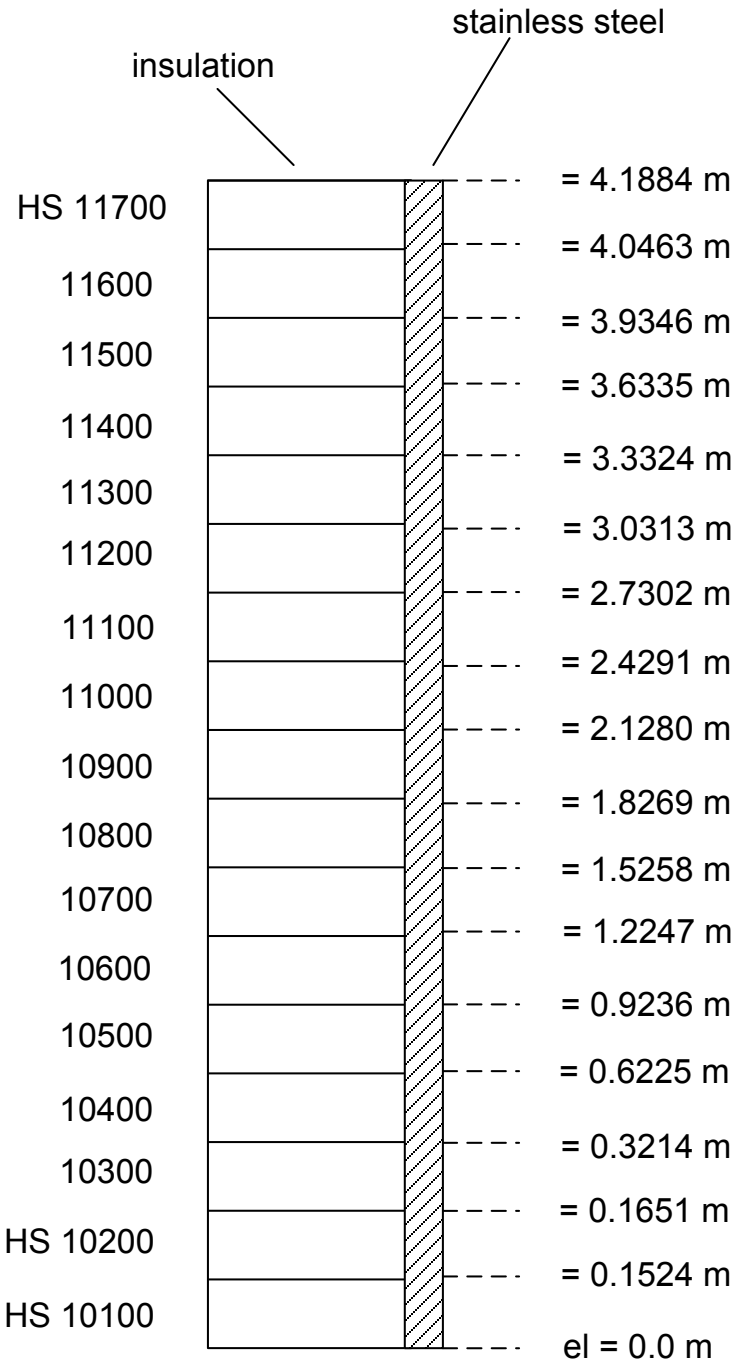

Figure C.2 Heat structures for the rack wall (Cell 2 in Phase I)

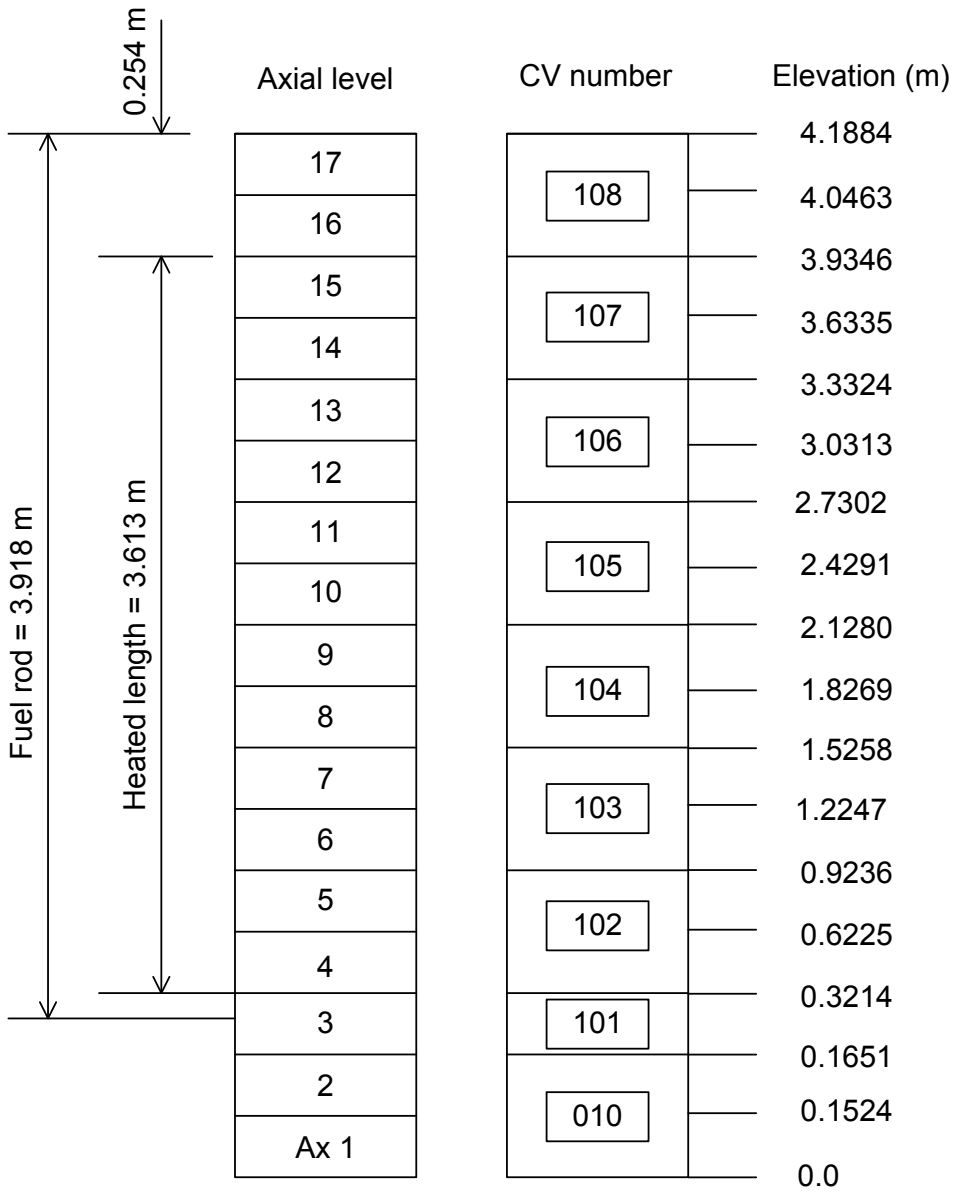

Figure C.3 Representation of the core cell nodes

NRC FORM 335
(12-2010)
NRCMD 3.7

U.S. NUCLEAR REGULATORY COMMISSION

BIBLIOGRAPHIC DATA SHEET

(See instructions on the reverse)

1. REPORT NUMBER
(Assigned by NRC, Add Vol., Supp., Rev., and Addendum Numbers, if any.)
NUREG/CR-7215

2. TITLE AND SUBTITLE
Spent Fuel Pool Project Phase I: Pre-Ignition and Ignition Testing of a Single Commercial 17x17 Pressurized Water Reactor Spent Fuel Assembly under Complete Loss of Coolant Accident Conditions

3. DATE REPORT PUBLISHED

MONTH	YEAR
April	2016

4. FIN OR GRANT NUMBER

5. AUTHOR(S)
S.G. Durbin, E.R. Lindgren. and A.S. Goldmann (Sandia National Laboratories)

M. Zavisca, Z. Yuan, R. Karimi, A. Krall, and M. Khatib-Rahbar (Energy Research, Inc.)

6. TYPE OF REPORT
Technical

7. PERIOD COVERED (Inclusive Dates)
July 2009 to July 2013

8. PERFORMING ORGANIZATION - NAME AND ADDRESS (If NRC, provide Division, Office or Region, U. S. Nuclear Regulatory Commission, and mailing address; if contractor, provide name and mailing address.)
Sandia National Laboratories, Albuquerque, NM 87185

Energy Research, Inc., Rockville, MD 20847-2034

9. SPONSORING ORGANIZATION - NAME AND ADDRESS (If NRC, type "Same as above", if contractor, provide NRC Division, Office or Region, U. S. Nuclear Regulatory Commission, and mailing address.)
Division of Systems Analysis
Office of Nuclear Regulatory Research
U.S. Nuclear Regulatory Commission
Washington, DC 20555-0001

10. SUPPLEMENTARY NOTES

11. ABSTRACT (200 words or less)
The US Nuclear Regulatory Commission (NRC), in collaboration with the Organisation for Economic Co-operation and Development (OECD), and 12 international partners, conducted an experimental program to obtain experimental data for the characterization of hydraulic and ignition phenomena of prototypic light water reactor fuel assemblies in a spent fuel pool under complete loss of coolant accidents for validation of the MELCOR severe accident computer code. MELCOR is a fully integrated, engineering-level computer code whose primary purpose is to model the progression of postulated accidents in light water reactors as well as non-reactor systems (e.g., spent fuel pool and dry cask). The experimental program, was conducted in two phases at Sandia National Laboratories. The first phase, described in this NUREG, focused on axial heating and zirconium fire propagation in a single 17x17 PWR fuel assembly. The results from the first phase of the experiments demonstrate that the MELCOR computer code can accurately simulate ignition timing and burn propagation in a single 17x17 PWR assembly under complete loss of coolant conditions.

12. KEY WORDS/DESCRIPTORS (List words or phrases that will assist researchers in locating the report.)
Spent Fuel Pool Project, Spent Fuel Pool, Spent Fuel Pool Loss of Coolant Accident, Pre-Ignition, Ignition, Spent Fuel Pool Pre-Ignition, Spent Fuel Pool Ignition

13 AVAILABILITY STATEMENT
unlimited

14 SECURITY CLASSIFICATION
(This Page)
unclassified
(This Report)
unclassified

15. NUMBER OF PAGES

16. PRICE

Federal Recycling Program

UNITED STATES
NUCLEAR REGULATORY COMMISSION
WASHINGTON, DC 20555-0001

OFFICIAL BUSINESS

NUREG/CR-7215

Spent Fuel Pool Project Phase I: Pre-Ignition and Ignition Testing of a Single Commercial 17x17 Pressurized Water Reactor Spent Fuel Assembly under Complete Loss of Coolant Accident Conditions

April 2016